



University
of Glasgow

Mills, Gordon B. (1999) *Scanning thermal microscopy using nanofabricated probes*. PhD thesis.

<http://theses.gla.ac.uk/3134/>

Copyright and moral rights for this thesis are retained by the author

A copy can be downloaded for personal non-commercial research or study, without prior permission or charge

This thesis cannot be reproduced or quoted extensively from without first obtaining permission in writing from the Author

The content must not be changed in any way or sold commercially in any format or medium without the formal permission of the Author

When referring to this work, full bibliographic details including the author, title, awarding institution and date of the thesis must be given

Scanning Thermal Microscopy Using Nanofabricated Probes

by
Gordon B Mills

Submitted for the the Degree of Doctor of Philosophy
to the Faculty of Engineering at the University of Glasgow

September, 1999

© Gordon Mills 1999

for Helen

Thanks To.....

- John Weaver glorious leader of the AFM group, championship supervisor and top chum. For teaching me so much, for shaving off his beard when I told him to, for losing everything I ever gave him, and for always being on for a cheeky babysham or two after the work was done.
- Ashish Midha for putting in the groundwork which made all this possible (just in time for me to arrive and steal the glory).
- Haiping Zhou for being the fabrication encyclopedia I never bought.
- Lesley Donaldson for all the micromachined substrates and technical support.
- Nanoelectronics Research Centre the A-team - for the unrivalled expertise in e-beam lithography and for providing such an enjoyable environment to work in for four years.
- Gari, Wei, Bridget, Juan, and Joe for technical support and social guidance while in Phoenix.
- The AFM group at Lancaster Uni. whose collaboration has been invaluable.
- Family and friends..... for much support and encouragement.

Abstract

Novel atomic force microscope (AFM) probes with integrated thin film thermal sensors are presented. Silicon micromachining and high resolution electron beam lithography (EBL) have been used to make batch fabricated, functionalised AFM probes. The AFM tips, situated at the ends of Si_3N_4 cantilevers, are shaped either as truncated pyramids or sharp triangular asperities. The former gives good thermalisation of the sensor to the specimen for flat specimens whereas the latter gives improved access to highly topographic specimens. Tip radii for the different probes are $\approx 1 \mu\text{m}$ and 50 nm respectively. A variety of metal structures have been deposited on the tips using EBL and lift-off to form Au/Pd thermocouples and Pd resistance thermometer/heaters. Sensor dimensions down to 35 nm have been demonstrated. In the case of the sharp triangular tips, holes were etched into parts of the cantilever in order to provide self alignment of the sensor to the tip. On the pyramidal tips it has been shown that multiple sensors can be made on a single tip with good definition and matching between sensors.

A conventional AFM was constructed in order to test the micromachined thermal probes. During scans of a photothermal test specimen using improved access thermocouple probes, 80 nm period metal gratings were thermally resolved. This is equivalent to a thermal lateral resolution of 40 nm. Pyramidal tips with a resistance thermometer/heater, which were made for the microscopy and analysis of polymers, have been shown by others to produce high resolution thermal conductivity images. The probes have also been shown to be capable of locally heating a polymer specimen and thermomechanically measuring phase changes in small volumes of material.

Also presented here is a study of scanning thermal microscopy of semiconductor structures using a commercial AFM. Included are scans of several specimens using both commercial and the new micromachined probes. Subsurface images of voids buried under a SiO_2 passivation layer were taken. It is shown that contrast caused by thermal conductivity differences in the specimen may be detected at a depth of over 200 nm.

Table of Contents

1	INTRODUCTION.....	7
1.1	SCANNING MICROSCOPES	7
1.2	ATOMIC FORCE MICROSCOPES	8
1.3	SCANNING THERMAL MICROSCOPES	10
1.4	PRIOR ART AT GLASGOW.....	14
1.5	MOTIVATION FOR WORK.....	16
2	GENERIC PROBE.....	23
2.1	FABRICATION TOOLS.....	23
2.2	ANALYSIS TOOLS.....	26
2.3	MICROMACHINED SUBSTRATE.....	27
2.4	3D LITHOGRAPHY.....	30
2.5	ADVANCED LIFT OFF	33
2.6	EVOLUTION OF GENERIC PROCESSING.....	35
3	INSTRUMENTATION.....	38
3.1	CONSTRUCTION OF AN AFM.....	38
3.2	AFM CONTROL ELECTRONICS.....	41
3.3	THERMOCOUPLE CIRCUITRY.....	44
4	THERMOCOUPLE PROBES.....	47
4.1	THERMOELECTRICITY	47
4.2	MATERIAL SYSTEM.....	49
4.3	CROSS THERMOCOUPLES.....	50
4.4	TRIPLE THERMOCOUPLES.....	54
5	IMPROVED ACCESS THERMOCOUPLES.....	61
5.1	MOTIVATION.....	61
5.2	FABRICATION DEVELOPMENT.....	61
5.3	“SIDE” THERMOCOUPLE PROBES.....	66
5.4	PHOTOTHERMAL EXPERIMENT.....	69
5.5	“SWISS CHEESE” THERMOCOUPLES.....	72
6	RESISTANCE THERMOMETER PROBES.....	74
6.1	INTRODUCTION.....	74
6.2	EARLY WORK / PROBE CONTAMINATION	76
6.3	“BOWTIE” PROBES	78

6.4	ENHANCED SENSITIVITY PROBES.....	83
6.5	SELF ALIGNED RESISTANCE PROBES.....	86
7	STUDIES AT CASE COLLABORATOR.....	91
7.1	INTRODUCTION.....	91
7.2	THERMAL PROBES.....	91
7.3	EXPERIMENTAL SETUP.....	93
7.4	PROBE CHARACTERISTICS.....	94
7.5	PASSIVATED WIRES.....	99
7.6	FIB TRENCHES.....	103
7.7	ANGLE CUT SPECIMEN.....	105
8	CONCLUSIONS.....	111
8.1	PROBE FABRICATION.....	111
8.2	MEASUREMENTS.....	113
8.3	ARTEFACTS.....	114
8.4	FUTURE WORK.....	116
9	PUBLICATIONS.....	120

1 Introduction

1.1 Scanning Microscopes

Many modern microscopy techniques are based on the concept of scanning including scanning electron microscopy (SEM) [1], scanning optical microscopy [2], and scanning probe microscopy (SPM) [3]. Research in the fields of material science [4], metallurgy [5], biology [6], medicine [7] and semiconductor technology [8] has been furthered using scanning microscopy. Measurements of such diverse properties as topography [9], ion transport [10], electrical conductance [11], fluorescence [12] and spectroscopy of optical emissions [13] have been made. The suitability of scanning microscopy to a wide range of measurements and environments arises from the fact that the principle of the microscope is in essence very simple. The idea is to sample information about the specimen at a number of points (pixels) and then display the spatial variation of the data as an image. This is a familiar and important way of visualising a specimen. Adding a scanner means that almost any single point measurement can evolve into a microscopy technique. Many measurements are made using sensors, probes or focused beams and these are particularly suited to scanning microscopy.

A recent growth area has been the examination of specimen properties on the micro and nano scale. This has been driven not only by research, but also by commercial activities in biomedical, pharmaceutical and semiconductor sectors. Of particular interest are

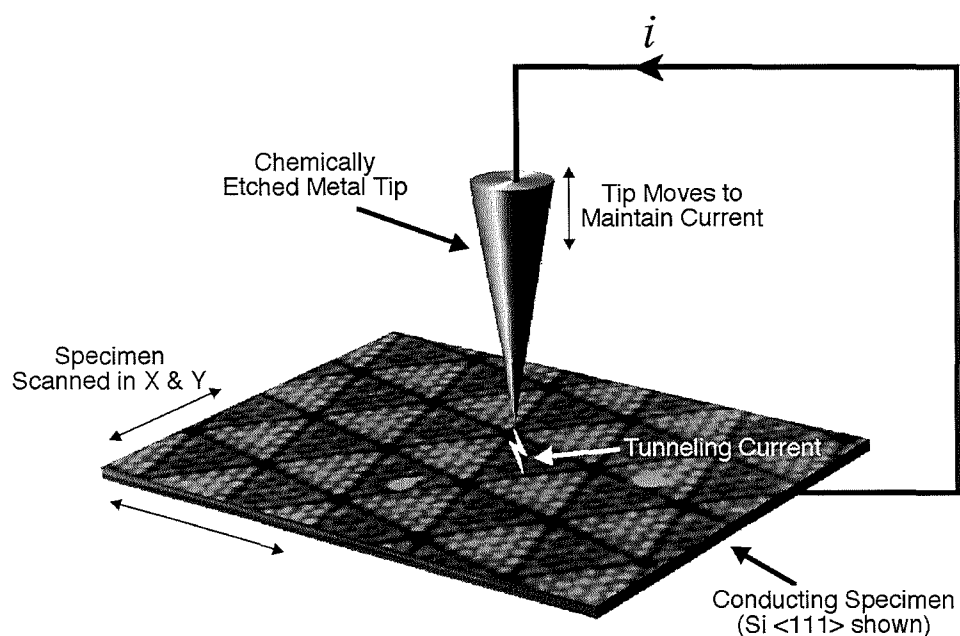


Figure 1-1 Schematic of a Scanning Tunneling Microscope.

microscopes that not only utilise the generic advantages of scanning, but also increase image resolution using miniaturisation of the sensor. Miniaturisation down to the molecular and atomic scale has only become possible in recent years following various developments in micro and nano technology. Key to miniature scanning microscopes, for example, is the use of piezoelectric transducers as nano-positioners [14], micromachining [15] and advanced patterning techniques such as optical and electron lithography [16-18].

1.2 Atomic Force Microscopes

Atomic force microscopy (AFM) [19, 20] is an innovative modification of the Nobel prize winning scanning tunnelling microscopy (STM) developed in 1982 by Binnig, Rohrer, Gerber and Weibel [21, 22]. Figure 1-1 shows a schematic of the STM, in which a sharp tip is used to electrically probe a conducting specimen. A voltage is applied to the tip and piezoelectric transducers used to bring the tip close to the specimen. When the spacing between tip and specimen becomes sufficiently small (of order 10 \AA) electrical tunnelling across the gap takes place [23]. The tip is then mechanically scanned over the specimen surface in a raster fashion, again using piezoelectric transducers. The tunnelling current is extremely sensitive to the tip to specimen separation and varies as topographic features on the specimen are encountered. Using a feedback loop to servo on the tunnelling current it is possible to maintain the gap and detect height changes of order 0.01 \AA . The signal from the feedback loop yields a topographic map of the specimen. Due to the extremely short range interactions that determine the tunnelling current, the inventors were able to resolve atoms of which a classic example is that of 7×7 silicon [24], shown in Figure 1-1. The contrast mechanisms in STM are complex and beyond the scope of this text. A thorough examination of the subject may be found elsewhere [3].

One drawback to the scanning tunnelling microscope however is that the specimen necessarily has to be electrically conducting. Atomic force microscopy, shown schematically in Figure 1-2, addresses this problem by mounting the sharp tip on a micro-cantilever. In this configuration, the tip to specimen distance is measured by detecting cantilever deflections instead of tunnelling current. This means that non-conducting specimens may be examined. The microscope tip can be operated in close proximity to the surface, called non-contact mode, in which case long range forces (Van der Waals, capillary, magnetic, electrostatic) cause attraction between tip and specimen [25]. Alternatively, the tip can be physically contacted to the specimen, called contact mode, where screening forces cause repellent forces between tip and specimen [26, 27]. In both cases the cantilever deflections must be detected with great accuracy, and this was originally achieved by positioning an STM tip on the reverse of the cantilever. Modern AFMs now commonly use optical techniques to detect cantilever deflections [3]. Atomic

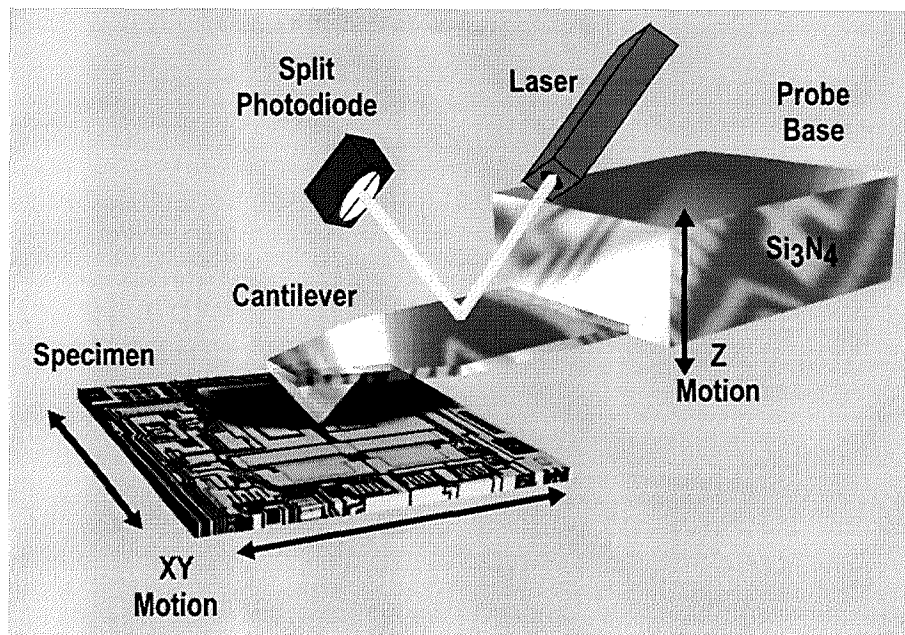


Figure 1-2 Schematic of an Atomic Force Microscope.

scale resolution has also been observed using the AFM [28, 29], however since the commercial availability of such instruments a key application has been measurements of larger scale nano-roughness.

A third class of microscope, which evolved some years after the AFM, is called the integrated sensor AFM. Here, microfabrication techniques are used to modify the AFM cantilever to incorporate an additional sensor. The sensors perform a variety of different functions. Some sensors have been used to replace the optical force sensing apparatus by including a piezoresistive element on the cantilever [30]. Another invention, more resembling the STM, used a micro-thermocouple to maintain tip to specimen separation by measuring heat loss from a heated tip [31]. Simultaneous measurements of the photothermal properties of the specimen were also made using this probe. A relatively simple modification of silicon probes involves coating the tip with a ferromagnetic material for magnetic imaging [32], or other conducting material for capacitive [33] and conductance measurements [34]. More complex microfabricated probes have included thermocouples for temperature mapping [35], fibre probes for high resolution optical microscopy [36] and micropipette or micromachined probes for ion conductance microscopy [10, 37]. Lithographic definition of sensors for SPM has been limited to a small number of groups, the most successful of which developed the Hall bar microscope for quantitative magnetic imaging [38].

1.3 Scanning Thermal Microscopes

Scanning thermal microscopy (SThM) is one of the new generation of integrated sensor AFM techniques. Temperature sensors used have included metal thermocouples [39], thermoresistors [40] and thermodiodes [41].

One of the first groups to incorporate a thermal sensor into the SPM environment was that led by H.K. Wickramasinghe at IBM in New York [31]. The instrument was called the scanning thermal profiler (STP) and operated by scanning a heated thermocouple junction, situated at the end of a sharp tip, across a sample surface. When brought close to the specimen, the thermocouple measured the rate of heat transfer into the specimen, and this was used to regulate the height of the tip. The instrument was operated in a similar fashion to an STM, using constant heat flow in place of constant tunnelling current, and hence was not truly a dual contrast mode microscope. The lateral topographic resolution of this instrument was reported as 0.1 μm .

A modified STP was developed by Oesterschultze et al at the University of Kassel, Germany [42]. A thermocouple was formed by coating a sharp metal tip with epoxy resin and then evaporating a second metal. Because the end of the metal tip remained uncoated due to the surface tension of the epoxy film, the junction between the two metals is localised to the tip apex. The size of the junction in this case covers an area 10 μm long at the end of the tip. Lateral topographic resolution was claimed at less than 30 nm. Such a small figure for resolution from such a large sensor is possible because the tip to specimen contact area, which is confined to the very end of the probe, is the determining factor.

Another thermal STM technique is the scanning tunnelling thermometer [43]. In this configuration a metal tip is used to form a thermocouple with a dissimilar conducting specimen. By plotting the thermoelectric voltage evolved when the tip to specimen junction was externally heated using a laser, temperature maps relating to optical absorption were produced. This technique proved to be unreliable in some cases because the thermocouple coefficient varies with position when used with heterogeneous specimens (later used as a contrast mechanism in scanning thermopower microscopy [44]). As with the STM, this technique is limited to imaging conducting samples. With the work of Nonnenmacher et al [45] this technology was transferred to the AFM environment. This instrument uses attractive mode force sensing to bring a heated metal coated Si tip into near contact with various metal specimens. Temperature is measured indirectly by detecting contact potential variations in a similar way to the Kelvin probe microscope [46, 47]. The thermal dependency arises from the temperature gradient formed between tip and specimen which,

depending on the proximity and thermal conductivity of the specimen, results in a change in the contact potential. Thermal conductivity and subsurface images were produced, with good correlation to the topographic features. Estimation of the exact temperature of the tip was hampered by parasitic heating of the tip from the force sensing laser and domination of a background signal level caused by the contact potential arising from the flat of the cantilever and the specimen.

A leading group in integrated sensor AFM is that of A. Majumdar and co-workers who work in the University of California, Santa Barbara. They have conducted a great deal of research into microthermocouple fabrication. An early attempt involved two wires, one chromel and one alumel, being fused together electrically and etched to form a sharp tip [35]. An aluminium foil mirror was then glued to the back of the wires which were mechanically twisted into a cantilever shape. The thermocouple junction size was approximately $25 \mu\text{m}^2$. One problem with this design however was that the tip tended to deform with the force of contact. To solve this, a shard of diamond was glued to the probe tip and one of its sharp facets scanned in place of the thermocouple [48]. Diamond has the highest thermal conductivity of any material at room temperature, so the thermal time constant of the instrument was not changed appreciably. An improvement in topographic resolution was observed, however the thermal spatial resolution was still limited by the thermocouple size. In addition to this, the probe characteristics were not reproducible between scans since it proved impossible to identify and reuse a specific facet of the diamond as the tip.

A different probe design by the same group featured a commercial silicon nitride cantilever and tip which was coated in metal and used as a bimetallic strip [49]. The approach here was to scan the cantilever in contact mode and measure temperature induced deflections, due to the difference in expansion coefficients of the metal and the silicon nitride. It was discovered that the deflection signal was dominated by heat convection in the air surrounding the cantilever, and not by conduction through the tip. The instrument was moved into vacuum and the tip radius increased by depositing a droplet of epoxy at the end of the tip. Improved thermal images were obtained, albeit with reduced thermal spatial resolution. The reported spatial resolution for topography was 1 nm with a corresponding thermal spatial resolution of $0.4 \mu\text{m}$. The group concluded that to reach 30-50 nm thermal spatial resolution, the thermal sensor would have to be similarly sized [39].

Further efforts by the Majumdar group in producing extremely small thermocouples involved processing commercial silicon nitride coated silicon cantilevers [50]. Here, the silicon nitride was first stripped off and replaced by a thin layer of Au. On top of this, a layer of silicon oxide was deposited followed by a thin layer of Pt. To pattern the sensor,

the tip was then brought into contact with a conducting surface and a voltage pulse of a few Volts applied between the specimen and tip. The voltage pulse caused the thin Pt film to evaporate around the point of contact, forming a small hole. After etching away the underlying oxide, a capping layer of Pt was evaporated over the tip to form a thermocouple junction equal in size to the hole at the end of the tip. Spatial resolution of the thermal image was claimed to be 10 nm, however this was determined from the noise equivalent spatial resolution of a single sharp edge caused by a spurious particle on the surface. Noise equivalent spatial resolution is a calculation made by dividing the edge length of a feature by the apparent signal to noise ratio in the image, and does not necessarily mean that any such resolution (defined by the more conventional criteria) was demonstrated. A disadvantage to this fabrication process was the unpredictable nature of the evaporation of the Pt film, and the likelihood of contamination of the junction at this stage. The metals were not always found to be in good contact and the thermocouple often did not last the duration of a scan. Cantilever heating effects again produced artefacts in the thermal images, because the front face of the cantilever was covered entirely in metal and therefore a good thermal conductor.

Production of probes using this voltage induced evaporation lithography moved on to a semi-batch process [51]. Shadow evaporation techniques were used to deposit metal pads onto arrays of cantilevers. The devices were then separated and processed as before. The group also made studies into the heat transfer mechanisms from tip to sample. They concluded that at room temperature the main heat flow mechanism between tip and sample was conduction through an aqueous separation layer.

The Kassel group have recently fabricated several different integrated sensor AFM probes in batch processes [52-55]. They use micromachining of bulk silicon and gallium arsenide [56] to produce wafers of around 200 tips. Their current thermal interests lie in fabrication of Schottky diode probes [41] and scanning Joule expansion microscopy [57, 58]. The Schottky diode probes use sharp conical tips with an approximately 250-500 nm active region at the tip apex. Specimen access here is excellent, however the fact that only a small fraction of the diode is in thermal contact with the sample could lead to any localised thermal signal being overcome by ambient thermal noise and $1/f$ noise in the sensor. Besides thermal application of the probe, the diode is also sensitive to electrical and optical fields.

The scanning Joule expansion technique was developed by the Kassel group in collaboration with A. Majumdar. The technique uses cantilever deflection in a conventional AFM probe to measure thermal expansion in a heated sample. Results have shown that thermal expansions down to 1 pm can be detected.

An alternative to techniques where passive thermometers like thermocouples and diodes are used to measure temperature, is SThM using resistance thermometers. These simple thermometers can also heat the specimen, and therefore be used in an active stimulus / response mode. The combination of resistance thermometry with AFM was first demonstrated by Dinwiddie and co-workers [40], who micromechanically fashioned miniature Pt_{0.9}Rh_{0.1} wires into a cantilever shape with a protruding tip. The Pt_{0.9}Rh_{0.1} wire was 5 µm in diameter with a 75 µm Ag cladding. The cladding was removed around the tip, increasing the probe resistance at the tip and also decreasing the tip dimensions. By applying a small voltage to the resistive probe and measuring thermally induced resistance changes, temperature changes at the tip can be detected. Alternatively, if a large current is applied to the tip, significant heating can occur. Using the tip as a heat source, the heat flow from tip to specimen can be measured. Applications for this technique include localised calorimetry [59], thermal mapping of polymer blends [60], measurement of thermal conductivities [61] and Fourier transform infra-red (FTIR) analysis of polymer films [62]. In addition to these, several experiments have been carried out in the field of sub-surface thermal imaging [63, 64]. It is possible to detect and estimate the depth of subsurface features using resistive probes by modulating the electrical heating. Solution of the one dimensional wave equation

$$\frac{\partial^2 T}{\partial x^2} - \frac{1}{D} \frac{\partial T}{\partial t} = 0$$

where D is the thermal diffusivity of the specimen, T is temperature, x is the depth of penetration and t is time, gives the thermal diffusion length, L, of the heat into the specimen to be

$$L = \sqrt{\frac{2D}{\omega}}$$

This assumes periodic modulation of the heat source at angular frequency ω , that the tip radius is infinitely large, and that conduction is the only heat transfer mechanism. In reality, where a probe of finite tip radius is used, the problem is much more complex, however this simple analysis shows that the depth of penetration may be controlled to some degree by varying the modulation frequency of the heat source. A more thorough examination of the subject is given elsewhere [65].

One use for resistively heated thermal probes is in the field of AFM storage. Mamin et al from IBM Almaden have achieved write densities of 10 Gb/in² at 100 kb/s [66] and read rates of 1.2 Mb/s [67]. Initial strategies employed piezoresistive AFM cantilevers heated using a focused infra-red laser [68] and then electrical heating of the whole cantilever [69]

to create nanoindentations in a polymer film. In order to decrease write times however the thermal source needed to be reduced in size. This was achieved by selectively ion implanting silicon cantilevers to leave a resistive region several microns wide at the tip [66]. Thermal time constants of 30 μ s were observed compared to \approx 40 ms when heating the whole cantilever. Such instruments may benefit from further miniaturisation of thermal heaters and other innovations such as multiple cantilevers operated in parallel [70].

1.4 Prior Art at Glasgow

An initial study into using lithographic techniques to pattern sensors onto AFM tips was carried out in 1993 by an undergraduate student at the University of Glasgow [71]. Results showed that recessed micromachined silicon tips could be coated with resist and patterned using electron beam lithography (EBL). This discovery initiated a four year effort to arrive at a generic technology for making integrated sensor AFM probes. Funding was procured¹ and A. Midha, a postgraduate student, and Dr H. Zhou, a postgraduate research assistant, were recruited to aid the development.

A design for batch fabricating integrated sensor AFM probes was developed 1993-1996, and is described in full in the PhD thesis by A. Midha [72]. The principle of this design was to provide a generic probe that would support multiple layers of lithography on and around an AFM tip, thus allowing the fabrication of localised sensors. A variety of sensors were envisioned including scanning near field optical microscopy (SNOM) apertures [73], Hall Magnetometers [38] and thermometers. The goal was to advance these emerging AFM techniques by shrinking sensor dimensions and improving the reproducibility and stability of the integrated sensor probes.

Critical to this project was the availability of electron beam lithography at Glasgow University. Photolithography [18] and silicon etching [74] is routinely used to batch fabricate sharp tips for topographic mapping [15], but attempts to combine lithography and micromachining to make integrated sensor probes have encountered alignment and resolution limits on the micron scale [51]. Using EBL brings the ability to pattern features and automatically align on the nanometer scale [17, 75, 76].

Figure 1-3 shows a schematic of an individual cantilever as proposed by A. Midha et al. Layers which defined the sensor at the tip apex are patterned on a silicon nitride cantilever supported on a silicon membrane. Probe bases, alignment marks, cantilevers and tips are all defined by etching a single silicon wafer and so the probes are monolithic in nature (see

¹ 9/1994-8/1996, EPSRC, "Nanofabrication of scanned probe microscope sensors", £212k, GR/K24307

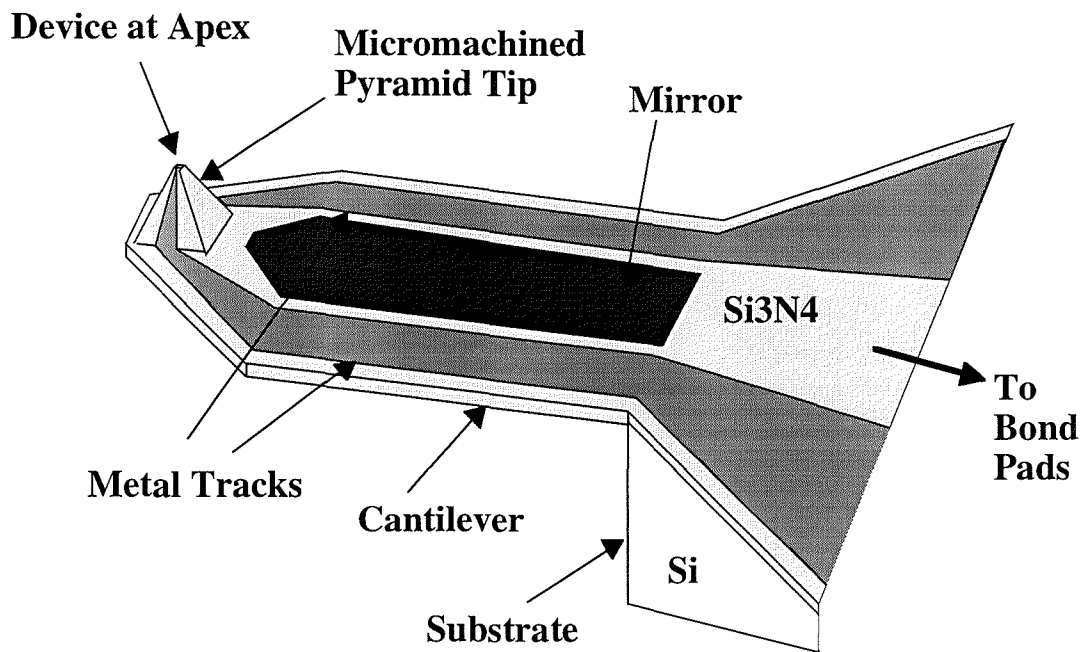


Figure 1-3 Schematic of a generic AFM cantilever.

Chapter 2). This served to overcome many historical difficulties encountered when trying to add sensors to AFM cantilevers. Adapting planar semiconductor techniques to a custom made 3-dimensional substrate became the task, as opposed to processing a fragile free standing cantilever.

After several iterative design modifications to achieve the maximum device quantity per wafer, but with suitable substrate resilience, the generic substrate emerged as a 3" silicon wafer containing 240 "blank" probes, ready for EBL modification. The wafer was designed to be cleaved into quarters before sensor definition to aid speedy process development, but all processing was designed to be compatible with the use of 3" wafers. Although batch fabrication of probes lends itself readily to mass production for commercial purposes, this was not the original motivation of the inventors. Rather, the primary objective was to provide a supply of near identical probes for research purposes. It was hoped that this would add stability and continuity to integrated sensor AFM experiments, and also provide a technology base for producing more complex probes (e.g. combined sensors on a single probe).

The situation at the start of this project was that a scheme for fabricating wafers of probes ready for EBL modification had been developed. Sensor technology was less well advanced. Most of the effort by A. Midha had been directed at producing probes with integrated apertures for SNOM. However, problems involving the pattern transfer of the

apertures and subsequent metal cladding had delayed progress substantially. The patterning of metal features to produce thermal devices had already been demonstrated on flat test specimens and Dr H. Zhou was actively involved in furthering this work to three dimensional substrates.

Summarising, the current state of technology inherited at the beginning of the project comprised:

- Etching of a commercially available three inch silicon wafer to form batch fabricated probe bases.
- Through wafer alignment markers for use with EBL.
- A timed silicon etch to form pyramidal tips.
- “Float coating” - a novel resist scheme for coating three dimensional features [77].
- Software implementation for automatic refocusing of the Leica EBL machine for writing patterns on substrates with significant relief.
- A KOH etch resistant material system for patterning metal features on the end of pyramid tips.
- A final silicon release etch for dissolving the supporting membrane to leave free standing AFM cantilevers.

1.5 Motivation for Work

Building on the work of the AFM group at the University of Glasgow, this project was focused on the advancement of the technology for generic, batch fabricated, integrated sensor AFM probes. The motivation was to use the technology to produce thermal probes for high resolution SThM. The specific goals were to develop the existing fabrication processes to give reproducible working probes, to explore the characteristics of the new probes, and to scan specimens which would demonstrate their enhanced capabilities. The manufacture of the probes remained core, however unlike other predominantly fabrication based projects the application of the technology was a top priority.

The fabrication aims of the project were as follows:

- Use EBL to pattern thermal sensors on the generic cantilevers designed by A. Midha.
- Increase the yield of probes to produce many identical probes.
- Address the problem of poor specimen access inherent to the existing probes.

The benefits of using EBL to make integrated sensor probes are threefold. Firstly, EBL is a tool that can typically produce features of order 50 nm. If implemented successfully this

would improve significantly on current SThM sensor miniaturisation. Secondly, the automation used with such tools allows many levels to be accurately aligned to the AFM tip. This differs from most other “punctual” techniques where a single event (electrical evaporation or fusion, non-continuity of resist, chemical etching, micromanipulation) localises the sensor to the tip apex. The benefits of lithographic definition are that sensors may become more complex by adding multiple levels, and have much smaller feature dimensions. Lastly, the excellent reproducibility offered by EBL means that sensors will vary less from probe to probe. Currently, probes tend to be individually characterised before use and each experiment is then unique to that probe.

Emerging analytical techniques on the nanometer scale are of considerable interest to the semiconductor industry, and as such this project attracted sponsorship from *Motorola MRST*². The sponsorship was in the form of an Engineering and Physical Sciences Research Council (EPSRC) Co-operative Award in Science in Engineering (CASE). Due to a need for new microscopic techniques with which to examine ever shrinking generations of integrated circuit, the project was supported both financially and with expertise in the areas of microscopy and material characterisation. Part of the sponsorship involved an extended period of work at the Materials Characterisation Lab in Mesa, Arizona (see Chapter 7). The objective was to assess SThM by examining semiconductor devices and related structures. Some of the perceived applications of SThM to *Motorola* were as follows.

- Thermal detection of local heat distributions in densely populated very large scale integrated (VLSI) devices.
- Identification of electrical faults which result in thermal features.
- Detection of subsurface elements of multilayer structures.
- Non-invasive inspection of packaged devices with passivation coatings.
- Profiling the optical output of semiconductor lasers.

Additional motivation for the development of thermal probes was provided by an informal collaboration between the University of Glasgow and the University of Lancaster, England. The group in the Department of Physics in Lancaster, headed by Dr H. M. Pollock, are experts in thermal microscopy of polymers. Using resistance thermometer probes, pioneering work has resulted in the invention of CASM (calorimetric analysis with scanning microscopy) and MASM (mechanothermal analysis with scanning microscopy) [78]. Improvements on the current Wollaston wire technology were anticipated in the form

² Materials Research and Strategic Technologies, Motorola SPS, 2200 West Broadway Rd, Mesa, Arizona 85202

of increased thermal imaging resolution, improved response time and decreased analysis volumes.

- [1] *Light and Electron Microscopy*: Cambridge University Press, 1992.
- [2] J. B. Pawley, *Handbook of Biological Confocal Microscopy*. New York: Plenum Press, 1990.
- [3] *Scanning probe microscopy and spectroscopy*: Cambridge University Press, 1994.
- [4] S. Amelinckx, R. Gevers, and J. Van Landuyt, *Diffraction and Imaging Techniques in Material Science*, vol. 1: North Holland Publishing Company, 1978.
- [5] *Metallurgical Microscopy*: Butterworth, 1973.
- [6] A. M. Baro, R. Miranda, J. Alaman, N. Garcia, G. Binnig, H. Rohrer, C. Gerber, and J. L. Carrascosa, "Determination of surface-topography of biological specimens at high- resolution by scanning tunnelling microscopy," *Nature*, vol. 315, pp. 253-254, 1985.
- [7] *Electron microscopy in human medicine*, vol. 1-11: McGraw Hill, 1978-1983.
- [8] S. M. Sze, *VLSI Technology*: McGraw Hill, 1988.
- [9] G. Binnig and H. Rohrer, "Surface imaging by scanning tunneling microscopy," *Ultramicroscopy*, vol. 11, pp. 157-160, 1983.
- [10] C. B. Prater, P. K. Hansma, M. Tortonese, and C. F. Quate, "Improved scanning ion-conductance microscope using microfabricated probes," *Review Of Scientific Instruments*, vol. 62, pp. 2634-2638, 1991.
- [11] A. Olbrich, B. Ebersberger, and C. Boit, "Conducting atomic force microscopy for nanoscale electrical characterization of thin SiO₂," *Applied Physics Letters*, vol. 73, pp. 3114-3116, 1998.
- [12] *Fluorescent Probes in Cellular and Molecular Biology*: CRC Press, 1994.
- [13] R. C. Davis and C. C. Williams, "Nanometer-scale absorption-spectroscopy by near-field photodetection optical microscopy," *Applied Physics Letters*, vol. 69, pp. 1179-1181, 1996.
- [14] G. Binnig and D. P. E. Smith, "Single-tube 3-dimensional scanner for scanning tunneling microscopy," *Review Of Scientific Instruments*, vol. 57, pp. 1688-1689, 1986.
- [15] T. R. Albrecht, S. Akamine, T. E. Carver, and C. F. Quate, "Microfabrication of cantilever styli for the atomic force microscope," *Journal Of Vacuum Science & Technology a-Vacuum Surfaces and Films*, vol. 8, pp. 3386-3396, 1990.
- [16] S. P. Beaumont, P. G. Bower, T. Tamamura, and C. D. W. Wilkinson, "Sub-20-nm-wide metal lines by electron-beam exposure of thin poly(methyl methacrylate) films and liftoff," *Applied Physics Letters*, vol. 38, pp. 436-439, 1981.
- [17] R. F. W. Pease, "Electron-beam lithography," *Contemporary Physics*, vol. 22, pp. 265-290, 1981.
- [18] B. J. Lin, "Deep uv lithography," *Journal Of Vacuum Science & Technology*, vol. 12, pp. 1317-1320, 1975.
- [19] G. Binnig, C. F. Quate, and C. Gerber, "Atomic force microscope," *Physical Review Letters*, vol. 56, pp. 930-933, 1986.

-
- [20] G. Binnig, "Force microscopy," *Ultramicroscopy*, vol. 42, pp. 7-15, 1992.
- [21] G. Binnig, H. Rohrer, C. Gerber, and E. Weibel, "Tunneling through a controllable vacuum gap," *Applied Physics Letters*, vol. 40, pp. 178-180, 1982.
- [22] G. Binnig and H. Rohrer, "Scanning tunneling microscopy," *Helvetica Physica Acta*, vol. 55, pp. 726-735, 1982.
- [23] G. Binnig, H. Rohrer, C. Gerber, and E. Weibel, "Vacuum tunneling," *Physica B&C*, vol. 110, pp. 2075-2077, 1982.
- [24] G. Binnig, H. Rohrer, C. Gerber, and E. Weibel, "7X7 Reconstruction on si(111) resolved in real space," *Physical Review Letters*, vol. 50, pp. 120-123, 1983.
- [25] M. Nonnenmacher, J. Greschner, O. Wolter, and R. Kassing, "Scanning force microscopy with micromachined silicon sensors," *Journal Of Vacuum Science & Technology B*, vol. 9, pp. 1358-1362, 1991.
- [26] *The Solid State*: Oxford Science Publications, 1978.
- [27] *Solid State Physics*: Cambridge University Press, 1974.
- [28] G. Binnig, C. Gerber, E. Stoll, T. R. Albrecht, and C. F. Quate, "Atomic resolution with atomic force microscope," *Surface Science*, vol. 189, pp. 1-6, 1987.
- [29] F. Ohnesorge and G. Binnig, "True atomic-resolution by atomic force microscopy through repulsive and attractive forces," *Science*, vol. 260, pp. 1451-1456, 1993.
- [30] M. Tortonesi, R. C. Barrett, and C. F. Quate, "Atomic resolution with an atomic force microscope using piezoresistive detection," *Applied Physics Letters*, vol. 62, pp. 834-836, 1993.
- [31] C. C. Williams and H. K. Wickramasinghe, "Scanning thermal profiler," *Applied Physics Letters*, vol. 49, pp. 1587-1589, 1986.
- [32] P. Grutter, E. Meyer, H. Heinzelmann, L. Rosenthaler, H. R. Hidber, and H. J. Guntherodt, "Magnetic imaging by atomic force microscope," *Journal Of Applied Physics*, vol. 63, pp. 2947-2947, 1988.
- [33] C. C. Williams, W. P. Hough, and S. A. Rishton, "Scanning capacitance microscopy on a 25 nm scale," *Applied Physics Letters*, vol. 55, pp. 203-205, 1989.
- [34] A. Born, A. Olbrich, M. Maywald, and R. Wiesendanger, "Analysis of electrical breakdown failures by means of SFM-based methods," *Applied Physics a-Materials Science & Processing*, vol. 66, pp. S1063-S1065, 1998.
- [35] A. Majumdar, J. P. Carrejo, and J. Lai, "Thermal imaging using the atomic force microscope," *Applied Physics Letters*, vol. 62, pp. 2501-2503, 1993.
- [36] E. Betzig, S. G. Grubb, R. J. Chichester, D. J. Digiovanni, and J. S. Weiner, "Fiber laser probe for near-field scanning optical microscopy," *Applied Physics Letters*, vol. 63, pp. 3550-3552, 1993.
- [37] P. K. Hansma, B. Drake, O. Marti, S. A. C. Gould, and C. B. Prater, "The scanning ion-conductance microscope," *Science*, vol. 243, pp. 641-643, 1989.
- [38] A. Oral, S. J. Bending, and M. Henini, "Scanning Hall probe microscopy of superconductors and magnetic materials," *Journal Of Vacuum Science & Technology B*, vol. 14, pp. 1202-1205, 1996.
-

-
- [39] A. Majumdar, J. Lai, M. Chandrachood, O. Nakabeppu, Y. Wu, and Z. Shi, "Thermal imaging by atomic-force microscopy using thermocouple cantilever probes," *Review Of Scientific Instruments*, vol. 66, pp. 3584-3592, 1995.
- [40] R. B. Dinwiddie, R. J. Pyllki, and P. E. West, "Thermal conductivity contrast imaging with a scanning thermal microscope," in *Thermal Conductivity*, T. W. Tong, Ed., 1994, pp. 22.
- [41] T. Leinhos, M. Stopka, and E. Oesterschulze, "Micromachined fabrication of Si cantilevers with Schottky diodes integrated in the tip," *Applied Physics a-Materials Science & Processing*, vol. 66, pp. S65-S69, 1998.
- [42] M. Stopka, L. Hadjiiski, E. Oesterschulze, and R. Kassing, "Surface investigations by scanning thermal microscopy," *Journal Of Vacuum Science & Technology B*, vol. 13, pp. 2153-2156, 1995.
- [43] J. M. R. Weaver, L. M. Walpita, and H. K. Wickramasinghe, *Applied Physics Letters*, vol. 49, pp. 1587, 1989.
- [44] J. Xu, B. Koslowski, R. Moller, K. Lauger, K. Dransfeld, and I. H. Wilson, "Proposal to study the thermopower produced by a vacuum-tunneling junction," *Journal Of Vacuum Science & Technology B*, vol. 12, pp. 2156-2160, 1994.
- [45] M. Nonnenmacher and H. K. Wickramasinghe, "Scanning probe microscopy of thermal-conductivity and subsurface properties," *Applied Physics Letters*, vol. 61, pp. 168-170, 1992.
- [46] M. Nonnenmacher, M. P. Oboyle, and H. K. Wickramasinghe, "Kelvin probe force microscopy," *Applied Physics Letters*, vol. 58, pp. 2921-2923, 1991.
- [47] J. M. R. Weaver and D. W. Abraham, "High-resolution atomic force microscopy potentiometry," *Journal Of Vacuum Science & Technology B*, vol. 9, pp. 1559-1561, 1991.
- [48] J. Lai, M. Chandrachood, A. Majumdar, and J. P. Carrejo, "Thermal detection of device failure by atomic-force microscopy," *Ieee Electron Device Letters*, vol. 16, pp. 312-315, 1995.
- [49] O. Nakabeppu, M. Chandrachood, Y. Wu, J. Lai, and A. Majumdar, "Scanning thermal imaging microscopy using composite cantilever probes," *Applied Physics Letters*, vol. 66, pp. 694-696, 1995.
- [50] K. Luo, Z. Shi, J. Lai, and A. Majumdar, "Nanofabrication of sensors on cantilever probe tips for scanning multiprobe microscopy," *Applied Physics Letters*, vol. 68, pp. 325-327, 1996.
- [51] K. Luo, Z. Shi, J. Varesi, and A. Majumdar, "Sensor nanofabrication, performance, and conduction mechanisms in scanning thermal microscopy," *Journal Of Vacuum Science & Technology B*, vol. 15, pp. 349-360, 1997.
- [52] S. Munster, S. Werner, C. Mihalcea, W. Scholz, and E. Oesterschulze, "Novel micromachined cantilever sensors for scanning near-field optical microscopy," *Journal Of Microscopy-Oxford*, vol. 186, pp. 17-22, 1997.
- [53] E. Oesterschulze, W. Scholz, C. Mihalcea, D. Albert, B. Sobisch, and W. Kulisch, "Fabrication of small diamond tips for scanning probe microscopy application," *Applied Physics Letters*, vol. 70, pp. 435-437, 1997.
- [54] E. Oesterschulze and M. Stopka, "Imaging of thermal-properties and topography by combined scanning thermal and scanning-tunneling-microscopy," *Microelectronic Engineering*, vol. 31, pp. 241-248, 1996.
-

-
- [55] C. Mihalcea, W. Scholz, S. Werner, S. Munster, E. Oesterschulze, and R. Kassing, "Multipurpose sensor tips for scanning near-field microscopy," *Applied Physics Letters*, vol. 68, pp. 3531-3533, 1996.
- [56] S. Heisig and E. Oesterschulze, "Gallium arsenide probes for scanning near-field probe microscopy," *Applied Physics a-Materials Science & Processing*, vol. 66, pp. S385-S390, 1998.
- [57] S. Munster, T. Chang, R. Kassing, A. Majumdar, and E. Oesterschulze, "Micromachined Probes for High Frequency Scanning Electrical Force Microscopy and Scanning Joule Expansion Microscopy," *Pre-Print*, 1997.
- [58] J. Varesi and A. Majumdar, "Scanning Joule expansion microscopy at nanometer scales," *Applied Physics Letters*, vol. 72, pp. 37-39, 1998.
- [59] A. Hammiche, M. Reading, H. M. Pollock, M. Song, and D. J. Hourston, "Localized thermal analysis using a miniaturized resistive probe," *Review Of Scientific Instruments*, vol. 67, pp. 4268-4274, 1996.
- [60] A. Hammiche, D. J. Hourston, H. M. Pollock, M. Reading, and M. Song, "Scanning thermal microscopy - subsurface imaging, thermal mapping of polymer blends, and localized calorimetry," *Journal Of Vacuum Science & Technology B*, vol. 14, pp. 1486-1491, 1996.
- [61] L. J. Balk, M. Maywald, and R. J. Pylkki, "Nanosopic detection of the thermal-conductivity of compound semiconductor-materials by enhanced scanning thermal microscopy," *Institute Of Physics Conference Series*, vol. 146, pp. 655-658, 1995.
- [62] A. Hammiche, H. M. Pollock, M. Reading, M. Claybourn, P. H. Turner, and K. Jewkes, "Photothermal FT-IR spectroscopy: A step towards FT-IR microscopy at a resolution better than the diffraction limit," *Applied Spectroscopy*, vol. 53, pp. 810-815, 1999.
- [63] A. Hammiche, H. M. Pollock, M. Song, and D. J. Hourston, "Subsurface imaging by scanning thermal microscopy," *Measurement Science & Technology*, vol. 7, pp. 142-150, 1996.
- [64] A. Hammiche, M. Song, H. M. Pollock, M. Reading, and D. J. Hourston, "Subsurface sthm imaging of blends, with localized calorimetric analysis," *Abstracts Of Papers Of the American Chemical Society*, vol. 212, pp. 278-POLY, 1996.
- [65] D. Almond, and P. Patel, *Photothermal Science and Techniques*: Chapman and Hall, 1996.
- [66] B. W. Chui, T. D. Stowe, Y. S. Ju, K. E. Goodson, T. W. Kenny, H. J. Mamin, B. D. Terris, R. P. Ried, and D. Rugar, "Low-stiffness silicon cantilevers with integrated heaters and piezoresistive sensors for high-density AFM thermomechanical data storage," *Journal Of Microelectromechanical Systems*, vol. 7, pp. 69-78, 1998.
- [67] B. W. Chui, T. D. Stowe, T. W. Kenny, H. J. Mamin, B. D. Terris, and D. Rugar, "Low-stiffness silicon cantilevers for thermal writing and piezoresistive readback with the atomic force microscope," *Applied Physics Letters*, vol. 69, pp. 2767-2769, 1996.
- [68] H. J. Mamin and D. Rugar, "Thermomechanical writing with an atomic force microscope tip," *Applied Physics Letters*, vol. 61, pp. 1003-1005, 1992.
- [69] H. J. Mamin, "Thermal writing using a heated atomic force microscope tip," *Applied Physics Letters*, vol. 69, pp. 433-435, 1996.
- [70] S. C. Minne, S. R. Manalis, and C. F. Quate, "Parallel atomic force microscopy using cantilevers with integrated piezoresistive sensors and integrated piezoelectric actuators," *Applied Physics Letters*, vol. 67, pp. 3918-3920, 1995.
-

- [71] S. Rahman, "Final year project in E&EE," , vol. supervised by Dr J.M.R. Weaver, pp. University of Glasgow, 1994.
- [72] A. Midha, "Batch-fabrication of novel nanoprobes for SPM," in *Electronics & Electrical Engineering*. Glasgow: University of Glasgow, submission due 1999.
- [73] E. Betzig, A. Harootunian, A. Lewis, and M. Isaacson, "Near-field scanning optical microscopy (nsom) - investigation of radiation transmitted through sub-wavelength apertures," *Biophysical Journal*, vol. 47, pp. A407-A407, 1985.
- [74] K. R. Williams and R. S. Muller, "Etch rates for micromachining processing," *Journal Of Microelectromechanical Systems*, vol. 5, pp. 256-269, 1996.
- [75] A. N. Broers, W. W. Molzen, J. J. Cuomo, and N. D. Wittels, "Electron beam fabrication of 80-Å metal structures," *Applied Physics Letters*, vol. 29, pp. 596-598, 1976.
- [76] A. N. Broers, J. M. E. Harper, and W. W. Molzen, "250-Å linewidths with PMMA electron resist," *Applied Physics Letters*, vol. 33, pp. 392-394, 1978.
- [77] A. Midha, L. Donaldson, G. Mills, J. M. R. Weaver, and H. Zhou, "'Float Coating': A Resist Coating Technique for Electron-Beam Nanolithography on Micromachined Substrates," *Unpublished*, 1997.
- [78] M. Reading, D. J. Hourston, M. Song, H. M. Pollock, and A. Hammiche, "Thermal analysis for the 21st century," *American Laboratory*, vol. 30, pp. 13, 1998.

2 Generic Probe

2.1 Fabrication Tools

A contact printer (by *Hybrid Technology Group*) was used for all of the photolithographic micromachining stages. This type of photolithography uses a shadow mask to produce optical images on a substrate. The mask is physically contacted to a surface and exposed with UV light. A photosensitive coating (Microposit³ S1818), which is a positive resist, is used as the imaging medium. The developer for this resist is AZ1400³ (1:1 developer:water). Minimum feature sizes down to 250 nm have been demonstrated using contact printing techniques [1], however for routine work over large areas a minimum feature size of 500 nm is commonplace. Different photolithographic levels were manually aligned using this machine with placement errors of approximately 10 μm .

Electron beam lithography (EBL) was performed using a *Leica*⁴ EBP5 5HR machine. This machine is a 100 kV vector scan model with a five inch, interferometrically positioned, stage. Vector scanning differs from simpler raster scanning in that the writing beam is directed only to the areas of the substrate to be exposed and so reduces writing times for sparse patterns. The writing fields are 800x800 μm with typical stitching accuracies of 50 nm. Minimum spot size is 12 nm at 100 kV which gives written feature sizes down to 25 nm. Patterns are held in software and are designed using a program called *Wavemaker*⁵ (WAM) which produces GDSII pattern files (an industry standard format). Write times are typically a few hours long depending on pattern density and dose. The machine is routinely run at both 50 kV and 100 kV. In general 50 kV (high beam current, larger spot sizes) is used for low resolution/large coverage patterns whereas 100 kV (low beam current, small spot sizes) is used for high resolution/small coverage patterns. The EBL machine is run with two different final aperture sizes (see Figure 2-1), large for 50 kV and small for 100 kV. This results in the electron beam having a better spot shape and greater depth of focus for 100 kV operation (at the expense of beam current) compared to 50 kV. Jobs times at 100 kV are roughly two to three times longer than equivalent jobs written at 50 kV.

PMMA (poly-methyl methacrylate) resists were used for all the electron beam work during this investigation. Two different varieties, *Aldrich*⁶ (120,000 mwt) and *Elvacite*⁷

³ Shipley, Humber Ave, Trading Estate, Coventry, UK.

⁴ Leica Lithography Systems, Clifton Rd, Cambridge, CB1 3QH.

⁵ Barnard Microsystems Ltd.

⁶ Aldrich Chemicals Co. Ltd, The Old Brickyard, New Rd, Gillingham, Dorset, SP8 4JL.

⁷ Elvacite - brand name belonging to Dupont.

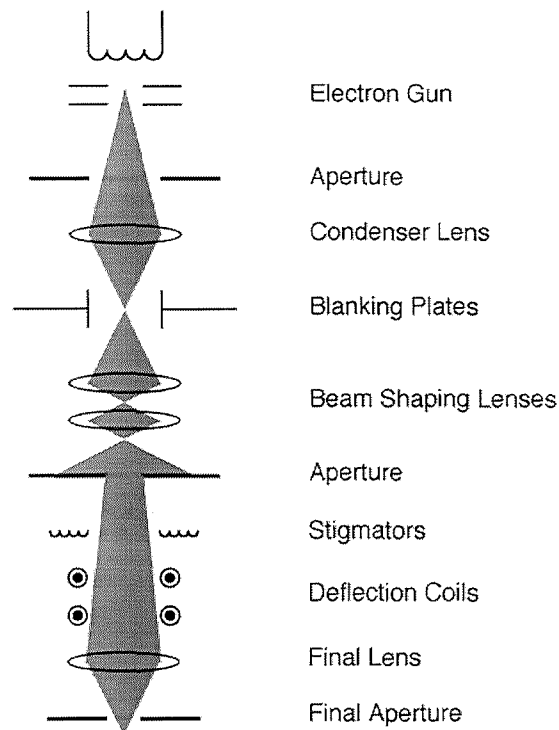


Figure 2-1 Representation of an electron lithography system.

(350,000 mwt) dissolved in orthoxylene were available. The resists were spun onto the substrates using commercial spinners at speeds of 2500 or 5000 rpm depending on the nature of the specimen. Concentrations of 2.5% up to 12% resist by weight were available in each variety of resist giving film thicknesses in the range 20 to 500 nm.

Typically the lithographic patterns for the probe fabrication were transferred into metal device layers, or metal masks for reactive ion etching (RIE). Metal deposition was carried out in an automatic *Plassys*⁸ MEB 450 evaporator. Six different metals (Au, Pd, Ni, NiCr, Ge, Ti) were available using this machine. The Plassys heats the metals using an electron gun (10 kV, 1 A) under a vacuum of 1×10^{-6} Torr and the thickness is measured with an accuracy of approximately 1 nm using a crystal detector. Specimen and metal source are situated approximately one metre apart in this evaporator which gives minimal heating of the specimen. This is important when the specimen is patterned with polymers such as PMMA which can reflow at 180 °C. Sputter coating was also used during the process to deposit Cr. This method uses a plasma to sputter atoms from a metal disc which then condense on the specimen to form a film of uniform thickness [2].

⁸ Plassys, 14 Rue de la Gare, 91630 Marolles-en-Harepoix, France.

Pattern transfer from resist into metal was achieved by using wet etching (Cr and NiCr) or “lift off” (Au, Pd, NiCr, Ti). Lift off is a technique whereby metal is evaporated directly onto a specimen after resist development [3]. Areas where the resist has cleared out allow the metal to stick to the specimen, but in all other areas the metal is removed as the underlying resist is dissolved in acetone.

Bulk silicon micromachining is used to define the probe bases, cleave lines, markers and pyramidal tips on the generic substrate. Accurate timed etching was achieved by using a custom made etching kit comprising 750 ml Quickfit reaction flask, *Eurotherm*⁹ temperature controller, twin Pt thermometer, *Electrothermal* heating mantle (with magnetic stirring) and water cooled reflux. Machined steel (corrosion resistant grade 316-S31) formed a two piece cover for the reaction flask which allowed access for a three inch wafer. KOH is an anisotropic etch for silicon etch stopping on the <111> plane for concave etch pits. The KOH solution was made by dissolving KOH pellets into ultrapure water to make 7 molar solution (increased by 5% due to compensate for potassium carbonate formation in air). For this solution, temperatures of 80-105 °C gave etch rates between 75±1 µm/hour and 255±1 µm/hr in the <100> direction. In order to etch convex features (like a pyramidal tip) a mixture of KOH + IPA (isopropyl alcohol) was used. Although the IPA is not miscible in KOH solution and forms a separate layer on top of the alkali, it changes the etch rate of certain fast etching silicon planes [4] which produces a desirable tip profile for convex pyramids [5].

RIE is routinely used to transfer metal and polymer patterns into silicon nitride. The metal masks are patterned using either photolithography, or electron beam lithography followed by lift off or wet etching. Using a *Plasma Technologies*¹⁰ BP80 machine with C₂F₆ gas (15 mTorr, 100 W), silicon nitride is etched at rates about 30 nm/min using a bias of -300 V.

Sacrificial dielectric layers were required during the micromachining process and, although the starting substrates were pre-coated on both sides with 100 nm thick silicon nitride deposited by low pressure chemical vapour deposition (LPCVD), it was necessary to perform dielectric deposition at Glasgow. The available resources dictated that plasma enhanced chemical vapour deposition (PECVD) silicon nitride was used. This form of silicon nitride is formed by reacting silane and ammonia gases in a glow discharge over a heated stage (300-350 °C). The resultant coating is high in hydrogen and oxygen

⁹ Eurotherm Ltd, Faraday Close, Durrington, Worthing, W Sussex, BN13 3PL, UK.

¹⁰ Plasma Technology Ltd, North End, Yatton, Bristol, Avon BS19 4AP, UK.

impurities and its properties differ from LPCVD silicon nitride in some respects (e.g. low resistance to hydrofluoric acid) yet remain similar in others (e.g. RIE rate using C_2F_6). Stress in PECVD nitride layers can be created during deposition and may relax later when the layer is micromachined. Stress of this nature is undesirable when making micro-levers such as AFM cantilevers and so the deposition parameters were optimised minimise stress [6].

2.2 Analysis Tools

Scanning electron microscopes were used routinely during this investigation. In all cases *Hitachi*¹¹ machines were used (S800, S900, S4500). All microscopes used field emission sources and were operated at a variety of accelerating voltages. Wafers of probes were examined after most steps in the fabrication process in order to check the quality of the lithography or etching. Normally only a few sites on the wafer were examined because of the possibility of contamination from oil in the chamber. It was found that a very low voltage (3 kV or below) was needed when imaging released Si_3N_4 cantilevers because the cantilever would bend due to charging. Even using low accelerating voltages, charging of the Si_3N_4 cantilever caused the image contrast to vary.

*Leica*¹², *Nikon*¹³ and *Zeiss*¹⁴ epi-illumination optical microscopes were used for the optical analysis of large scale features on specimens and probes. Image capture using CCD cameras was available and examples can be seen in later chapters. Nomarski interference contrast was used with some of the specimens to enhance topographic contrast.

A *Digital Instruments*¹⁵ atomic force microscope was used during part of this investigation. The microscope was capable of being used in both contact, tapping and lift modes. A modification to the electronics and scanning head allowed resistive thermal tips to be used. Sharp commercial silicon and silicon nitride AFM probes were also used for verifying the topographic images acquired with the blunter probes.

A *Micrion*¹⁶ focused ion beam system was used for both drilling holes in thermal specimens, and imaging metal grains. Implantation of gallium was a concern when preparing thermal specimens, because this can change the thermal properties of the

¹¹ Hitachi Scientific Instr, Merlin Bld, Hogwood Ind Est, Finchhamstead, Wokingham, Berks, UK.

¹² Leica Microsystems Holdings GmbH, Ernst-Leitz-Strasse, D-35578 Wetzlar, Germany.

¹³ Nikon UK, Haybrook, Halesfield 9, Telford, Shropshire TF2 4EW, UK.

¹⁴ Carl Zeiss Jena GmbH, Zeiss Gruppe, Tatzendpromenade 1a, 07745 Jena, Germany.

¹⁵ Digital Instruments, 112 Robin Hill Rd, Santa Barbara CA, USA.

¹⁶ Micrion Corporation, One Corporation Way, Centennial Park, Peabody, MA 01960-7990, USA.

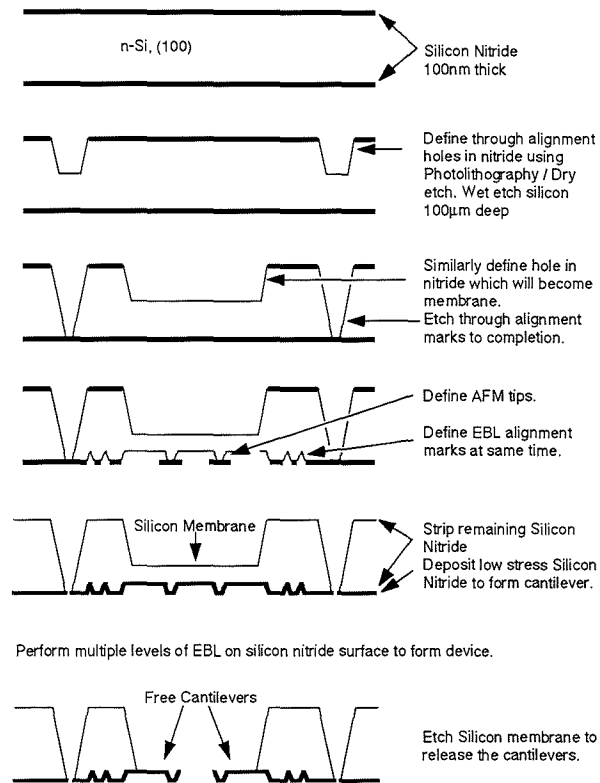


Figure 2-2 Micromachining levels from raw material to release.

specimen. A procedure of implanting a broad area before milling specific sites was recommended to equalise this effect [7].

Scanning Auger spectroscopy was performed to identify the contamination level of materials on a commercial thermal probe. The *Physical Electronics*¹⁷ machine was operated by B. Rogers of Motorola. Scanning Auger is routinely used for identifying light elements like oxygen, carbon and sodium. It was necessary in this case to use a sputtering beam to clean excess carbon from specimen surfaces before analysis.

2.3 Micromachined Substrate

The probe fabrication process for a generic probe is shown schematically in Figure 2-2. Initial KOH silicon etches on the reverse side of the wafer form individual probe bases and a thin silicon membrane. Photolithography masks for these levels were produced using electron beam lithography. Figure 2-3 shows WAM designs for the masks, and a processed wafer after the reverse side micromachining has been completed. All subsequent

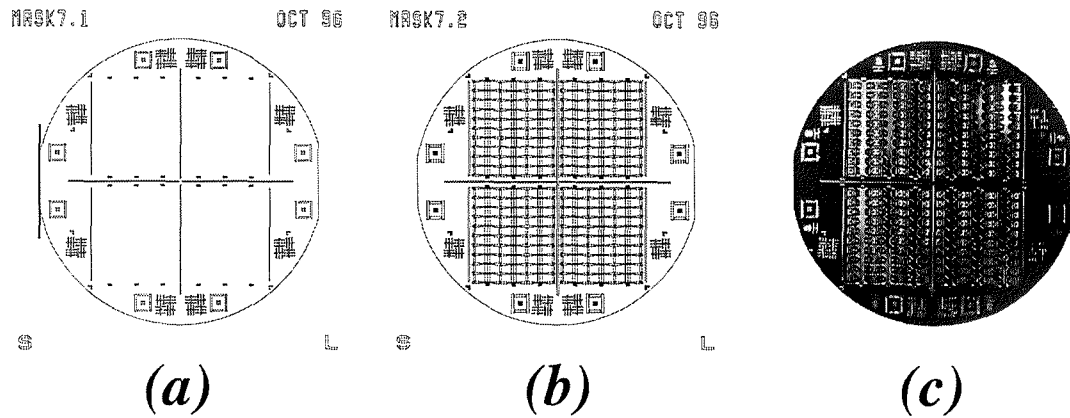


Figure 2-3 (a) CAD pattern for 1st photolithography mask containing cleave lines, etch through markers and course alignment markers. (b) CAD pattern for 2nd photolithography mask containing probe bases and membranes. (c) Photograph of wafer after etching of the 2nd photolithography pattern.

front side patterns are written directly onto the wafer using EBL. In order to align the front side EBL patterns to the micromachined probe bases and membranes, markers are patterned during the reverse side processing. Timing of the KOH etches then produces holes etched through the wafer to which the electron beam writer can align.

The first electron beam lithography level on the front side contains patterns for the

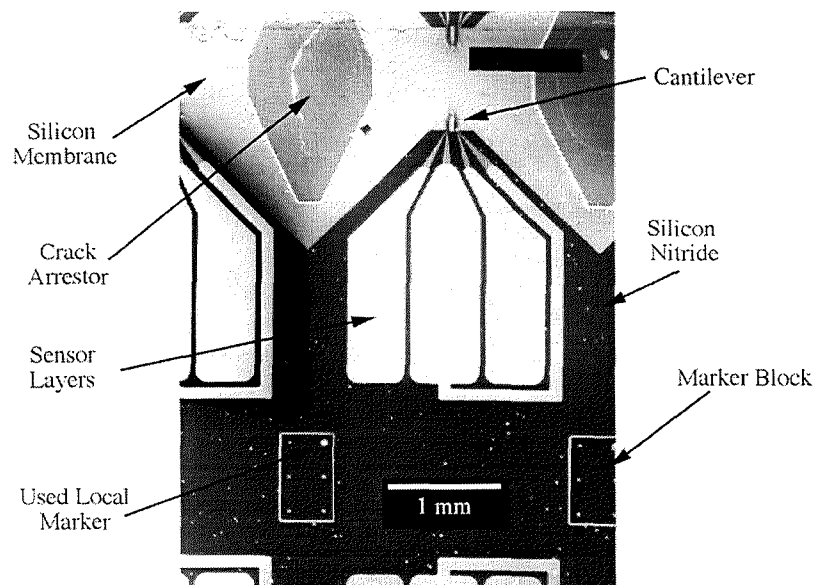


Figure 2-4 SEM of the front side of the micromachined substrate.

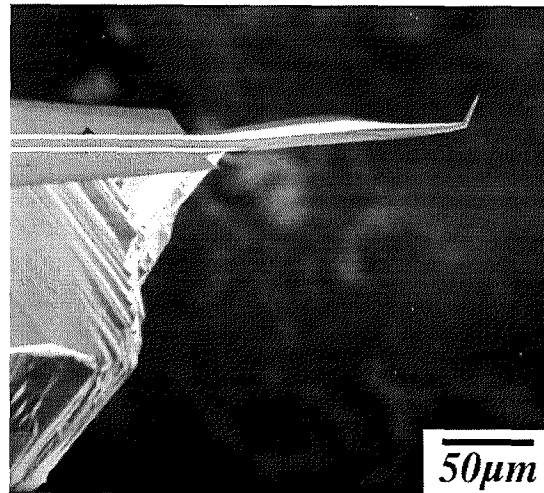


Figure 2-5 Side profile of the probe base - the different crystal planes form a complex shape.

pyramidal tips, local alignment markers and crack arrestors (see Figure 2-4). This pattern is lifted off in Ti before dry etching [8]. Timed wet etching in KOH+IPA is then carried out down to a depth of approximately 20 μm . This etch produces pyramidal tips, typically 30 μm at the base with 1-2 μm^2 flat tops. The pyramidal tips are positioned to be coincident with the membranes (etched earlier from the reverse), as are the crack arrestors (large unetched areas positioned at sites of weakness). At this point, local markers are patterned several millimetres away from the pyramidal tips on the probe base (so that they do not interfere when mounted for scanning). AFM tips are routinely mounted at angles of about 10° so the base does not foul the specimen. By etching these markers into the substrate at the same lithographic level as the pyramid tips, their positions are accurately defined relative to each other. This, among other things, determines the accuracy of alignment of later levels.

After the LPCVD silicon nitride and depositing a layer of PECVD silicon nitride on the front side of the wafer (500 nm thick, optimised for minimum stress), a 100 nm thick layer of chrome is sputtered on the front side of the wafer. EBL is used to pattern an appropriate cantilever shape that is subsequently transferred into the chromium layer using a chromium etch solution (ceric ammonium nitrate). RIE (BP80, C_2F_6) is then used to transfer the metal pattern into the underlying silicon nitride. After the wafer is cleaned to remove the sacrificial Cr and any remaining resist, the substrate is ready for the sensor layers.

The sensor may be patterned using any mix of the techniques described so far, provided that the materials used are compatible with a final KOH etch which releases the cantilevers (referred to as the “release etch”). The profile of a released probe is shown in Figure 2-5.

Note that the probe base is a complex shape due to the combined etching from front and back.

2.4 3D Lithography

Formation of reproducible sensors at the end of sharp tips was the main goal of this project, and several techniques specific to Glasgow had been developed to achieve this. Dr J. Weaver, A. Midha, Dr H. Zhou and Dr S. Thoms were the inventors of this technology which served to overcome problems encountered when using high resolution EBL to make the sensors. Problems involving resist coating, alignment, and focusing of the EBL tool were addressed.

Coating sharp objects with electron beam resists, in this case PMMA dissolved in o-xylene, became a major area of concern when it was discovered that the resist could not be spun over large convex features (such as pyramidal tips). The edges of such features remained uncoated regardless of spin speed, and so a resist coating method called “float coating” [9] was developed by the researchers at Glasgow. Figure 2-6 shows the present

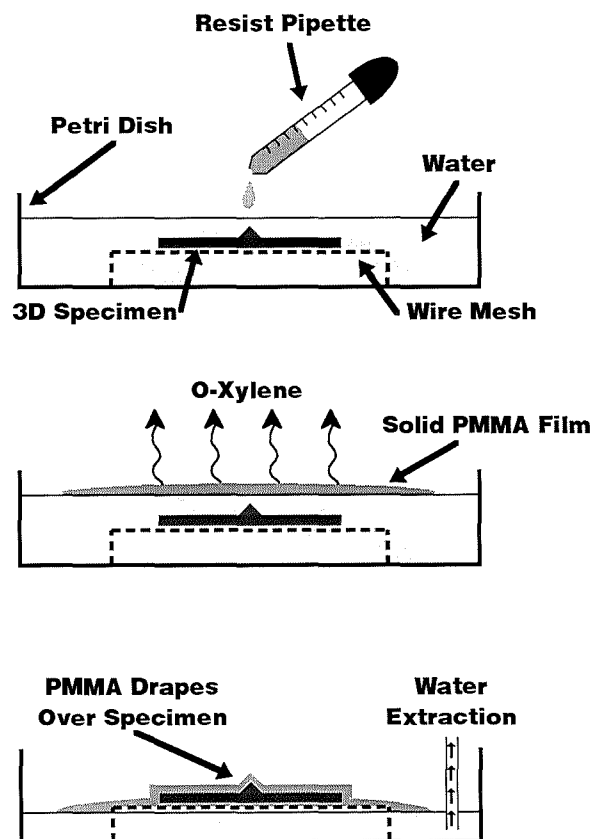


Figure 2-6 Float coating. A drop of PMMA in o-xylene is dropped onto water. The o-xylene evaporates to leave a solid film of plastic which is then draped over the substrate by removing the water.

technique used to float coat specimens, which was used for most of the work described in this document. The specimen is submerged in a dish of ultrapure water and a single drop of PMMA dissolved in o-xylene is allowed to fall onto the water surface. The o-xylene is immiscible in water and quickly spreads out over the water surface. Using water at room temperature, the o-xylene evaporates in 1 to 2 minutes leaving a continuous solid film of PMMA floating in the water surface. The size and thickness of the solid film is dependent on the concentration of PMMA and the dynamics of the drying process [10]. As the ultrapure water is then slowly removed, the film approaches the specimen and ultimately drapes over the specimen surface. Both flat and micromachined areas are coated with resist. In particular, the sharp edges of micromachined features (e.g. pyramidal tips) are well coated. Problems with “wrinkles” in the solid PMMA film have been observed. The density of the wrinkles appear to be dependent on the environmental conditions during evaporation of the o-xylene (e.g. temperature, air flow, humidity). A bake for 30 mins at 180 °C after the float coating removes any residual water from the specimen surface and takes the PMMA through its glass transition where it reflows to some extent and many wrinkles are removed. Some wrinkles do remain however and Figure 2-7 shows a potentially devastating wrinkle on a pyramidal tip. Although these wrinkles do not in general cause lithographic failure, this may be because the patterns used for the thermal sensors are sparsely distributed. Float coating may not be suitable for dense patterns.



Figure 2-7 Plan view of a micromachined pyramid which has been coated using float coating. A random wrinkle has coincided with the tip in this case and could potentially affect further processing.

Problems encountered when performing EBL on specimens with significant relief are varied. Refocusing the EBL machine is necessary in order to write a well resolved pattern away from the substrate plane. This involved modification of the control software and changes in the pattern to multiple matrices written at different focus. 100 kV operation was used for all writing away from the substrate plane because it provides greater depth of focus. An added benefit of using 100 kV was that the smallest writing spot (12 nm) was available for the sensor levels.

Alignment of the various lithographic levels to the pyramidal tip is achieved using etched topographic markers. These markers are patterned six to a block and etched in the same level as the pyramidal tips for maximum placement accuracy. Each pair of pyramidal tips has corresponding blocks of local markers (see Figure 2-4) which are in the form of pyramidal recesses in a rectangular mesa. The depth of the recesses and the height of the mesas are determined by the height of the pyramidal tips (typically 18-20 μm). In general the alignment accuracy of features to the pyramid using topographic markers was poor by

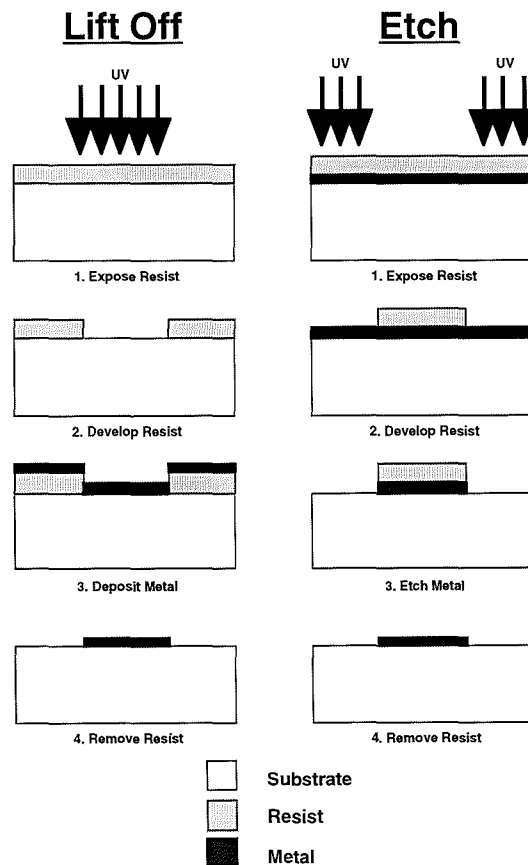


Figure 2-8 Lift Off (additive) and etching (subtractive) pattern transfer techniques.

EBL standards (≈ 250 nm). Problems with alignment of features will be discussed in more detail in Chapter 5.

2.5 Advanced Lift Off

Metal lift off was routinely used at the sensor definition levels of the process. In general, lift off will preserve high resolution features during pattern transfer better than etching processes (Figure 2-8). This is because etching tends to remove material laterally as well as vertically which causes shrinking and rounding of fine features. Lift off, in contrast, is used to remove metal which has been evaporated vertically onto the substrate and so the pattern should be perfectly preserved. Theoretically, removal of metal during lift off is a trivial and consistent process because there is no physical attachment between the metal

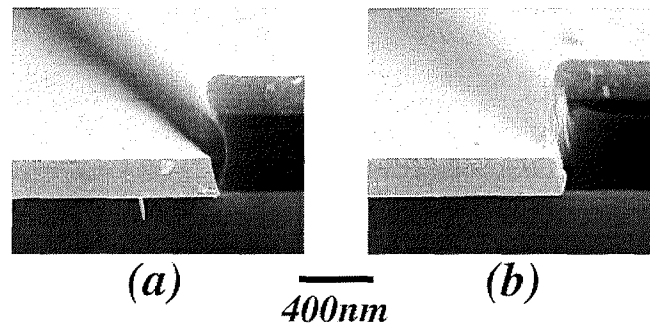


Figure 2-9 (a) Undercut resist profile with 200 nm of metal evaporated on top. (b) Overcut resist profile with 200 nm of metal evaporated on top. Note how the metal film is continuous in (b) but not in (a). Micrographs courtesy of Fraser Williamson, University of Glasgow.

pattern which stays on the substrate and the surplus metal which is removed. In practise the removal of surplus metal is far from trivial and unwanted pieces of metal (called “flags”) often fail to detach from the exposed features. The reason for poor lift off is that vertical resist profiles are difficult to achieve. Depending on development conditions, resist profiles can vary from undercut (desirable) to overcut (undesirable). Figure 2-9 shows examples of different metalised resist profiles. Where the resist profile is overcut, the metal film is continuous and may cause flags. The metal film however is weaker at the joins, and so when the underlying resist is removed, the surplus metal can tear away giving successful lift off. Conventional methods which improve lift off include physical agitation using ultrasonic bursts or “shooting” using micropipettes (a manual technique [3]).

The problem of poor development causing flags is acute for the lift off of the sensor levels positioned on the micromachined pyramidal tips. Different matrices in the EBL patterns are written to be in focus only on the substrate plane and at the tip apex, and so the electron beam is imperfectly focused on the sides of the pyramids where the matrices overlap. The result of this is that trivial feature growth is observed on the sides of the pyramids and the electron dose at feature edges is reduced due to broadening of the writing spot. Optimum development of this pattern is difficult to achieve because of the variations in dose over the pyramid. Flags and metal caps on the pyramids are common. An additional lift off aid for 3D substrates was developed involving the patterning of sacrificial features which facilitate the tearing mechanism of metal removal. These sacrificial features take a variety of forms depending on the nature of the pattern. For example, it was observed that lift off of a single metal wire bisecting a micromachined pyramid was in general successful. It was also observed that if a wire was patterned up the pyramid and terminated near the apex, then in general the metal failed to lift off from the pyramid apex and formed a cap (see Section 5.2 for further information).

Three examples of sacrificial features which improve lift off on pyramidal tips are shown in Figure 2-10. In Figure 2-10(b) a triple thermocouple device is shown where three Pd wires bisect a single Au wire at the apex of a pyramidal tip. Spatial constraints affected how many pads for electrical connection may be patterned, and so each of the four wires is single terminal. Instead of terminating the wires at the pyramid apex, the wires extend over to the other side of the pyramid. After some pattern optimisation (see Chapter 4) lift off yield for this complex pattern approached 90% and virtually eliminated occurrences of capping.

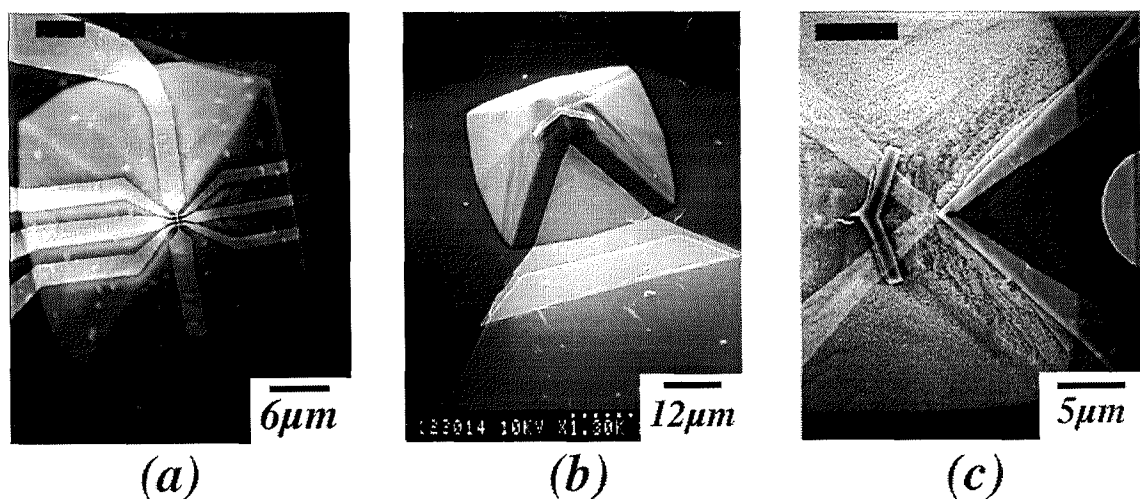


Figure 2-10 (a) Triple thermocouple probe. (b) Triangular cantilever shape for an improved access probe. (c) An improved access thermocouple probe pre-release.

Figure 2-10(b) shows a sharp triangular shape lifted off in metal on the side of a pyramidal tip. The purpose of the metal is to mask underlying silicon nitride during RIE. The silicon nitride that remains after etching forms the AFM cantilever. An “L” shaped feature has been patterned here at the tip apex to aid lift off. This feature provides an extra region where the metal on the tip may tear, and it was found that lift off of the triangular feature was greatly improved. Although the “L” shaped feature remains after RIE etching, it floats away in the release etch because it has no attachment to the cantilever.

A final example is shown in Figure 2-10(c). Here, the thermocouple wires for a probe have to coincide with a triangular shaped cantilever on the side of a pyramidal tip. In similar fashion to the triple thermocouple device, the wires are not terminated on the pyramid (as was first intended), but are extended over to the opposite side. This time the wires do not run over the tip apex, but nevertheless improved lift off yield significantly.

2.6 Evolution of Generic Processing

Several advances in the fabrication of the generic probe were made during this project, the most important of which were as follows. Firstly, a capping layer was introduced after the cantilever definition layer. This was to offset the fact that despite being an isotropic form of metal coating, the sputtered Cr film that formed the dry etch mask was not continuous. The film appeared not to cover the apices of the pyramids and formed a star shaped hole like that shown in Figure 2-11. After dry etching, the unprotected silicon nitride at the tip apex was etched, which rendered the cantilever useless for further modification. The capping layer consisted of an extra, low resolution, level of lithography consisting of a square over the pyramidal tip. This pattern was lifted off in thin $\text{Ni}_{0.6}\text{Cr}_{0.4}$ to form an extra



Figure 2-11 SEM of the apex of a pyramidal tip coated with 100 nm Cr. Note the star shapes region which has remained uncoated.

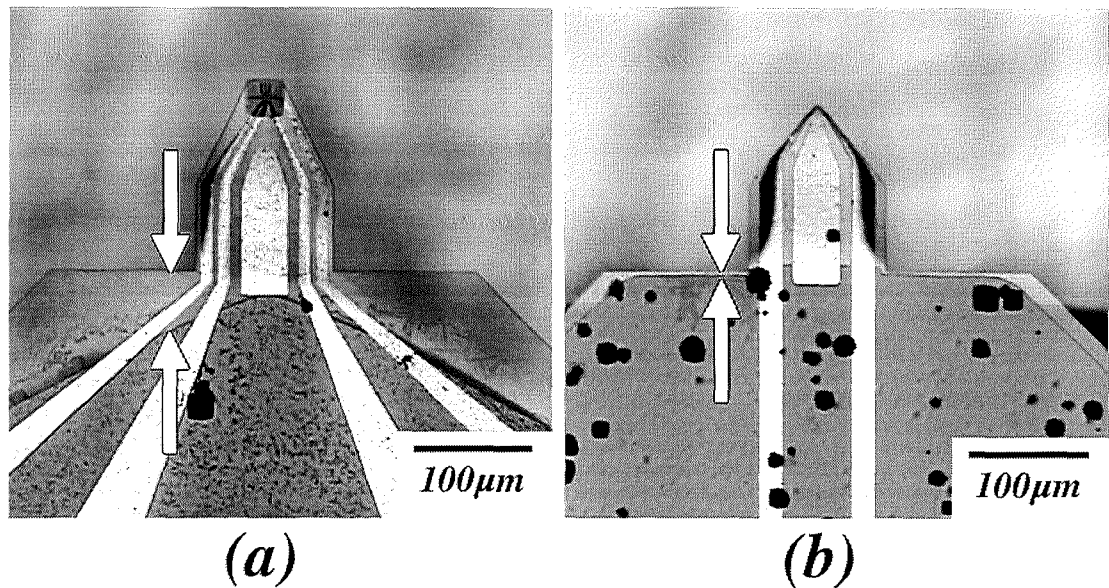


Figure 2-12 (a) Cantilever released in KOH. (b) Cantilever released in KOH+IPA. Arrowed regions show where the silicon base has receded badly with etch (a) but not with etch (b).

dry etch protection layer for the affected area. The use of thicker Cr layers, or a bilayer of sputtered and evaporated metal, may eventually result in the elimination of this process.

The release etch was also changed during the lifetime of this project. Exact timing of the KOH release etch was required to ensure that the probe base receded to exactly the bottom of the cantilever. A top priority however was to ensure that all the silicon had been removed from inside the pyramidal tip, and so the probes were often deliberately over-etched. Figure 2-12(a) shows a released probe that has been undercut, resulting in a weakened cantilever. This often led to cracks evolving at the base of the cantilever due to the lateral forces experienced during AFM scanning. In order to alleviate the problem, Dr H. Zhou substituted the KOH with a KOH/IPA etch solution similar to that used in the pyramid etch. This etch solution was known to slow the etch rates of certain fast etching planes in silicon [4], and the resulting profile showed a marked improvement over the pure KOH solution. Figure 2-12(b) shows a cantilever released in the KOH/IPA solution. Note the squarer profile of the silicon at the cantilever base, which gives enhanced lateral stiffness and reduced stress concentration at the cantilever base.

- [1] B. J. Lin, "Deep uv lithography," *Journal Of Vacuum Science & Technology*, vol. 12, pp. 1317-1320, 1975.
- [2] S. M. Sze, *VLSI Technology*: McGraw-Hill, 1988.

- [3] S. P. Beaumont, P. G. Bower, T. Tamamura, and C. D. W. Wilkinson, "Sub-20-nm-wide metal lines by electron-beam exposure of thin poly(methyl methacrylate) films and liftoff," *Applied Physics Letters*, vol. 38, pp. 436-439, 1981.
- [4] K. R. Williams and R. S. Muller, "Etch rates for micromachining processing," *Journal Of Microelectromechanical Systems*, vol. 5, pp. 256-269, 1996.
- [5] A. Midha, "Batch-fabrication of novel nanoprobes for SPM," in *Electronics & Electrical Engineering*. Glasgow: University of Glasgow, submission due 1999.
- [6] S. Hicks, "Low stress PECVD silicon nitride.," University of Glasgow, Personal communication, s.hicks@elec.gla.ac.uk.
- [7] G. Harris, *Motorola MRST*, Private communication 1998, Gari.Harris@motorola.com.
- [8] A. Midha, S. K. Murad, and J. M. R. Weaver, "Anisotropic pattern transfer of fine resist features to silicon nitride via an intermediate titanium layer," *Microelectronic Engineering*, vol. 35, pp. 99-102, 1997.
- [9] A. Midha, L. Donaldson, G. Mills, J. M. R. Weaver, and H. Zhou, "'Float Coating': A Resist Coating Technique for Electron-Beam Nanolithography on Micromachined Substrates," *Unpublished*, 1997.
- [10] P. Ball, "Fluid dynamics - How coffee leaves its mark," *Nature*, vol. 389, pp. 788, 1997.

3 Instrumentation

3.1 Construction of an AFM

A flexible microscope was built for the testing and scanning of the functionalised AFM probes. Initial design and construction was performed by Dr J. Weaver and A. Midha. Commercial optics, mounted on a vibration isolated optical bench, were used to make the force detection system. The instrument evolved from its initial role of scanning SNOM probes (developed by A. Midha, and latterly Dr H. Zhou and L. Bruchaus), where a key feature was the illumination of aperture probes using a high numerical aperture (NA) objective. This approach was intended to provide maximum illumination intensity at the SNOM apertures. The choice of objective meant that beam deflection [1, 2] could not be used for force detection since it proved impossible to steer a laser beam past a 0.5 NA objective onto a generic cantilever. This was due to blockage by either the objective casing, or the silicon probe base. An interferometric method for force detection was chosen instead [3, 4], in which the SNOM pump and force detection laser beams follow the same path through a single objective. A common path heterodyne interferometer was used for the force detection, giving shot-noise limited sensitivity to cantilever deflection and insensitivity to thermal drift. Laser light for the interferometer was divided and frequency shifted using a Bragg cell. Significant latter simplification of the instrument for SThM involved the removal of the SNOM pump optics, however the original interferometric force detector was retained.

The optical system used for the thermal microscope at Glasgow is shown schematically in Figure 3-1. The light source (Argon ion, 514 nm, 15 mW) is directed through a Bragg cell which both splits the beam in two, and frequency shifts one beam by the acoustic

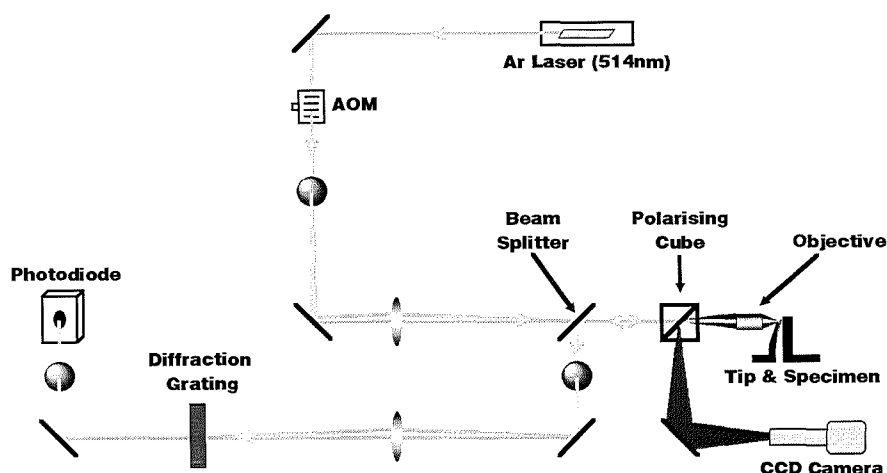


Figure 3-1 Thermal microscope optics (modified diagram from original by J. Weaver).

frequency (72 MHz in this case). A schematic of the Bragg cell is shown in Figure 3-2. It operates by passing acoustic vibrations originating from a piezo-electric transducer through an optically transparent medium (typically SiO_2 or TeO_2). The acoustic wave causes a spatial variation of refractive index in the optical medium, which may be controlled by altering the acoustic power. Optimum diffraction occurs if the angle of incidence is set to the Bragg angle,

$$\theta_B = \sin^{-1}\left(\frac{\lambda}{2\Lambda}\right)$$

Where λ is the frequency of the light and Λ is the acoustic frequency in the Bragg cell. At this angle a sharp first order diffraction maximum is observed. The first order transmission experiences a frequency change equal to the driving acoustic frequency. This effect may be described as a Doppler shift [5] which results from reflection from a moving diffraction grating. In this way, the two beam light beams of different frequency needed for heterodyne interferometry are created. The difference in frequency, $\Delta\omega$, is called the intermediate frequency (IF). In order to get two equal intensity beams for interferometry, the acoustic power is set so that approximately 50% of the laser is diverted away from the normal optical path into the first diffraction order.

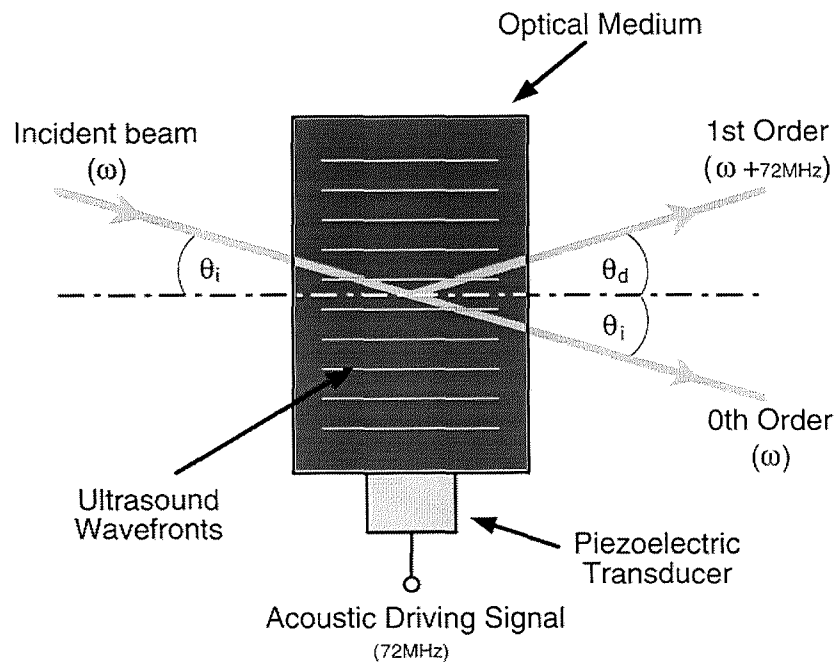


Figure 3-2 Schematic of a Bragg cell. Optimum diffraction occurs when $\theta_i = \theta_d = \theta_B$ the Bragg angle.

After splitting and frequency shifting by the Bragg cell, the interferometer beams are guided onto the cantilever using the objective lens. The beams are positioned such that one beam illuminates the fixed end of the cantilever and the other the free end. With constant cantilever deflection, a constant phase difference is maintained between the two laser beams. When the cantilever is contacted to a surface however, the resulting deflection causes a change in phase difference between the two beams. Such movements are detected by optically mixing the two reflected beams to produce a signal at the IF. Further electrical mixing with a reference signal at the IF produces a dc signal proportional to the phase of the original reflected laser beams. Since this phase is determined by the cantilever deflection, the dc signal may be used as a measure of the force of contact of the AFM cantilever with a surface.

Optical mixing after reflection from the cantilever is performed by guiding the interferometer beams onto a metallic transmission grating. The period of this grating varies in one dimension and adjusting the position and rotation of the grating makes it possible to make the two beams coincide. The coincident beams are focused onto a photodiode where they beat together to produce a signal at the IF. Electrical demodulation using two orthogonal reference signals produces dc signals proportional to the cantilever deflection (sine and cosine of the optical phase difference). Passive power splitters and double balanced mixers from *Minicircuits*¹⁸ were used to construct the demodulation circuit. The photodetector and demodulation electronics were housed in close proximity (in the same shielded container) to limit electromagnetic interference from the nearby Bragg cell drive signal.

Mechanical scanning of the probe was implemented using a commercial 3-axis flexure stage¹⁹ with piezoelectric actuators. The piezoelectric actuators operate from 0-150 V and produce a maximum travel of 13.5 μm . Micrometer screws provide coarse manual alignment over a 2 mm range. To simplify the alignment of the laser beam to the probe, the tip was fixed and the specimen scanned. Both tip and specimen were mounted on custom made holders. Two CCD (charged coupled device) cameras were introduced to help during the alignment of the laser beams to the cantilever, and the approach of the tip to the specimen. The optical path of the primary camera was coincident with that of the interferometer, and a polarising beam splitter cube was used to separate the laser from a white light source (Figure 3-1). A small proportion of the laser intensity is diverted to the CCD camera using this set-up, however this was required for the alignment procedure. A coloured filter was used to attenuate the laser light so as not to saturate the camera. The

¹⁸ Minicircuits, PO Box 350166, Brooklyn, New York, USA.

¹⁹ Elliot Scientific, Gladstone Pl, 36-38 Upper Marlborough Rd, St Albans, Herts, UK.

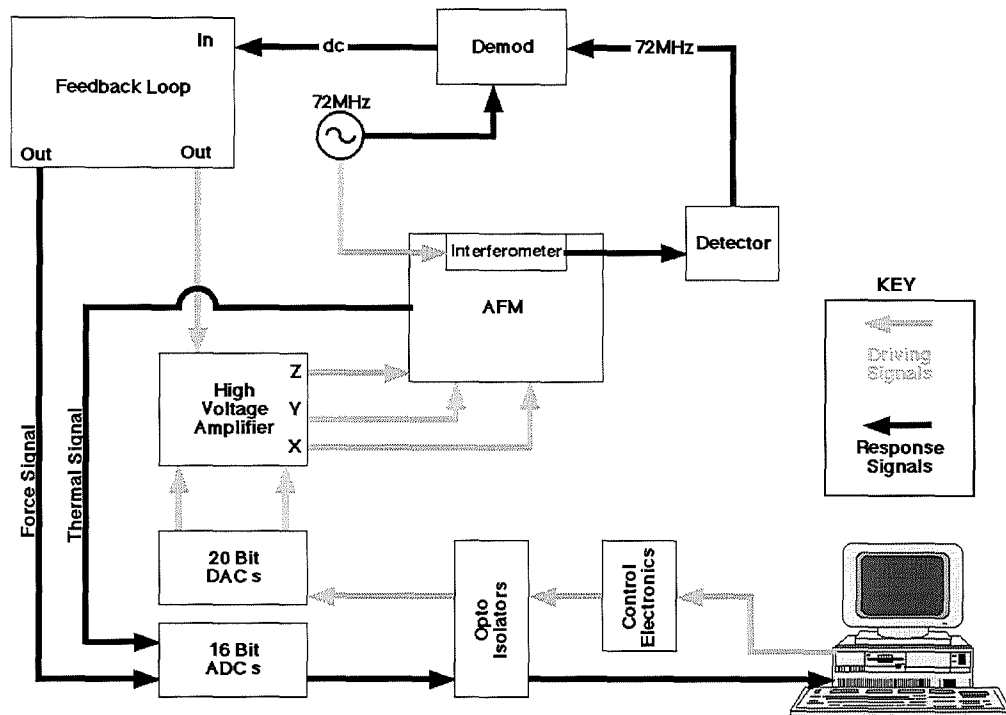


Figure 3-3 Block diagram of the electronics for the contact mode AFM.

purpose of the second camera (not shown in Figure 3-1) was viewing light transmission through SNOM apertures, and was thus seldom used for SThM.

3.2 AFM Control Electronics

A schematic diagram of the control electronics for the AFM is shown in Figure 3-3. Most of the component parts shown predated this project and were designed and built by Dr J. Weaver. Scanning software was written by a fourth year project student²⁰. Computer assembly and software modification were carried out by the author.

The operation of the system mimics in part an older attractive mode AFM system used for potentiometry. A computer interacts with the AFM through digital to analogue, and analogue to digital converters (DACs and ADCs respectively). The DACs drive the XY raster scanning motion, whereas the ADCs collect information from the microscope which is then plotted on the computer monitor. The feedback loop (single pole integrator) serves on the signal from the optical interferometer which is proportional to the cantilever deflection. High voltage (-150 to +150 V) amplifiers convert the computer generated raster

²⁰ Project Student 1994, Department of Electronics and Electrical Engineering, University of Glasgow.

motion, and Z height corrections from the feedback loop, into drive signals for the piezoelectric transducers.

The computer used to drive the microscope was assembled from commercial components. A fast processor (P150) and hard disk were required because experience of the older potentiometric AFM had shown that disk write delays limited rapid data acquisition rate. For attractive mode AFM this was not so critical, since scanning is generally limited by settling delays of the feedback loop. Contact mode AFM on the other hand, where fast initial scans are used to give rough positional information, often allows the user to scan at faster frequencies. Some important elements of the older system were retained however. The software for scanning was written in 1994 by a final year project student and later updated by Ashish Midha. An early generation SVGA (8514A) video card was used in conjunction with a modern SVGA card to provide the user with a twin monitor environment. To avoid having to configure the software for new hardware, the new computer was fitted with an identical 8514A card. Few problems were encountered when fitting this antiquated card to a modern motherboard, however care had to be taken in selecting a compatible monitor (the pin outs on SVGA cables vary depending on what degree of auto-detecting is employed). The computer was electrically isolated from the rest of the microscope in order to break the ground connection between microscope and computer thus avoiding noise transmission.

The original system used an obsolete DAC/ADC card to drive the microscope (14 bit DACs, 14 bit ADCs). Although a duplicate card was available, it was not compatible with the Pentium processor bus speed and so a modern I/O card was used instead to drive external DACs and ADCs (20 and 16 bit respectively). The new DACs differed from those on the original DAC/ADC card in that they were serial-in/parallel-out (the original DACs were parallel-in/parallel-out). A hardware solution to this compatibility problem was engineered by Dr Weaver involving a series of parallel-in/serial-out shift registers and some control logic. Subroutines in the Pascal code controlling data streaming to the DACs were written by the author.

The AFM was tested on completion to check that force regulation was operating adequately. Topographic scans were acquired using both “blank” Si₃N₄ Glasgow generic cantilevers (no defined sensor) and commercial silicon cantilevers from *Nanosensors*²¹. The specimen used here was fabricated by Dr J. Weaver using high resolution EBL and consisted of twin orthogonal metal gratings patterned on a Molybdenum coated Si substrate. A short (1 μm) period grating was evaporated first using 20 nm Al, then a

²¹ Nanosensors GmbH, IMO-Building, Im Amtmann 6, D-35578 Wetzlar-Blankenfeld, Germany.

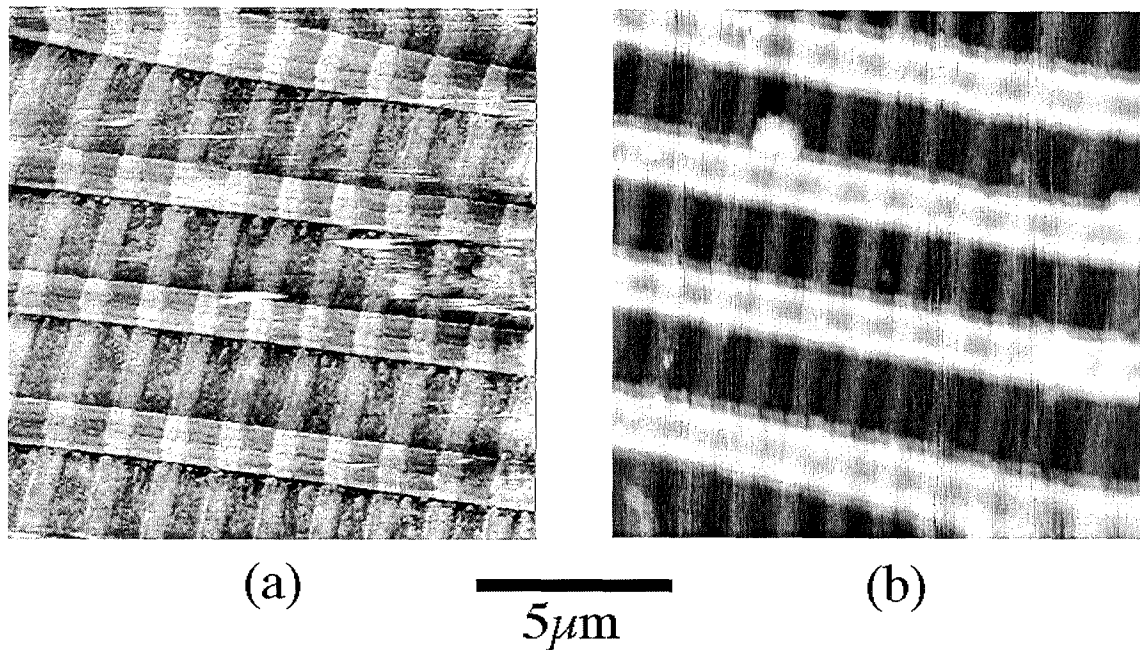


Figure 3-4 (a) Topographic scan of perpendicular metal gratings on glass using a generic probe. (b) The same specimen scanned using a sharp commercial silicon tip.

longer ($3\ \mu\text{m}$) period grating was deposited on top using $50\ \text{nm}$ AuPd. AFM scans of the gratings can be seen in Figure 3-4. Reflection of the laser beams from the Glasgow probe was aided by evaporation of $20\ \text{nm}$ Al on the reverse of the cantilever. The scans clearly show the orthogonal gratings. The difference in contrast between the two images is due to the superior specimen access afforded by the sharp Si tip. Although high resolution information is observed using the Glasgow probe, the flat apex tip ($\approx 1.5 \times 1.5\ \mu\text{m}$ top, 35° half angle) does not allow the tip to faithfully trace the surface. This is a common artefact in SPM, resulting in image contrast being governed by the tip shape. The image using the sharp silicon tip is expected to be a truer representation of the specimen due to improved specimen access ($10\ \text{nm}$ tip radius, 15° half angle). This would appear to be the case since the commercial probe gives stronger contrast (the tip is accessing the trenches between wires), and more consistent with the evaporated thicknesses (the signal at the thicker horizontal wires is greater than that at the vertical wires).

Despite the poorer topographic imaging capability of the Glasgow probes compared with a conventional AFM probe, the strategy of using AFM to position integrated thermal sensors is still valid. The primary objective of using the force signal is to navigate a specimen, and thus accurately overlay the simultaneous thermal image. The image in Figure 3-4 is certainly good enough for this purpose, with topographic features in the image resulting from structures no more than $1\ \mu\text{m}$ from the sensor.

3.3 Thermocouple Circuitry

Special care was taken when designing the methods for physical mounting and electrical connection of the miniature thermal probes to an external amplifier. Initial efforts to make electrical connection to thermocouple probes by Dr H. Zhou had shown that the probes were sensitive to electrostatic discharge (ESD). Calculations estimate that only 3 pJ of energy would be required to vaporise a typical 100x100x75 nm metal thermocouple junction (assuming the failure mode is melting, neglecting the possibility of the metals forming a eutectic, and using 1336 °K as the melting temperature of Au). This corresponds to the discharge from a 15 mm length of a coaxial cable with lead capacitance 100 pF/m charged to 15 V (typical situation for a floating input to an opamp). The chosen strategy therefore involved several features designed to reduce the likelihood of electrical failure of the probes on contact to external circuitry.

Angled aluminium probe mounts had already been manufactured for use with the contact mode AFM described earlier. In order to keep connections short, it was decided that the thermal probes should be mounted on a small printed circuit board (PCB) which would then be glued onto the aluminium holder. The PCB included copper pads to which the thermocouple wires could be electrically connected, and featured a single pole low pass filter (-3 dB breakpoint approximately 30 kHz depending on probe resistance) made from surface mount resistors and capacitors. The purpose of the filter was to protect the probe from high frequency signals arising from discharges due to lead capacitance or amplifier transients. The close proximity (approx. 1 cm) of the filter to the thermocouple probe provided minimum lead capacitance. In most cases, it was expected that the thermocouple signal would be dynamically detected using a homodyne detector (i.e. the temperature of the specimen would be modulated). Pre-amplification of the thermocouple signals (of order 10 μ V) was employed before input to a lock-in detector so that noise pickup and impedance mismatches would be minimised. An instrumentation amplifier (*Burr Brown*²² INA114) was chosen for its high CMRR and suitable bandwidth (10 kHz at gain = 100). The amplifier needed to be situated physically close to the probe to decrease lead capacitance, and so was mounted on a small separate PCB and connected using short (\approx 15 cm) insulated wires. Surface mount components were used on the amplifier board in order to keep signal paths to a minimum. The buffer amplifier output was connected to the lock-in amplifier using coaxial cable. A photograph of both the probe mount and amplifier board are shown in Figure 3-5.

²² Burr Brown, www.burr-brown.com.

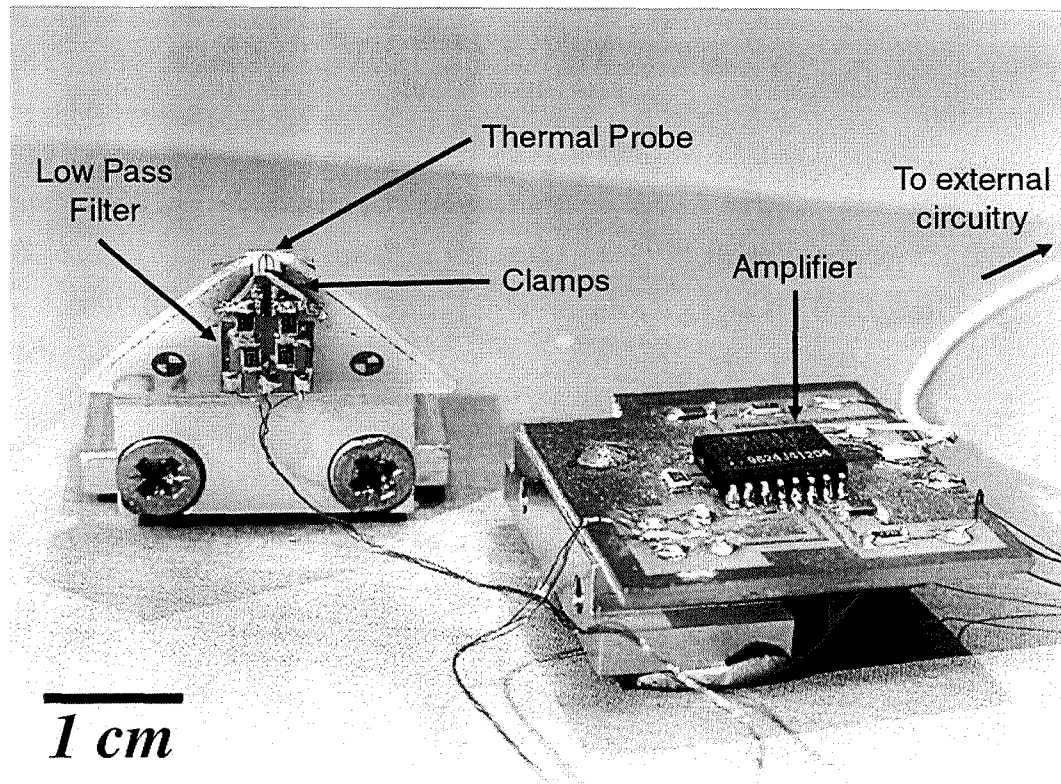


Figure 3-5 Thermal probe mount with passive filter and amplifier board.

Bonding the thermocouple wires to the circuitry was attempted using a mix of techniques. Initially ultrasonic bonding with aluminium wires was used, which involved precise alignment of a metal wedge to the probe. This method was successful, although time consuming due to the fact that many bond wires failed to stick to either the thermocouple wires or the copper pads on the PCB. The adhesion problems seemed to be caused by contamination and the height mismatch between the probe pads and the PCB (equal to the probe base thickness). Cleaning the PCB in hydrochloric acid prior to bonding increased the number of good bonds made to the PCB, however cleaning the probe was not possible due to the fragility of the cantilever. Latterly, silver epoxy was used to secure hanging bonds, although this technique risked damage to the cantilever. An additional strategy designed to protect the probe from ESD involved making bonds between the thermocouple wires to short circuit the sensitive junction. These bonds could be left in place until the amplifier had been connected and powered up, before being cut using an insulating knife.

In order to improve on the bonding method for electrical connection of the probes, a clip system was devised (shown in Figure 3-5). Two tiny sharpened beryllium copper strips were soldered to the existing probe mount PCB, then shaped into angled clips using tweezers. The sharp ends of the strips were positioned to rest on with the thermocouple pads on the probe base. A third metal strip was used to raise the two clips while the probe

was placed underneath. Annealed beryllium copper has similar mechanical properties to spring steel and electrical conductivity almost as high as copper. This provides a low resistance path and means the clips do not deform during the mounting operation. A small piece of wire (≈ 1 cm long) was temporarily used to short the two clips together during mounting and connection to the rest of the amplifier circuitry. It was cut after the amplifier had been powered up using an insulating knife.

- [1] G. Meyer and N. M. Amer, "Novel optical approach to atomic force microscopy," *Applied Physics Letters*, vol. 53, pp. 1045-1047, 1988.
- [2] S. Alexander, L. Hellemans, O. Marti, J. Schneir, V. Elings, P. K. Hansma, M. Longmire, and J. Gurley, "An atomic-resolution atomic-force microscope implemented using an optical-lever," *Journal Of Applied Physics*, vol. 65, pp. 164-167, 1989.
- [3] Y. Martin, C. C. Williams, and H. K. Wickramasinghe, "Atomic force microscope force mapping and profiling on a sub 100-Å scale," *Journal Of Applied Physics*, vol. 61, pp. 4723-4729, 1987.
- [4] Y. Martin and H. K. Wickramasinghe, "Magnetic imaging by force microscopy with 1000-Å resolution," *Applied Physics Letters*, vol. 50, pp. 1455-1457, 1987.
- [5] H. Cummins, N. Knable, L. Gampel, and Y. Yeh, "Frequency shifts in light diffracted by ultrasonic waves in liquid media.," *Applied Physics Letters*, vol. 2, pp. 62-64, 1963.

4 Thermocouple Probes

4.1 Thermoelectricity

A thermocouple thermometer is an electrical circuit consisting of at least two dissimilar conducting elements. Three related thermoelectric effects govern the operation of a thermocouple. If a temperature gradient exists between the junctions of two dissimilar conducting elements (see Figure 4-1(a)), then an emf is produced which may drive current round a closed loop. This phenomenon is called the Seebeck effect, named after Thomas Johann Seebeck to whom the discovery is attributed. The absolute Seebeck coefficient (ASC), or absolute thermoelectric power, (S) of an individual element in a closed circuit may be described as

$$S(T) = \int_0^T \frac{\sigma}{T} dt$$

Where σ is the Thomson coefficient of the material and T is absolute temperature. The algebraic sum of the ASCs of individual thermoelectric elements in a circuit produces the relative Seebeck coefficient (RSC) of the thermocouple. The open circuit RSC of a thermocouple is given by (see over)

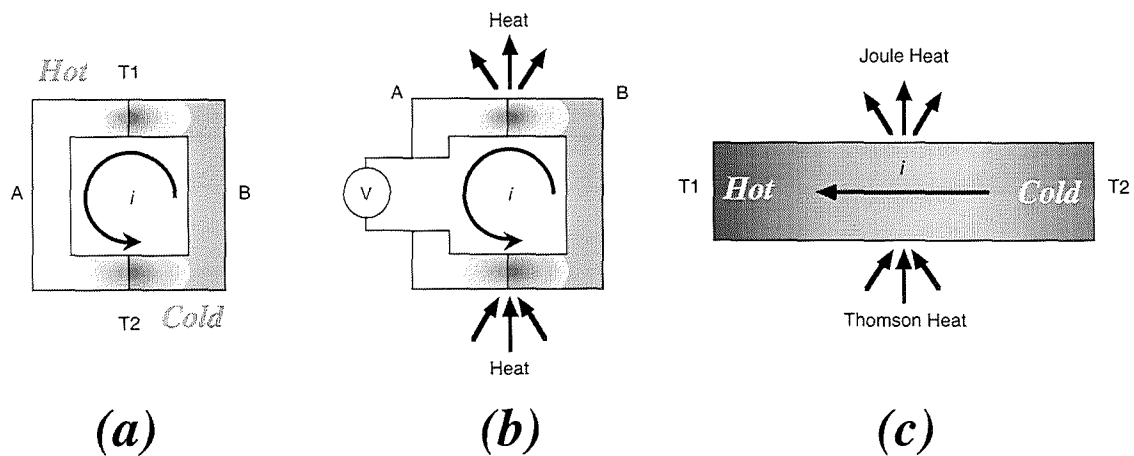


Figure 4-1 (a) If materials A and B are different conductors then the Seebeck effect produces an emf that drives a current i proportional to the temperature difference of the junctions. (b) If A and B are dissimilar conductors, and a current i is driven round the closed circuit, Peltier heating will occur at one junction and Peltier cooling at the other. Reversing the direction of the current flow changes the direction of energy flow at the junctions. (c) Thomson heat is the reversible heat absorbed or evolved (dependent on direction of current) when a current passes through a single conductor subject to a temperature gradient. This is additional to any resistive joule heating which is not reversible.

$$\frac{dE_{AB}}{dT} = S_A - S_B$$

Where E_{AB} is the emf produced by a thermocouple made from materials A and B . S_A and S_B are the ASC's (normally measured in $\mu\text{V}/^\circ\text{C}$) of the individual conductors. The emf in a thermoelectric element subject to a temperature gradient is caused by a voltage which retards the thermal diffusion of electrons from hot to cold areas. In addition to this, the Fermi level of element varies with temperature which produces a second voltage contribution. This combination of voltages produces the driving emf for thermocouple circuits. A complete quantum mechanical analysis of the origin of these effects is beyond the scope of this text but is described in full elsewhere [1-3].

The Peltier heat was named after Jean Charles Peltier who discovered the effect in 1834. He observed that passing a current across the junction of two dissimilar materials resulted in heating or cooling at the junction depending on the direction of current flow. In a circuit consisting of two dissimilar conductors as in Figure 4-1(b), energy is liberated at one junction and, if the circuit is isothermal, the same amount of energy is absorbed at the other. The Peltier coefficient P_{AB} , with current passing from material A to B , may be expressed simply as

$$P_{AB} = T(\sigma_B - \sigma_A)$$

Where T is the absolute temperature of the junction and σ_A and σ_B are the Thomson coefficients of the two conductors A and B .

Finally, the Thomson effect is the reversible heat produced when a current is passed through a conductor which is subject to a temperature gradient. This phenomenon was proposed by William Thomson (later Lord Kelvin) to complete a thermodynamic theory of thermoelectricity [4], and later measured experimentally for a variety of materials [5]. Reversible heat is energy that is liberated or absorbed depending on direction of current flow. This heat is additional to the Joule heat which is always liberated. The heat energy Q produced per unit volume per unit time in the conducting element in Figure 4-1(c) is given by

$$Q = j^2 \rho \pm \sigma j \frac{dT}{dx}$$

Where j is the current density, ρ is the electrical resistivity of the thermoelement, and σ is the Thomson coefficient. The first term is the Joule heating, but the second term (the

Thomson heat) may be positive or negative depending on the direction of the current flow with respect to the temperature gradient.

Both the Thomson and Peltier heats are closed circuit effects (they require current flow) and may produce errors in thermoelectric thermometry. Most practical thermocouple circuits however are usually operated open loop or with negligible current flow, and so these effects may be ignored. Errors may also occur with the introduction of electrical leads for the purpose of measurement [6, 7]. These may be avoided by maintaining the junctions of the thermocouple arms and the measurement leads at a reference temperature. The measured signal is then proportional to the difference in temperature between the measuring and reference thermocouples.

4.2 Material System

Thermocouple selection for the development of the Glasgow SThM probes was inherited from initial investigations by A. Midha, J. Weaver, and H. Zhou [8] and consisted of a Au/Pd thermocouple with a thin NiCr intermediate layer for adhesion purposes. This decision was based on a number of practical requirements relating to fabrication and performance. It had been decided that initially the thermoelements be limited to those metals that were available for deposition in the Plassys MEB evaporator, namely Ni, NiCr, Ge, Ti, Au, Pd. The reason for this was that there was easy access to this evaporator in a clean environment which made for quick, reliable film deposition. In addition, the thickness of these metals could be controlled to ± 1 nm (important for lift off development). Further limitations were that the metals should be compatible with potassium hydroxide etching, and the lift off process used for definition of the thermocouple wires. The noble metals Au and Pd were chosen because they have a reasonable RSC ($12 \mu\text{V}/^\circ\text{C}$ at 300K [1]), are unreactive in potassium hydroxide, are thermoelectrically stable up to 1000°C in air [9] and do not readily form oxide coatings in air. The last requirement here is important for thin film thermocouples since the thermocouple interface is necessarily exposed to air between electrode deposition levels. Metals which would have produced a higher RSC like Ni and $\text{Ni}_{0.6}\text{Cr}_{0.4}$ (assuming similar properties to Nickel/Chromel thermocouples), were rejected because they both form surface oxide layers in air which could potentially degrade the electrical continuity of the thermocouple.

The thicknesses of the metals were chosen to provide a low resistance thermocouple so that the emf drop across the voltage measurement circuitry would be maximised. Lithographic considerations however dictate that the metal thickness be of the order of the minimum desired feature size, and one metal be thicker than the other to ensure continuity

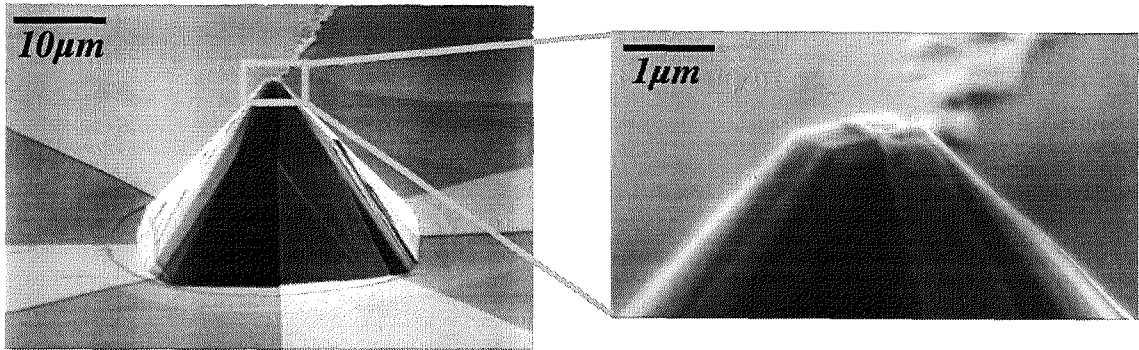


Figure 4-2 Test structure showing two separate wires intersecting at the apex a micromachined pyramid (courtesy of H. Zhou).

at the junction. Experiences of A. Midha had shown that both Au and Pd did not adhere satisfactorily to silicon nitride [8], and so a KOH compatible adhesion layer consisting of 5 nm $\text{Ni}_{0.6}\text{Cr}_{0.4}$ was required for each arm of the thermocouple. This layer was not expected to change the behaviour of the thermocouple since at such thicknesses the layer is not continuous, and resistive compared to the Au and Pd electrodes. Having satisfied the above criteria, test thermocouples using metal thicknesses of 20 nm Au and 45 nm Pd (excluding adhesion layers) were demonstrated by A. Midha and Dr H. Zhou, and so these values were retained for initial attempts at making thermocouples on probe tips.

4.3 Cross Thermocouples

The cross thermocouple probes were developed jointly with Dr Haiping Zhou. The principle was to have two dissimilar wires (Au and Pd) intersect over the apex of one of the generic probes. This automatically made sensor definition a two step process. Alignment between these two levels was important in so far as the sensor was to be positioned on the flat apex of the pyramid, but by its nature the cross thermocouple would yield a junction in every instance of misalignment.

Figure 4-2 shows an early pyramid test structure fabricated by Dr Zhou. These were constructed on substrates without the back processing normally found on the real device substrates. A cross thermocouple has been written at the pyramid apex, and the overlap of the wires that form the thermocouple junction can be clearly seen. The bottom wire is a bilayer of 5 nm $\text{Ni}_{0.6}\text{Cr}_{0.4}$ and 20 nm Au and the top wire is 5 nm $\text{Ni}_{0.6}\text{Cr}_{0.4}$ and 45 nm Pd. Probing for continuity using a dc probe station yielded a value for junction resistance of around 500 Ohms. Temperature dependence of the devices was then investigated by measuring their voltage response when pumped with an argon laser. The bulk materials

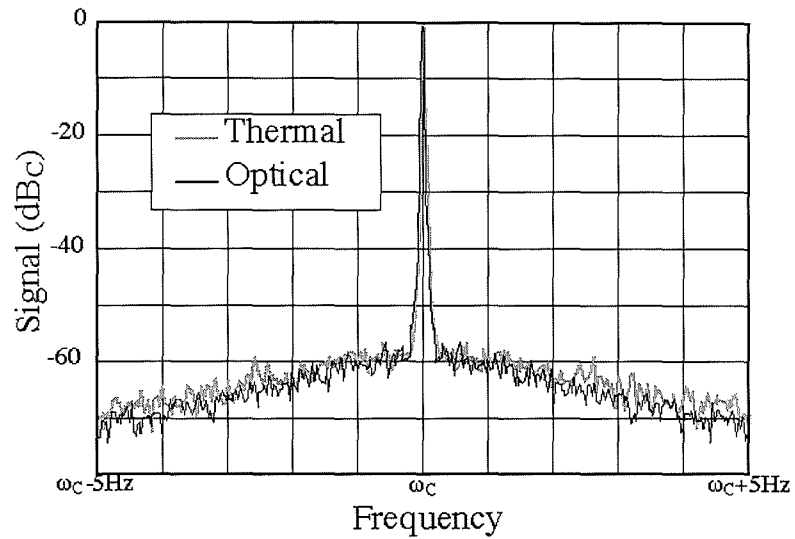


Figure 4-3 Spectral trace of a thermocouple on a pyramid apex when heated by a mechanically chopped laser (courtesy of J. Weaver).

predicted a junction Seebeck coefficient of $12 \mu\text{V}/^\circ\text{C}$. It was shown that the actual value for such thin film thermocouples is in fact similar to within a factor of two, (error arising from the uncertainty of the laser spot size). Examination of the close-in noise spectra of the laser and thermal response of the thermocouple (Figure 4-3) shows little difference demonstrating that the $1/f$ noise in the sensor is less than that of the laser [10].

Dr Zhou continued to make cross thermocouples on back etched substrates with silicon

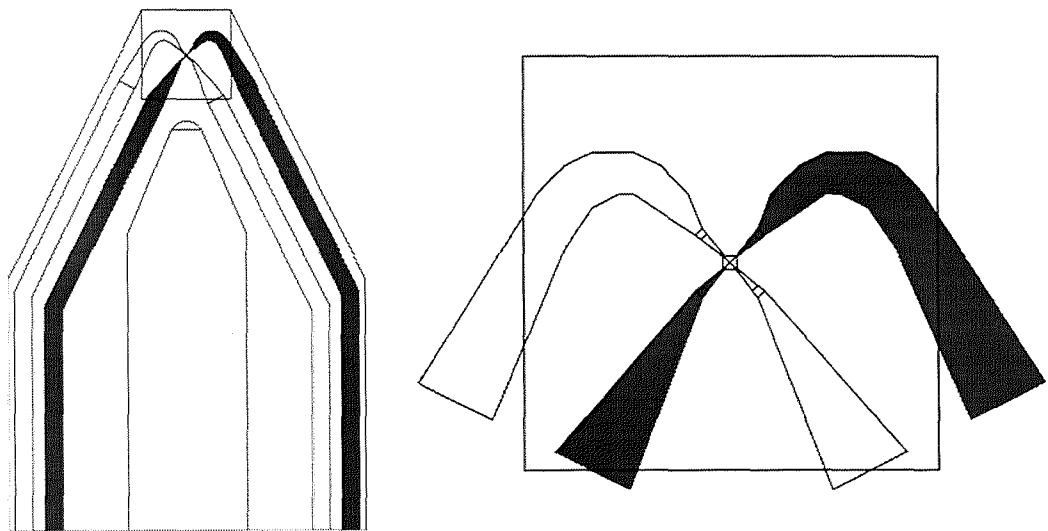


Figure 4-4 CAD pattern for device layers of the cross thermocouple probe.

nitride cantilevers. The CAD patterns for the sensor layers of the cross thermocouple probe are shown in Figure 4-4. An extra level was added after the sensor definition which included thick Au pads for bonding to the thermocouple wires, and a Au mirror on the cantilever to reflect the force sensing laser beams. The contact between the Pd wire and the Au pads forms a second thermocouple which has a junction area of several thousand square microns. The thermovoltage from the probe is proportional to the temperature difference between the thermocouple at the tip apex and this second “reference” thermocouple. By positioning this thermocouple on the probe base, its temperature may be approximated to that of the silicon substrate. This may assumed to be room temperature in most cases however care must be taken to account for situations where the temperature of the reference thermocouple may be changed (e.g. thermally radiative specimens).

After optimising the electron exposure, Dr Zhou fabricated a small number of operational thermocouple probes. Yields of order 10% per wafer were observed. Figure 4-5 shows a completed pre-release cross thermocouple probe. The minimum wire widths, and hence thermocouple junction sizes were 70 nm in this case. Tests after release showed the continuous thermocouples to have electrical resistances of approximately 1 k Ω . The probes were cleaved and attempts were made to use ultrasonic bonding to contact to the gold pads. Problems with contamination on the pad surface, which resulted in poor adhesion of the bonded wires, prompted attempts to use silver loaded epoxy to make the electrical connections. Unfortunately many probes became open circuit after the bonding process. It was suggested that this was due to electrostatic discharges (ESD) vaporising the thermocouple junctions. None of the cross thermocouple probes were scanned due to electrical failure on connection to the external measurement circuit.

A later demonstration by the author of the lithographic limit of patterning these wires over the flat topped micromachined pyramids is shown in Figure 4-6. A semi-processed

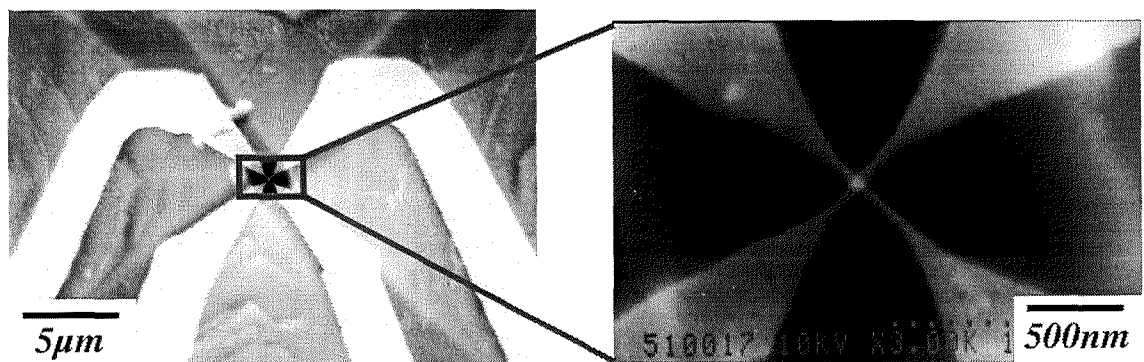


Figure 4-5 Plan view of Au/Pd thermocouple situated at the apex of a pre release micromachined tip (courtesy of H. Zhou).

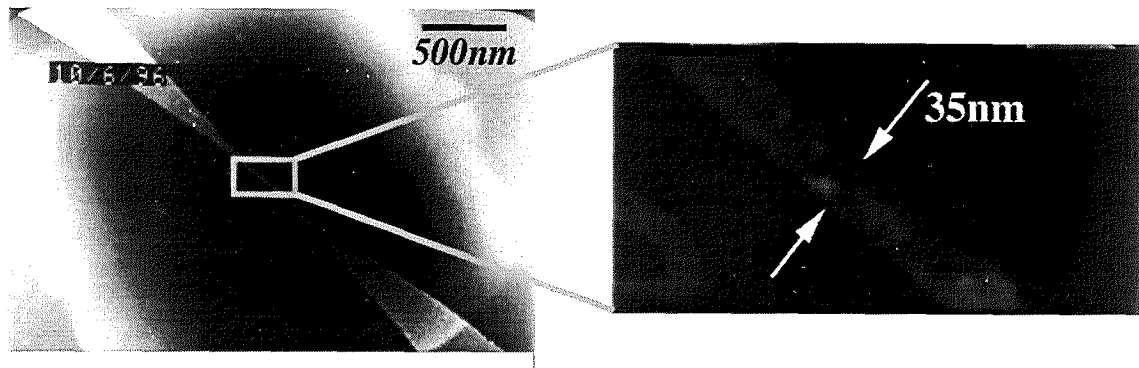


Figure 4-6 Approaching the resolution limit of a single wire on the apex of a micromachined pyramid.

thermocouple (consisting of only the Au thermocouple arm) was accidentally broken during processing, and this allowed some of the wires to be scribed and put in a Hitachi S900 (small specimen, high resolution electron microscope). The original wafer had been an exposure test and therefore a variety of thicknesses of wires were found. Typically the wires were 30-50 nm wide at their narrowest point. Wires with a width of 25 nm were also demonstrated on another wafer and appeared continuous when imaged using the lower resolution S800 SEM. A selection of the pre-release 25 nm thermocouples were probed using the dc probe station, but all became open circuit after conducting momentarily. One reason for this could be that too large a current was used (100 μ A compliance) and the device was breaking down due to electrical overstress. Alternatively ESD from the probe needles may have caused the failures, however care had been taken to short the two needles together before measurements were attempted. After the release etch, the rest of the 25 nm thermocouples appeared to be open circuit after examination by SEM. The wires appeared to have detached from the cantilever surface during the etch. This poor adhesion may have been caused by contamination under the wires.

A second generation design for the cross thermocouple probes involved larger pads to facilitate bonding with silver loaded epoxy. Figure 4-8 shows the arrangement of these pads on the substrate. The Au wire is joined at both ends by a single Au pad whereas the Pd wire has a Au pad at each end. This arrangement increases the area of Au for external connection purposes. The two pads attached to the Pd wires would have been made into a single pad were it possible.

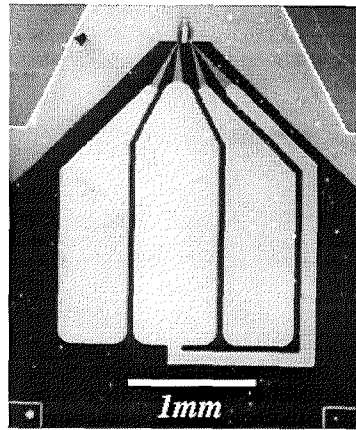


Figure 4-8 Pad arrangement for "cross" thermocouples. Note that two of the pads are shorted together. The blocks of six local alignment markers are clearly visible.

4.4 Triple Thermocouples

Several potential advantages are offered by incorporating more than one thermal sensor on an AFM probe. One possible application is the creation of a parallel thermal scanner which could scan multiple sensors simultaneously and thus increase throughput of the measurement system. For example, benefits in the form of increased data transfer rates to techniques like AFM storage [11] may be realisable. Investigations have been made using multiple lever instruments [12], but not yet with multiple sensors on a single cantilever. Another possible utility for multiple thermal sensor probes is the investigation of the parasitic tip contact changes which cause artefacts in thermal AFM imaging. By measuring the temperature at several different sites on the probe tip, it may be possible to determine

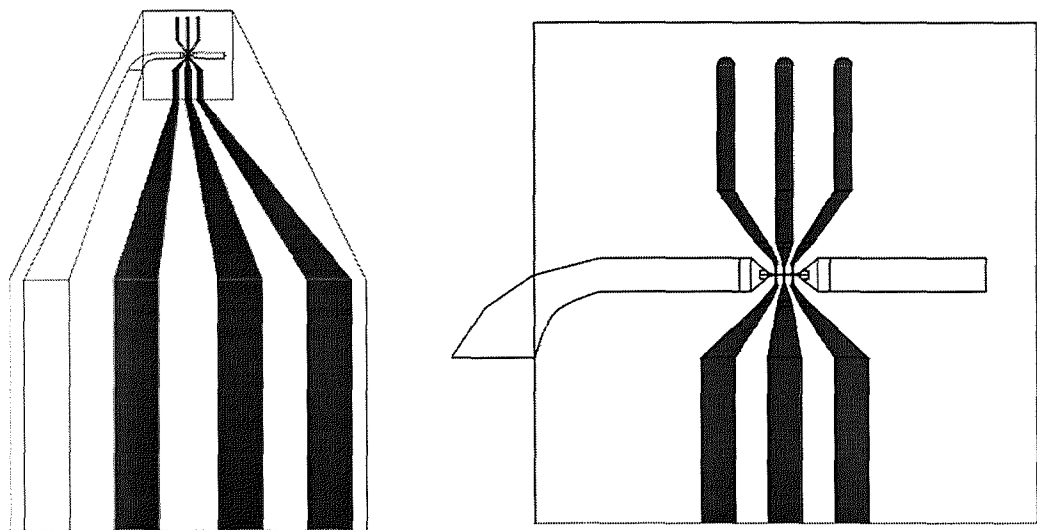


Figure 4-7 CAD patterns for the device layer of the triple thermocouple probe (Blue=Pd, Yellow=Au).

what part of the tip in contact and the quality of the contact. The ability to subsequently correct a thermal image by compensating for tip contact variations would be extremely valuable, especially with highly topographic specimens. A final benefit of making multiple sensors is that the yield of operable probes increases. Multiple sensors means that there are multiple chances of making at least one good sensor per probe. Conversely of course this means that the chance of all sensors succeeding on a single probe decreases as sensors are added, and so multiple sensor probes are expected to have relatively low yield.

In order to demonstrate the practicality of multiple sensor probes, it was decided to make triple thermocouple probes. It has been shown that a single thermocouple can be made using a variety of methods [13-16], and although twin thermocouple probes have not yet been fabricated it was thought that triple thermocouples would more readily show an ability to extend to “n” thermocouple probes. For example, twin near field optical sensors have been demonstrated [17], however the technique does not readily extend to more complex arrangements because the apertures are only loosely controlled through timed etched and not patterned lithographically.

The layout of the three thermocouples consisted of a common gold arm and three bisecting Pd arms (Figure 4-7). Ideally each thermocouple would be completely separate from the others (in order to reduce electrical crosstalk and increase thermal resistance among the sensors), but it was felt that packing six leads and six pads onto a single probe

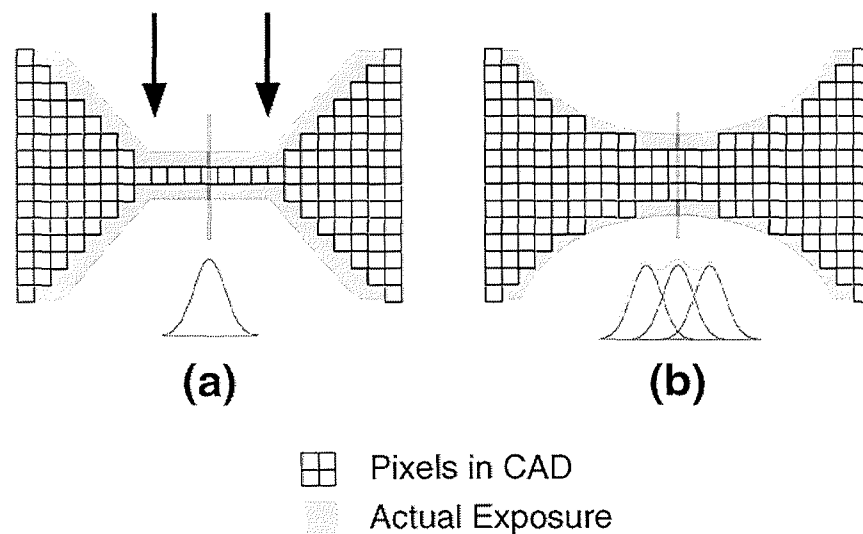


Figure 4-9 (a) By defining a single pixel wire and using the exposure to control the shape it was found that the arrowed regions were susceptible to open circuit. (b) By using multiple pixels to form the constriction, and smoothing the edges, increases in successful wires were observed, but at the expense of flexibility and minimum wire width.

was impractical for a first attempt. New problems were already anticipated with writing a long narrow constriction in the Au wire, and multiple high resolution wires in the Pd layer. Some novel design changes were implemented to combat these potential problems. During the fabrication of the cross thermocouples, it was discovered that the rounding of sharp edges aided lift off considerably. Applying this to the high resolution features, the tapers in the wires (where the thermocouples are formed) were smoothed. The result was an increase in well lifted off features, and a decrease in destructive open circuits at the tapered region. A second design change saw a move away from defining the high resolution features using dose variation. Originally the taper in each of the cross thermocouple wires had been made by drawing a single pixel (5 nm) wire in the CAD package (see Figure 4-9(a)), and varying the dose of electron exposure to define the width of the wire. This was felt to be sub-optimal however since the resulting exposure profile of the wire resembles that of a single Gaussian giving poor edge definition. Wide wires had also been observed to leave adjoining features over-exposed. By defining the wire in CAD to be approximately the desired width (about 30% less to account for some feature growth) and then exposing at a lower dose, a “plateau” exposure profile is created (Figure 4-9(b)). One advantage of this is that feature edges are better defined, however it also means that feature width must be more or less predetermined in the software and so some flexibility is lost.

Another development to aid the lift off, of the Pd layer in particular, was the lengthening of the metal wires so that each bisects the whole pyramid. This is a ploy to facilitate the tearing nature of lift off (see Section 2.5). Small, isolated portions of material are most

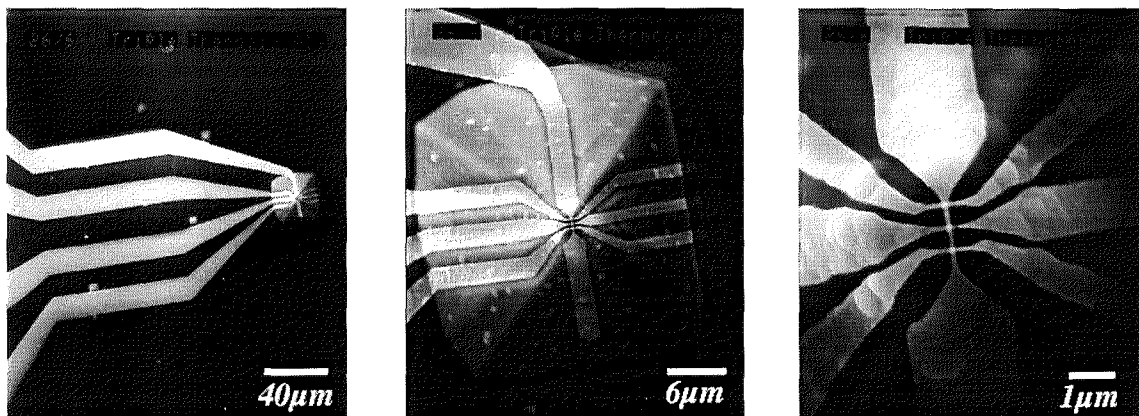


Figure 4-10 First pre-release triple thermocouple probe. Note how the wires continue over the pyramid past the junction to aid lift-off. Close up of the triple thermocouple junctions. Note that the middle wire appears discontinuous, however this discontinuity occurs on the other side of the gold wire from the pads and so does not affect the operation of the probe.

likely to fail during lift off, however lengthening the wires over the pyramid improves the chances of the bulk of the surplus material pulling away the small areas at the tip apex. An analogy for this would be peeling adhesive tape (shaped like the thermocouple wires) from a surface. Tears, which could propagate and cause the tape not to peel off in one piece, are most likely to originate at sharp corners. By smoothing these corners, tearing can be reduced and successful removal of the tape (lift off) increased.

The triple thermocouples were fabricated after exposure tests were conducted to find the optimum dose for the definition of the high resolution features ($\approx 3500 \text{ C/cm}^2$). Lifting off the long Au wire proved to be non-trivial, since discontinuities were often apparent along the narrowest part of the wire. Changing the wire in CAD from single to multiple pixels, as described earlier, improved continuity significantly while allowing neighbouring features to be well exposed. This increased the yield of good Au wires from around 10% to 80% with wire widths of approximately 100 nm. Early attempts at fabricating the three Pd wires also tended to fail but in this case because surplus material was remaining at the tip apex which short circuited the wires together. Rounding of sharp features improved the quality of the lift off for the reasons described earlier, and again produced yields of around 80%. A finished probe is shown in Figure 4-10. From four quarter wafers, typically 50% of completed probes had all three thermocouples electrically continuous. The rest had single ($\approx 20\%$) or double ($\approx 20\%$) thermocouples, leaving only a small proportion ($\approx 10\%$) having failed completely. Resistances of the thermocouples were in general matched to within 50Ω . The calculated difference in resistance due to a thermocouple being situated at one or other end of the long Au wire is 30Ω , and in general the resistances corresponded to thermocouple position. This was not always true however due to the other factors affecting the resistance such as imperfections in wire shape, and contamination at the junction.

Beyond electrical continuity testing, the thermal dependency of the thermocouples was demonstrated by mounting the thermal probes in the Glasgow AFM (see Chapter 3) and manually bringing a commercial Peltier cell²³ into close proximity (see Figure 4-11). A Peltier cell is a thermopile sandwiched between two plates made from an electrically resistive, but thermally conductive material. The geometry is optimised such that when a current is passed one side of the device experiences Peltier cooling, and the other Peltier heating. For this particular cell, a current of 1.2 A at a voltage of 0.48 V produces a heat rise on the hot side of $+67 \text{ }^\circ\text{C}$. The middle thermocouple of a fully operational triple thermocouple was connected to the pre-amplifier circuitry the using the clamp method (see Section 3.3). The other two thermocouples were left open circuit. The thermocouple

²³ RS Electronics Peltier Mini Module

resistance was $800\ \Omega$. The Peltier cell was positioned using micrometer screws such that it was close ($\approx 30\ \mu\text{m}$), but not touching, the triple thermocouple probe. The bottom of the cell was aligned to the probe tip so that minimum heat from the cell impinged on the second “reference” thermocouple at the Au-pad/Pd junction. The graph shown in Figure 4-11 shows the variation in thermocouple voltage with increasing Peltier current (increasing temperature). A maximum Peltier current of $0.5\ \text{A}$ gave a thermocouple voltage of $6.5\ \text{mV}$. The noise level after $\times 100$ amplification was $0.25\ \text{mV}$. Assuming the thermocouple has bulk thermoelectric properties ($12\ \mu\text{V}/^\circ\text{C}$) this corresponds to a temperature difference between the “reference” and measuring thermocouples of approximately $5.5\ ^\circ\text{C}$. This figure is reasonable since the hot side of the Peltier plate may be assumed to rise by around $15\ ^\circ\text{C}$ at $0.5\ \text{A}$. In addition to this, the probe tip was not well thermalised to the plate since it was not in contact, and the signal would have been further diminished by additional heating of the “reference” thermocouple by the Peltier plate.

Another test was made to determine the matching of the three thermocouples. The probe was optically pumped by focusing a laser (Ar^+ , $5\ \text{mW}$, $514\ \text{nm}$) on the thermocouples. The laser was focused onto the mirror situated on the cantilever, thus heating the

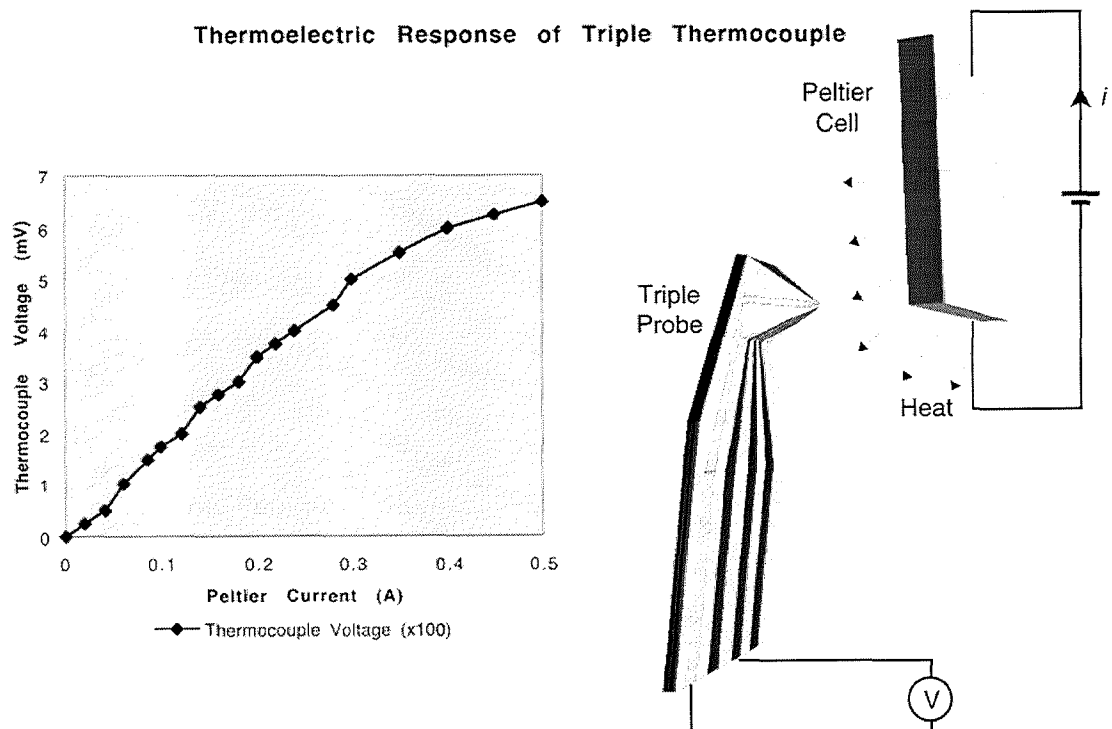


Figure 4-11 Graph showing the temperature dependence of one of the thermocouples on a completed triple thermocouple probe.

thermocouples uniformly. The laser was modulated at 400 Hz and detected using a lock in amplifier. The voltage response was recorded for each of the three thermocouples yielding values of 198 μV , 198 μV and 202 μV ($\pm 1 \mu\text{V}$). This corresponds to a matching of no worse than 3%. It is interesting to note that although the resistances of the thermocouples varied on average by about 6%, due to pattern imperfections, junction sizes and quality of contact at the junctions, the Seebeck coefficient varied by significantly less. This is consistent with the behaviour of bulk thermocouples. The 3% mismatch may arise from factors such as non-uniform heating due to roughness, asymmetry of the wires on the cantilever, local purity variations in the electrode metals, or mechanical stress.

Further experiments involving the triple thermocouple probes were attempted, including scanning a semiconductor laser diode facet. Unfortunately out of contact scans were dominated by heating from the laser light and not the facet itself. When contacted to the specimen surface, problems with crashing the probe over the edge of the facet and contamination of the tip with conducting adhesive from the specimen were experienced. No meaningful data was obtained, however it was encouraging that probe failure was observed to be due to gross mechanical impacts rather than sensor wear or electrostatic discharge.

- [1] Thermocouples Theory and Properties: CRC Press Inc, 1991.
- [2] W. F. Roeser, "Thermoelectric thermometry," *Journal of Applied Physics*, vol. 11, pp. 388-407, 1940.
- [3] Thermoelectricity: an introduction to the principles. New York: John Wiley and Sons, Inc., 1962.
- [4] W. Thomson, "Communication on a mechanical theory of thermo-electric currents," *Proc. Roy. Soc. Edin.*, 1851.
- [5] W. Thomson, "Account of Researches in Thermo-electricity," *Proc. Roy. Soc. Lon.*, vol. VII, 1854.
- [6] R. P. Reed, "Thermoelectric thermometry: a functional model," in *Temperature, its measurement and control in science and industry*. New York: American Institute of Physics, 1982, pp. 915-922.
- [7] R. P. Reed, "Ya Cant Calibrate a Thermocouple Junction .1. Why Not," *Measurements & Control*, pp. 137-145, 1996.
- [8] A. Midha, "Batch-fabrication of novel nanoprobe for SPM," in *Electronics & Electrical Engineering*. Glasgow: University of Glasgow, submission due 1999.
- [9] Y. G. Kim, K. S. Gam, and C. Rhee, "1000 H Stability Test Of the Au/Pd Thermocouple At 1000-Degrees-C," *Metrologia*, vol. 33, pp. 337-339, 1996.

- [10] H. Zhou, A. Midha, G. Mills, S. Thoms, S. K. Murad, and J. M. R. Weaver, "Generic scanned-probe microscope sensors by combined micromachining and electron-beam lithography," *Journal Of Vacuum Science & Technology B*, vol. 16, pp. 54-58, 1998.
- [11] B. W. Chui, T. D. Stowe, T. W. Kenny, H. J. Mamin, B. D. Terris, and D. Rugar, "Low-stiffness silicon cantilevers for thermal writing and piezoresistive readback with the atomic force microscope," *Applied Physics Letters*, vol. 69, pp. 2767-2769, 1996.
- [12] S. C. Minne, S. R. Manalis, and C. F. Quate, "Parallel atomic force microscopy using cantilevers with integrated piezoresistive sensors and integrated piezoelectric actuators," *Applied Physics Letters*, vol. 67, pp. 3918-3920, 1995.
- [13] Y. Suzuki, "Novel microcantilever for scanning thermal imaging microscopy," *Japanese Journal Of Applied Physics Part 2-Letters*, vol. 35, pp. L 352-L 354, 1996.
- [14] M. Stopka, E. Oesterschulze, J. Schulte, and R. Kassing, "Photothermal scanning near-field microscopy," *Materials Science and Engineering B-Solid State Materials For Advanced Technology*, vol. 24, pp. 226-228, 1994.
- [15] J. Lai, M. Chandrachood, A. Majumdar, and J. P. Carrejo, "Thermal detection of device failure by atomic-force microscopy," *Ieee Electron Device Letters*, vol. 16, pp. 312-315, 1995.
- [16] K. Luo, Z. Shi, J. Varesi, and A. Majumdar, "Sensor nanofabrication, performance, and conduction mechanisms in scanning thermal microscopy," *Journal Of Vacuum Science & Technology B*, vol. 15, pp. 349-360, 1997.
- [17] E. Oesterschulze, O. Rudow, C. Mihalcea, W. Scholz, and S. Werner, "Cantilever probes for SNOM applications with single and double aperture tips," *Ultramicroscopy*, vol. 71, pp. 85-92, 1998.

5 Improved Access Thermocouples

5.1 Motivation

A great deal of research during this project was involved with developing a thermal probe that offered better specimen access than the generic pyramid probes with flat apices. The blunt pyramidal tips are suitable for relatively flat specimens, but for highly topographic specimens the ability of the probe to faithfully trace the surface is compromised. Poor specimen access is a common cause of artefacts in conventional AFM [1] and has also been shown to cause spurious features in thermal imaging [2]. In general artefacts may be reduced with any given specimen by reducing the (microscopic) tip radius and the (macroscopic) opening angle of the probe.

The measurement of specimens from the semiconductor industry was of particular interest due to the Motorola sponsorship of the project. Passivated integrated circuits typically have densely packed protrusions several microns high, and so tip access is of great importance if SPM analysis is desired. Specimen preparation techniques which remove passivation by chemical means or planarise the specimen by mechanical polishing are common, however they can cause degradation of the original thermal properties of the specimen. To avoid this, methods for making a probe with good access were devised which involved reducing both the opening angle and tip radius of the probe (defined on the generic probe by the pyramid shape and the flat apex respectively).

5.2 Fabrication Development

An early idea to make an improved access probe relied on making the ends of two sharp wires overlap on the side of one of our generic pyramids. If the material supporting the wires could somehow be selectively removed by further processing, the free metal thermocouple would form a lithographically defined asperity which could then be scanned. The opening angle would also be improved if the angle between the two wires was less than the opening angle of the pyramid. In order to test feasibility of aligning and transferring EBL patterns where the critical features were situated on a sloped surface, preliminary tests were carried out. Custom made substrates with etched pyramid tips, but without the back etched membranes, were fabricated. Topographic EBL markers similar to those used with the generic substrate were positioned a known distance away from the pyramids. Using this scheme, two separate lithographic levels were written to form wires with coincident sharp tips (Figure 5-1).

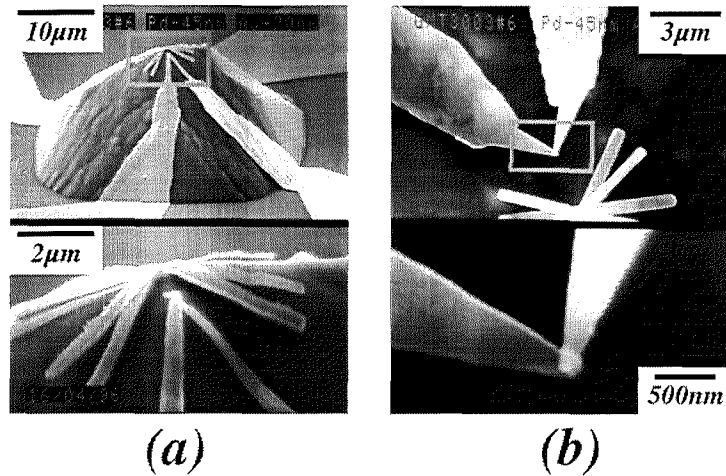


Figure 5-1 Side thermocouple test specimens.

Several problems were encountered during the testing. Firstly, lift-off of the wire tips proved to be extremely difficult and often resulted in catastrophic failure. The most common failure mode was a metal “cap” remaining over the pyramid apex. This had also been observed with the conventional flat apex thermocouples, but had been improved by applying several short bursts of ultrasonic agitation. Unfortunately ultrasonic lift off did not significantly improve matters when applied to these test structures. It appeared that although the resist under the metal was dissolving (which should have freed the metal to float off into the acetone), the metal was failing to release and sticking back down to the pyramid (Figure 5-2). Once settled back on the substrate, the metal held firm against attempts to dislodge it (presumably due to capillary forces). In order to free the metal caps, the patterns were rewritten, but this time a lift-off aid in the form of a cross was patterned

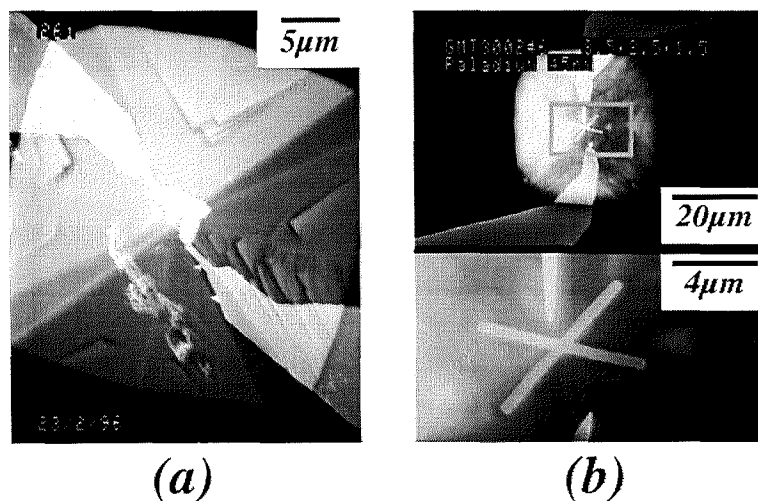


Figure 5-2 Sharp wire test structures patterned on the side of pyramids. Left: Failed lift off due to capping. Right: Successful lift off with a cross shaped lift off aid at the apex of the pyramid.

at the top of the pyramid (see Section 2.5). The cross was separate from the thermocouple wires, but introduced extra lines along which the metal could tear. In conjunction with ultrasonic agitation, this almost completely solved the lift off problem. The size and shape of the lift off aid was varied to maximise both removal of the metal cap, and the lift off quality round the tip. Figure 5-2 shows a typical cross structure and the resulting improvement in lift off.

A second problem arose in writing EBL defined wires with sharp points. Initial wires had tip radii of 150 nm and greater, depending on taper angle, which was far greater than intended. The wires were defined in software to terminate in a single 5 nm pixel, and were written with a 12 nm spot size. Practical EBL using the Leica machine can in general produce minimum feature sizes of 25 nm, and on sloped surfaces with imperfect focus conditions features somewhere in the region 50 nm were expected. Varying the electron exposure and development did not improve the tip sharpness. Features either appeared over exposed (over developed) and rounded, or under exposed (under developed) and rounded. There appeared to be very precise conditions at which ideal exposure and development would cause sharp tips. Instead of further efforts to identify the exact exposure conditions, it was decided to try and desensitise the pattern to exposure dose. This was achieved by distorting the shape of the tip in software so that development would give the desired shape. A single pixel protrusion from the tip was added to the written pattern. The length of this additional feature was varied and it was discovered that using a length of 75-125 nm (dependent on taper angle) yielded sub 50 nm diameter tip sharpness under normal exposure and development conditions. This may be thought of as an exposure compensation technique, similar to proximity correction [3], but for isolated features instead of densely packed features.

A final problem was encountered in the alignment of features. There were four main components to the alignment:

- Aligning the marker to the pyramidal tip.
- Aligning the critical features to the pyramidal tip.
- Aligning the different matrices (in the same lithographic level) to each other.
- Aligning different levels accurately to each other.

The first two are related because alignment of a feature to the tip depends critically on how well the position of the marker is known with respect to the pyramid. Local markers and pyramids are written on a three inch wafer in the same EBL level. The job takes several hours to write and in that time, despite periodic corrections, stage drift can result in misalignments of several hundred nanometres. To avoid these drift errors a scheme was

devised by A. Midha which involved quickly writing one matrix containing the outlines of the markers and pyramids, then a second longer matrix which filled in the remaining areas. By this method the edges of the features were well placed, and any drift errors when writing the bulk of the pattern were made redundant.

Aligning different matrices to each other was necessary because different spot sizes and focus conditions were needed to write large areas in a sensible time. Exactly where the marker was found however seemed to depend on the spot size, electron energy and focus conditions of the EBL machine and this could in turn cause gaps in the exposed pattern. Creating an overlapping area common to two adjoining matrices was common practice for planar lithography in order to compensate for small drift errors (≈ 50 nm). In this case however, random errors in the range 250-500 nm were observed with the three dimensional substrates, especially with the lower resolution matrices. By increasing the size of the overlapping areas it was possible to maintain the continuity of individual features, but at the expense of good definition. The reason for these particular misalignment errors remains unclear. The last and most critical aspect to the alignment of the coincident thermocouple wires was aligning the two lithographic levels which defined the thermocouple arms to each other. Care was taken to use the same alignment marker, spot size, focus conditions and electron energy for each level since errors here would determine the size and shape of the thermocouple junction. Despite these measures errors of several hundred nanometres were observed. Some well aligned thermocouples were fabricated, however these were attributed to the random nature of the errors rather than genuine cases of good alignment. More often, the misalignments would cause the wires miss each other altogether creating an open circuit, or cross over further down the length of the wires creating double tips. Figure 5-3 shows the different tip profiles caused by

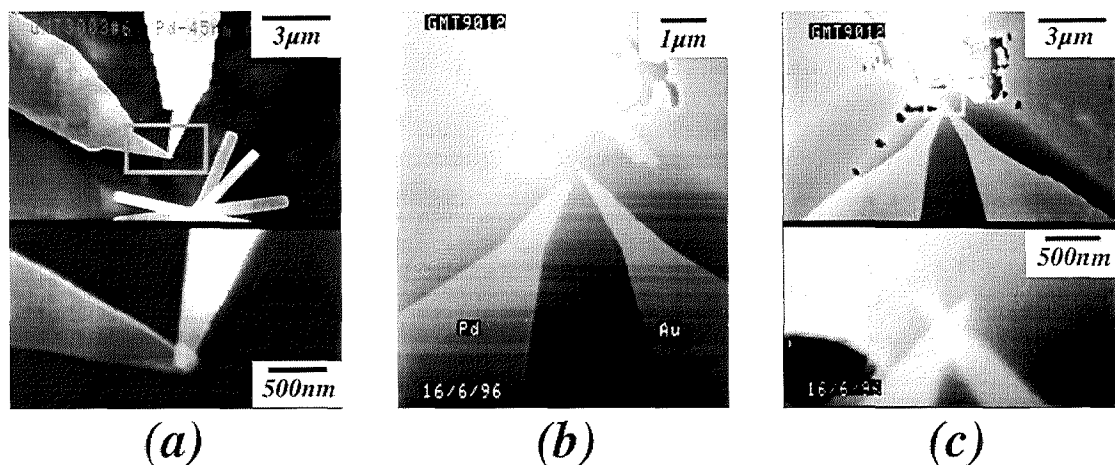


Figure 5-3 (a) Two wires well aligned to each other. (b) Misalignment causing an open circuit. (c) Misalignment causing a double tip.

misalignment of the two thermocouple layers. Without intimate knowledge of the procedure used by the electron beam-writer to determine the position of the markers, it proved difficult to determine the cause of the alignment errors. By trial and improvement however it was possible to limit the misalignments by implementing the following measures:

- Use 100 kV not 50 kV electron beam since observed misalignments were greater between matrices with 50 kV. The greater depth of focus provided by 100 kV resulted in less feature growth when out of focus.
- Use local alignment markers instead of global markers (reduces any errors which are a fraction of the distance from marker to pyramid).
- Disable the automatic drift calibration (an error in the software causes the machine to align to a site then compensate for drift which has already been eliminated).
- When fractionating patterns, human error in positioning matrices can result in misleading failures. Automatic centring of patterns is possible using the CATS software and is recommended.
- Use the same marker for critical alignment levels.
- Use the “cross method” which involves using a cross structure remote from the real marker for coarse operator alignment. Without this, the first marker set is heavily exposed and may be degraded for the subsequent levels.

The process of aligning the ends of two metal wires to each other was transferred to the generic substrates. Figure 5-4 shows a pre-release probe with a completed thermocouple. Despite the improvement in alignment provided by the improved operating procedure, errors of 250 nm were still occurring on a regular basis. Because of this, and the perceived difficulty of subsequently removing the underlying silicon nitride to free the thermocouple, a new probe design that used a degree of self alignment was developed.

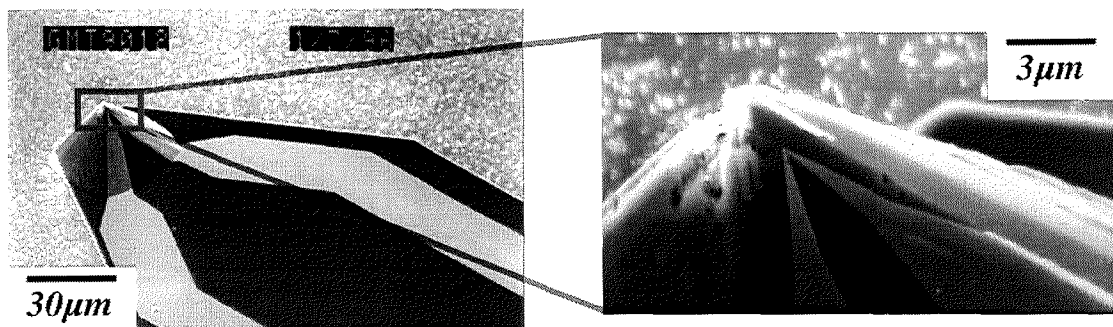


Figure 5-4 Two sharp tipped coincident wires on a generic substrate.

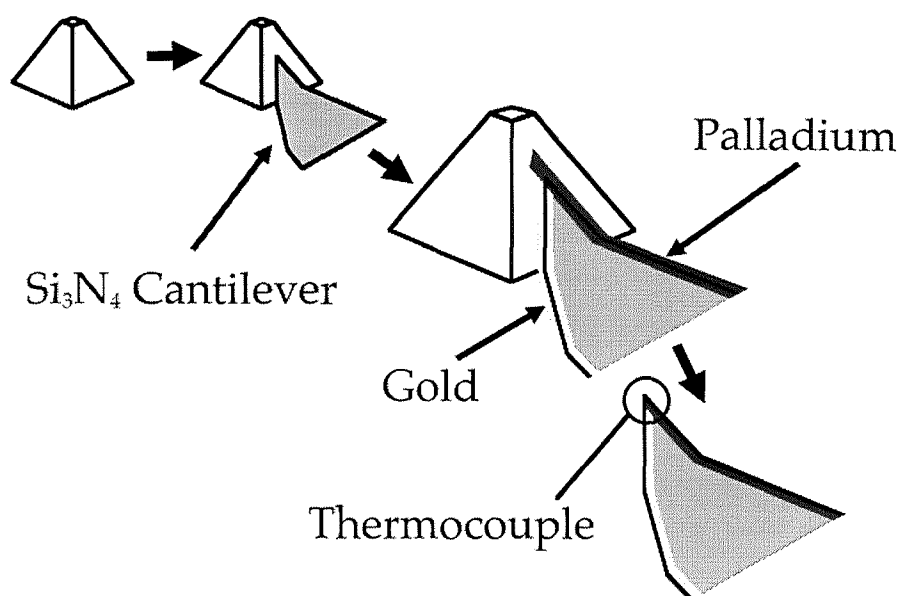


Figure 5-5 Schematic of the side self aligned thermocouple structure.

5.3 “Side” Thermocouple Probes

The principle feature of the new design, called the improved access thermocouple probe (or “side” thermocouple), was a change in the shape of the silicon nitride cantilever. Figure 5-5 shows a graphic representation of the new design. Instead of a cantilever that encompasses the pyramid, the silicon nitride is shaped into a sharp triangular tip positioned on the side of the generic silicon pyramid. Subsequent thermocouple wire levels are written such that they coincided at the sharp end of the triangular cantilever to form a junction, but also overlap the cantilever onto the sacrificial silicon membrane. Removal of the silicon membrane in the final level causes the removal any part of the thermocouple wires not on the triangular cantilever. This can be thought of as self alignment in one dimension. Figure 5-6 shows SEM micrographs of the new cantilever shape, and the deposition of the metal wires to form the thermocouple. Identical wire thicknesses (5 nm NiCr/20 nm Au and 5 nm NiCr/45 nm Pd) to those used for the flat apex devices were deposited for the “side” thermocouple. Normally the cantilever was transferred into a Cr RIE mask by wet chemical etching. This scheme however was not compatible with the definition of sharp features because wet etches are isotropic and so etch laterally as well as vertically, causing sharp corners to be degraded. This was known to be the case with the conventional cantilevers, but of little consequence because the edges of the cantilever were not critical features. With the triangular “side” cantilever however the definition of the cantilever determines the tip profile and width of the thermocouple

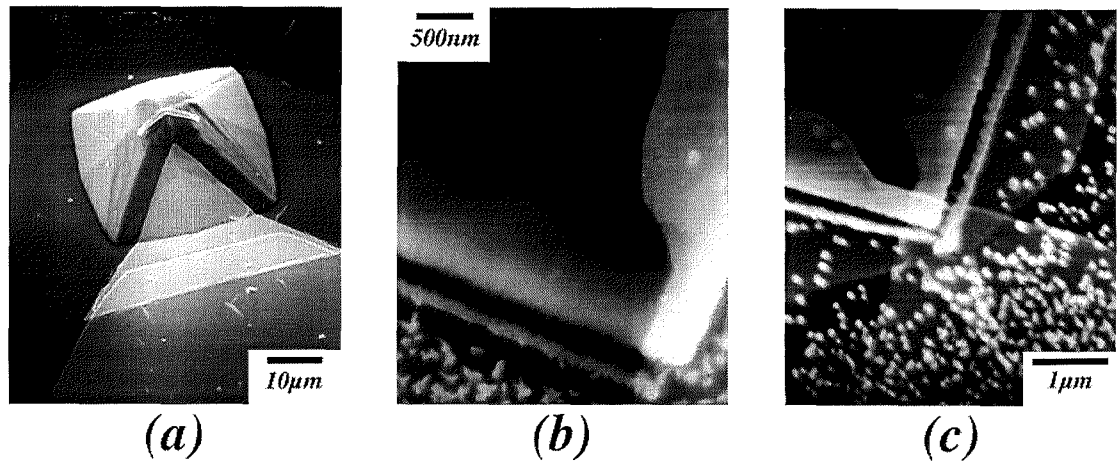


Figure 5-6 "Side" thermocouple probe. (a) Dry etch mask for the cantilever. (b) Au thermocouple wire overlapping the dry etched cantilever. (c) Au and Pd wires forming the thermocouple junction.

wires. It was necessary therefore to use a two step process to pattern the triangular cantilever. An initial lithographic level and wet etch of the original sputtered Cr layer broadly defined the cantilever shape up to the base of the pyramid. A second overlapping, high resolution, EBL level was lifted off in 100 nm of $\text{Ni}_{0.6}\text{Cr}_{0.4}$ to define the critical triangular end of the cantilever. Using the exposure compensation strategy outlined in section 5.2, well defined tip profiles were achieved in the RIE mask material. The mask did degrade slightly during RIE etching due to imperfect selectivity between NiCr and silicon nitride, which resulted in tip radii increasing from below 50 nm to around 100 nm.

Although the problems of producing a free space thin film thermocouple and misalignment causing double tips had been addressed by the "side" design, the problem of misalignment between EBL levels distorting the shape of the thermocouple junction was still evident. In addition to this, the nature of the physical contact between thermocouple and specimen had been changed. With thermocouples fabricated on the flat apex pyramidal tips, the whole of the surface area of the thermocouple is expected to touch the specimen (assuming a flat specimen). For the "side" thermocouple probe, only a small proportion of the thermocouple will touch the specimen due to the angle of incidence of the tip. A disadvantage of smaller contact area however is that only a small portion of the thermocouple is expected to be well thermalised to the specimen, compared to the flat apex thermocouple probes. This means that the improved access thermocouple tip may not be superior to the flat apex tips in every instance, since attenuation of thermal contrast may be observed due to non-uniform temperature at the thermocouple junction.

Thermocouple junction sizes of 250 nm^2 were fabricated on the improved access thermocouple probes. These dimensions were very much larger than those achieved with the flat apex thermocouples due to the restraints of beam-writer misalignment. In general the spread of junction sizes was $150\text{-}350 \text{ nm}^2$, although sometimes the variation was large enough to cause the thermocouple wires to miss the cantilever altogether. These random alignment failures were, by their nature, difficult to reproduce and their origin remains a mystery. One possibility is that lateral shifts are experienced because the writing beam is imperfectly aligned down the electron column. Testing continues to discover the cause of these problems.

Using a dc probe station (Omniprobe model 646) and a Hewlett Packard semiconductor parameter analyser (model 4145A), the thermocouples were tested for electrical continuity before release. They were found to have resistances in the range 800 to $1000 \ \Omega$. The variation in resistance values was attributed to the variation of junction size and quality. Around 80% of the devices appeared continuous in the SEM, but after probing only 50% were found to be electrically continuous. The cantilevers were released and Figure 5-7 shows a micrograph of a typical released probe. The probes had remained sharp after the final etch (KOH etches silicon nitride slowly $\approx 0.5 \text{ nm/min}$) with a typical tip radius of 100 nm . After release 90% of cantilevers were intact, with the failures being due to physical damage to the substrate (hairline cracks in the membrane). Probing showed that only 5 out of 30 devices were still electrically continuous. Resistance values however were the same as those taken pre-release, to within $50 \ \Omega$. The reason for the failure of the thermocouples before and after release was attributed to contamination between the thermocouple layers causing an insulating layer or loss of adhesion during the release. For subsequent "side" thermocouples, two measures were implemented that improved the

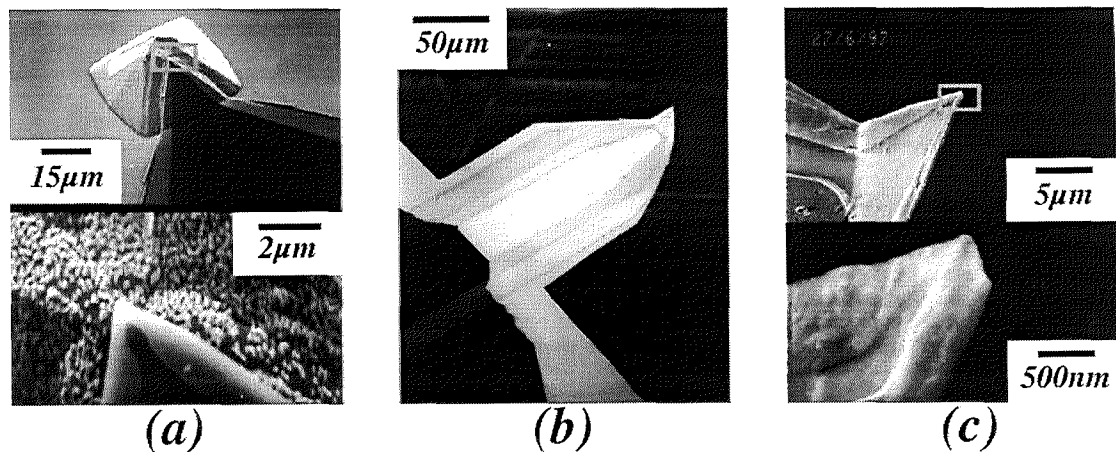


Figure 5-7 Left: Pre-release "side" probe. Middle: Released "side" thermocouple probe. Right: Close up of released "side" thermocouple tip.

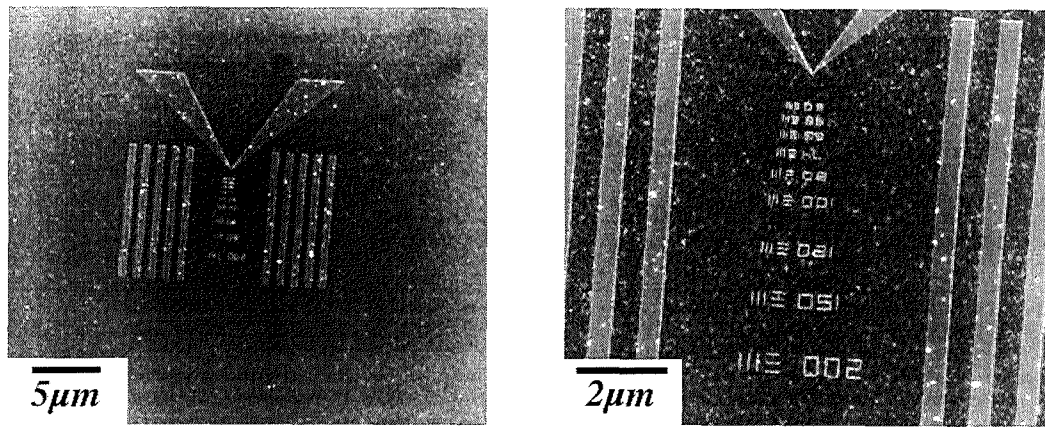


Figure 5-8 Patterns used for the photothermal test specimen.

yield. Firstly, developed patterns were subjected to 1 min oxygen plasma etch in a barrel asher before metal deposition (to remove any debris in the cleared channels), and secondly the amount of time that critical areas were exposed to air was reduced (as soon as one layer was completed the substrate was spun with resist for the next layer). This increased the yield of continuous thermocouples to at least 70%, and reduced the failure of junctions during release to approximately 10% thus confirming that contamination was responsible for the early failures.

5.4 Photothermal Experiment

The experimental set-up described in Chapter 4 was used for initial scanning tests with the “side” thermocouples probes.

A thermal test specimen was designed and fabricated by Dr J. Weaver consisting of large features for gross alignment and a series of gratings varying in size from 200 nm down to 50 nm (mark+space). Figure 5-8 shows SEM images of a similar specimen. The features were written onto a glass microscope slide using high resolution EBL and lifted off in 20 nm of Au. The whole specimen was then evaporation coated with 30 nm of Al. The specimen was mounted in the microscope and illuminated from the rear using a laser (Ar+, 514 nm, 10 mW). Figure 5-9 shows a schematic of the experiment and a view from the microscope CCD camera. The principle of the experiment was that Au absorbs approximately 2.5 times more light at 514 nm than Al [4], and would therefore cause a temperature gradient to be maintained between the two metals with the Au the hotter of the two. The laser was modulated at 1.025 kHz and a lock-in amplifier used to demodulate the signal from the thermocouple. Experience had shown that the cantilevers were sufficiently flexible not to physically damage the sensor when scanned over a surface. This was found to be the case even without the employment of force feedback. A first attempt to scan the

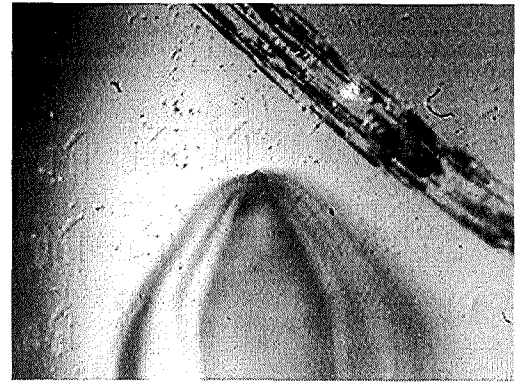
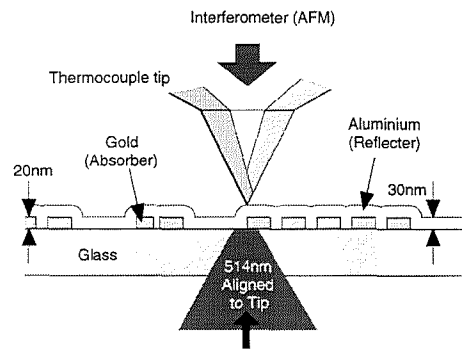


Figure 5-9 Left: Schematic of photothermal experiment. Right: View from microscope CCD camera of "side" probe in contact with the photothermal specimen.

"side" probes was made with the force feedback system disabled. A coarse manual approach was made, with the final contact controlled using the z-piezo.

Initial scans measuring the thermocouple voltage produced the two images shown in Figure 5-10. The magnified image is of the 200 nm (mark + space) grating. There appeared to be two kinds of contrast in the lower magnification image, temperature contrast and topographic contrast. The temperature contrast was the stronger contrast and seemed smeared due to thermal spreading by conduction through the reflecting aluminium and glass substrate. The contrast seemed correct however (higher temperatures around the gold features) and corresponded to 60 mK assuming bulk Seebeck coefficient for the thermocouple. The topographic contrast is offset from the large scale temperature contrast because the laser was not perfectly aligned to the thermocouple. Although the specimen

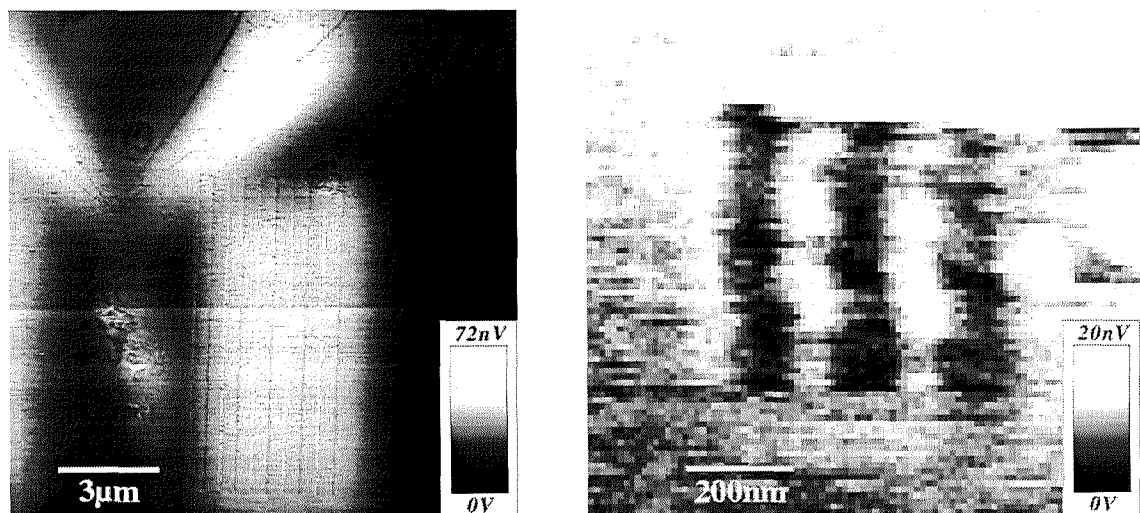


Figure 5-10 Left: Initial plot of thermocouple voltage vs position for photothermal specimen (scan time several hours). Right: Zoom of the 200 nm grating (contrast caused by tip contact changes).

succeeded in its primary role (to provide a specimen with thermal gradients), it did not provide high resolution temperature features. This was presumably due to the spreading of the heat into the surrounding metal. High resolution thermal detection of topography was observed due to differences in contact between tip and specimen, shown by the sharp edge enhancement effects seen in both the low and high magnification images. As the tip encountered hills and valleys the thermal conductivity between tip and specimen varied due to differences in the surface area of the sensor touching the specimen. Such artefacts obscured any true temperature information originating from the high resolution gratings. This can be seen in the high magnification image in which contrast is dominated by the topography of the specimen. The contrast is reversed from that which would be expected if the contrast were due to the specimen temperature (the Au features appear to be at a lower temperature). This is consistent with the theory that the tip is losing contact as it traverses the metal ridges caused by the grating. The smallest period grating resolved was 80 nm (mark+space) which indicated a 40 nm resolution. The risetime of the edges in the high magnified image were measured to be approximately 40 nm which agrees with the minimum resolvable grating figure. Although the high resolution contrast here was due to tip contact effects, the result shows that the probe is capable of thermally detecting 40 nm features should we find a specimen that requires such resolution.

With force feedback enabled, the simultaneous thermal and topographic images of Figure 5-11 were acquired. The pump laser appears to be even less well aligned to the tip for this scan. The topographic image features typical smears in the fast scan direction due to stick slip (a friction effect) and the tip picking up and depositing dirt. Due to the small (20 nm) height changes at the Au features, the topographic image shows relatively low contrast.

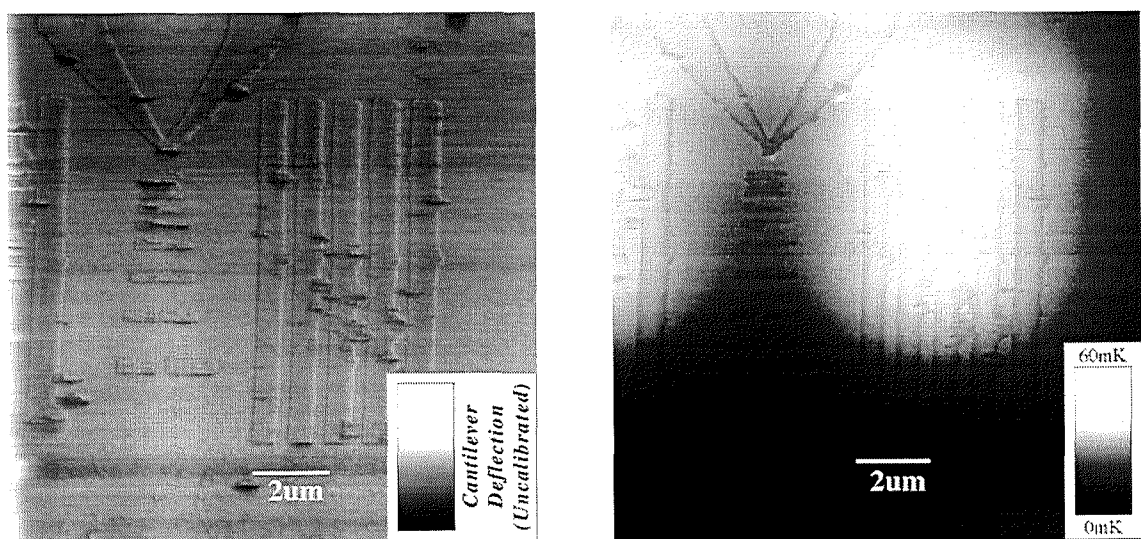


Figure 5-11 Left: Topographic image of the photothermal specimen. Right: Simultaneous temperature image (scale converted to K based on Seebeck coefficient of $12\mu\text{V/K}$).

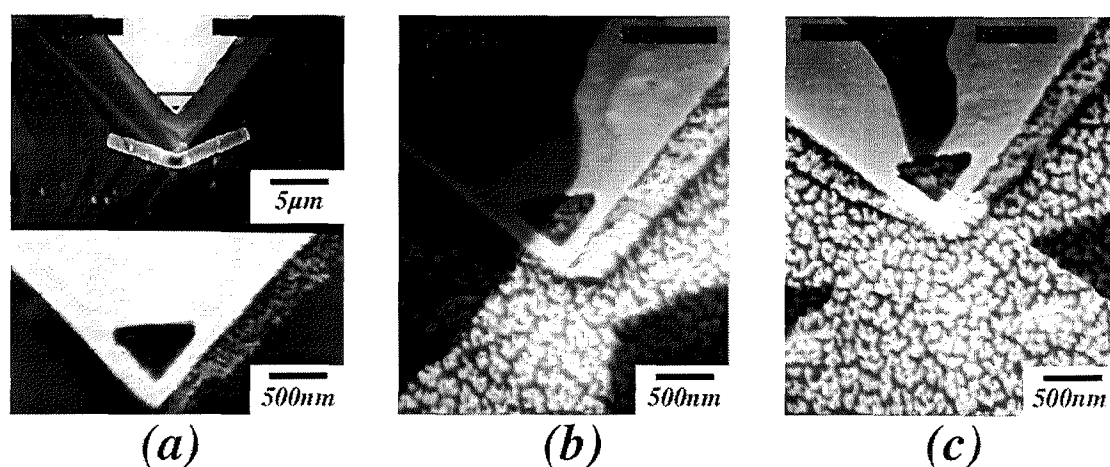


Figure 5-12 “Swiss cheese” thermocouple probe. Left: Dry etch mask for the cantilever. Middle: Au thermocouple wire overlapping the dry etched cantilever. Right: Au and Pd wires forming the thermocouple junction. Misalignment between layers causes the L shaped junction.

Some edge enhancement is apparent in the topographic image which could have been due to ragged edges on the Au features, however edge enhancement in AFM images can also be due to twisting of the cantilever if the tip sticks at an edge. The thermal image shows a distinct dark band round the larger Au features. This is caused by the tip making poor contact at feature edges and results in attenuated heating of the thermocouple. Artefacts in thermal scans are discussed more completely in Chapter 7.

5.5 “Swiss Cheese” Thermocouples

A further modification to the "side" thermocouple probe involved an attempt to align the thermocouple wires in two dimensions by selectively removing parts of the triangular cantilever. Figure 5-12 shows the modified cantilever and the subsequent deposition of the two thermocouple wires. In this case a triangular portion of the cantilever was removed to form a 100 nm wide rail at the apex of the cantilever onto which the thermocouple wires were written. This shape did not lift off reliably (only about 30% were successful), but future attempts improved this by rounding sharp corners (see section 6.5). The thermocouple, which was patterned using a similar design to previous "side" probes, formed an “L” shape at the tip apex due to misalignment between thermocouple levels. The thermocouples were continuous in most cases and measured about 1 k Ω resistance. Due to time constraints, these probes have not yet been tested.

[1] A Practical Guide to Scanning Probe Microscopy: Park Scientific Instruments, 1993.

- [2] A. Majumdar, K. Luo, Z. Shi, and J. Varesi, "Scanning thermal microscopy at nanometer scales - a new frontier in experimental heat-transfer," *Experimental Heat Transfer*, vol. 9, pp. 83-103, 1996.
- [3] M. Parikh, "Self consistent proximity effect correction technique for resist exposure (SPECTRE)," *Journal of Vacuum Science and Technology*, vol. 15, pp. 931-933, 1978.
- [4] *Metals Handbook : properties and selection of metals.*, vol. 1.

6 Resistance Thermometer Probes

6.1 Introduction

A collaboration involving Dr Hubert Pollock, Dr Azzedine Hammiche and latterly Dr Michael Conroy, all of Lancaster University, was started early in the lifetime of this project. The purpose of the collaboration was to make a resistance thermometer probe, using the generic Glasgow probe technology, that could be used to further the extensive research activities at Lancaster into the thermal analysis of polymers. Primary interests of the Lancaster group are high resolution thermal imaging, sub-surface imaging, thermal mapping of polymer blends and localised calorimetry [1-4]. The function of the probe as a combined heater and thermometer was a prerequisite, since for calorimetry in particular controlled heating of the specimen by the probe is required. In this technique a constant rate of energy is transferred to the specimen and the corresponding temperature rise measured as a function of time. Phase transitions are identified by periods in which the temperature of the specimen does not rise even though energy is still absorbed.

The resistance of pure metals varies approximately linearly with temperature [5, 6] and this property is commonly used to make temperature measurements [7]. The resistance variation of platinum with temperature for example is one of the stipulated interpolation instruments for realising the International Temperature Scale of 1990 [8, 9]. In general terms, the mechanism whereby the resistance of a metal increases with increasing temperature is dominated by electron-electron scattering from about 20 K to about 50 K, and electron-phonon scattering at higher temperatures. Below about 20 K resistance is dominated by electron impurity scattering and does not vary with temperature. Above about 50 K (depending on the material) the relationship between resistance and temperature is nearly linear, with platinum particularly so. The operation of metal resistance thermometers is generally good in the range -200 °C to +1000 °C.

The temperature coefficient of resistivity (TCR) α_r is defined as follows,

$$\alpha_r = \frac{1}{\rho_0} \frac{d\rho}{dT} \quad (6.1)$$

where ρ is the resistivity of the metal and ρ_0 is the resistivity at 0 °C. For metals in the approximately linear region above 50 K, ρ can be described by second order polynomial,

$$\rho \approx \rho_0(1 + \alpha T + \beta T^2) \quad (6.2)$$

where ρ_0 is the resistivity at 0 °C and α and β are material constants. Substituting equation 6.2 into 6.1 gives the TCR as,

$$\alpha_r \approx \alpha + 2\beta T \quad (6.3)$$

For a metal to be approximately linear it is clear that β must be much smaller than α . This is true for most metals.

The resistivities and TCR's of common metals are shown in Figure 6-1. Highly resistive alloys such as Nichrome are not suitable for making reproducible thin films, since the evaporation rates of the constituents are different and can lead to local variations in composition. The most sensitive material for temperature measurement is nickel (highest TCR). Nickel is impractical however because it readily oxidizes in air and is ferromagnetic, which means its properties vary nonlinearly with temperature and stress. A good choice would appear to be palladium, which has reasonably high TCR and resistivity. It is also compatible with KOH etching.

Material	Resistivity, ρ ($10^3 \Omega \cdot m$) at 20 °C	TCR, α_r ($10^{-4}/K$)
Nichrome (60%Ni, 16%Cr, 24%Fe)	109.0	2
Constantan (55%Cu, 45%Ni)	49.0	± 0.2
Manganin (86% Cu, 12%Mn, 2% Ni)	43.0	-0.2
Palladium	10.8	37.7
Platinum	10.6	39.2
Iron	9.71	65.1
Indium	9.00	47.0
Nickel	6.84	68.1
Tungsten	5.50	46.0
Rhodium	4.70	45.7
Aluminium	2.69	42.0
Gold	2.30	39.0
Copper	1.67	43.0
Silver	1.63	41.0

Figure 6-1 Table of resistivity and temperature coefficient of resistivity for selected metals [7].

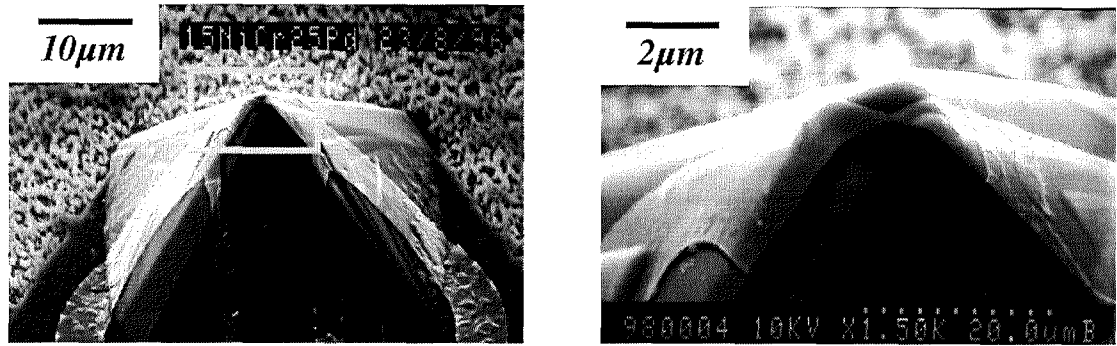


Figure 6-2 Four terminal resistance thermometer design (courtesy of Dr H. Zhou).

6.2 Early Work / Probe Contamination

Using palladium as the resistive material some progress had already been made by A. Midha and H. Zhou. The first design for a resistance thermometer probe is shown (pre-release) in Figure 6-2. The resistor was in the form of a 50 nm thick palladium wire that tapered at the pyramid apex. The reason for the taper was to increase the resistance of the wire at the point of contact thus increasing signal to noise and thermal spatial resolution. The tapers were typically 70-100 nm wide. In addition to the tapered wire, two adjoining wires were added away from the tip apex so that four terminal resistance measurements could be made. Measuring temperature induced resistance changes in this way means that contributions from the parts of the wire away from the pyramid are diminished. Gold pads similar to those used with the thermocouple probes (see Chapter 4) were used to allow external connection to these early probes (gold mirrors on the cantilever were added in later designs).

Two wafers containing 50 probes each were fabricated and supplied to Lancaster by Dr

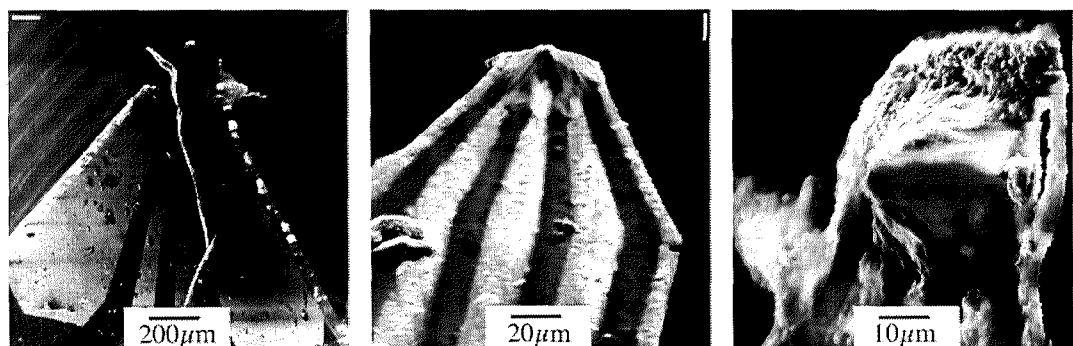


Figure 6-3 SEM micrographs of contaminated four terminal resistance thermometer probes (courtesy of Dr A. Hammiche).

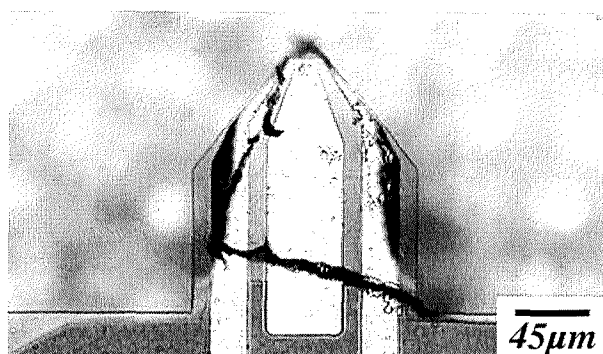


Figure 6-4 "Side" resistance thermometer probe with contamination incurred during the release etch. Later cured by employing a 10 min oxygen ash before release.

Zhou. A scheme for mounting the probes on steel washers and bonding with silver epoxy was then developed by Dr Hammiche (for use in a modified Topometrix Explorer microscope). Topographic scanning using the probes was quickly achieved however scanning in thermal feedback (where the heat lost from the probe to the specimen is regulated by adjusting the tip-specimen separation) proved very difficult and was achieved with only one probe. Examination of the probes by SEM in Lancaster showed that the tips were heavily contaminated with some unknown substance. Figure 6-3 shows SEM micrographs (taken by Dr Hammiche) of the early Glasgow resistance thermometer probes. The contamination was severe and the probes appeared to be almost entirely covered in a fibrous contaminant. The silicon nitride cantilevers also appeared to have been attacked, possibly from residual KOH after release.

The reason for the failure of these probes remains unclear. Post release examination of subsequent batches using electron and optical microscopes has shown that contamination can occur during the release etch (Figure 6-4). It is clear that this contamination, which is attributed to oily deposits from the SEM, is not as extreme as that observed in Figure 6-3. Over a period of some months, typically 20-50% of cantilevers on a wafer were affected by this contamination. This is reasonably consistent with the proportion of probes which are examined by SEM before release. Changing the pre-release wafer clean (10 mins in hot acetone) to include a 10 minutes exposure to oxygen plasma (in a barrel asher) eradicated this source of contamination.

A more destructive problem is degradation of the cantilever silicon nitride due to residual KOH. This has been observed on many occasions, examples of which are shown in Figure 6-5. The degradation of the cantilever surface may occur over a matter of days or weeks depending on the severity of the KOH residue. The post-release etch processing was modified to include neutralisation in weak hydrochloric acid followed by more

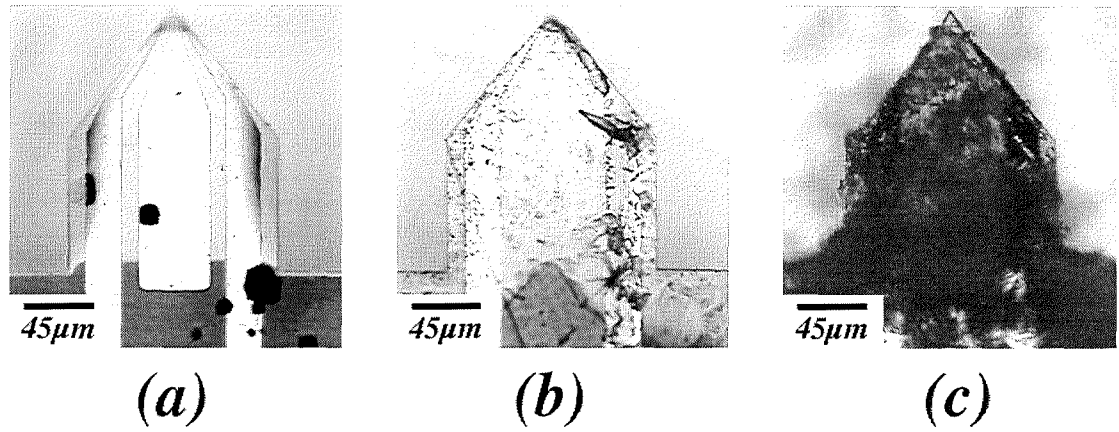


Figure 6-5 Residual KOH on a released cantilever. (a) A clean probe. (b) Residual KOH has degraded the cantilever (although cantilever and sensor may well still be operable). (c) Severe degradation of the cantilever resulting in an inoperable probe.

vigorous rinsing in ultra pure water. After these changes residual crystals of KOH disappeared, and the silicon nitride cantilever ceased to degrade with time.

At this point Dr Zhou moved on to other projects and the responsibility for the fabrication of resistance thermometer probes shifted to the author.

6.3 “Bowtie” Probes

The name “Bowtie” became the common name for the resistance thermometer probes with the wire on a truncated tip. This arose from the shape the taper makes on the

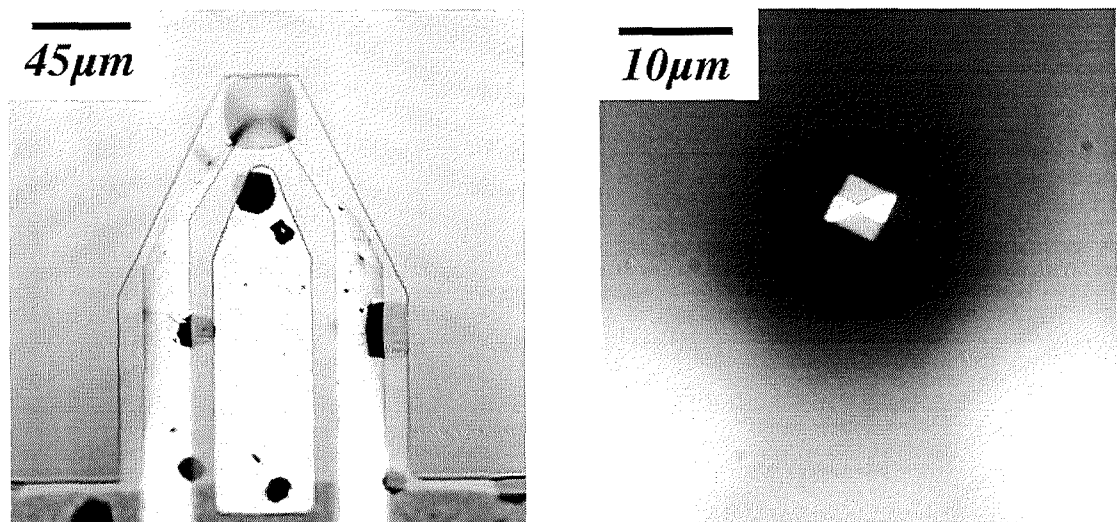


Figure 6-6 Optical images of the conventional Bowtie cantilever and the tip apex showing the “Bowtie” shape which gave the probe its name.

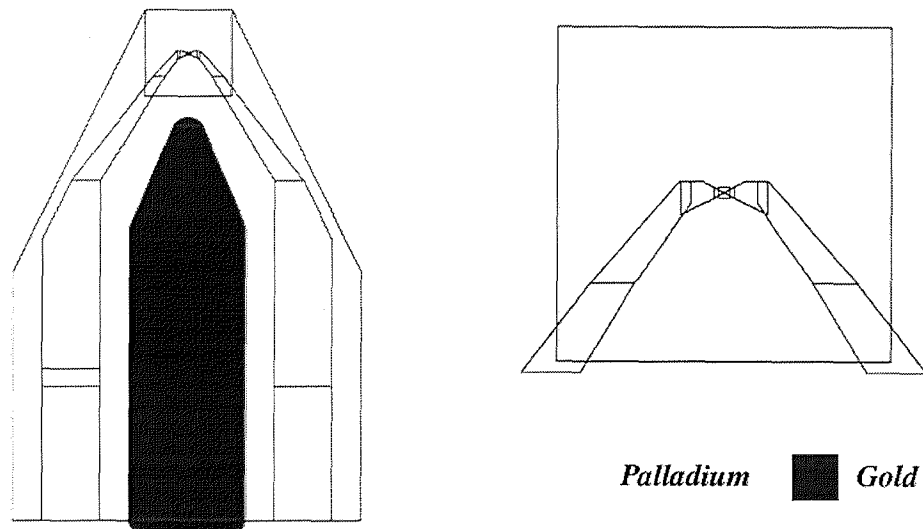


Figure 6-7 CAD patterns for the device layer of the conventional Bowtie resistance thermometer probe.

truncated pyramid tip (Figure 6-6). Before a first attempt by the author to make these probes, the resistor design was simplified to a single two terminal wire. The CAD design for the Bowtie cantilever is shown in Figure 6-7. From previous experience with the thermocouple probes, it was clear that this two terminal shape would be easier to lift off than the more complex four terminal design. Other design changes involved the inclusion of cut-out pads (which are not written as solid shapes to reduce the exposed area), and an optional serial resistor patterned on the probe base away from the cantilever. The inclusion of the resistor was for probes with narrow tapers (≤ 100 nm). The resistor was a simple meander calculated to provide an extra 5 k Ω resistance to the electrical path of the resistor. This would decrease the sensitivity of the resistor to thermal changes at the tip, but would serve to protect the taper from ESD. Wider (≈ 250 nm) tapered wires were also fabricated on the same wafer to ensure that some working probes were produced for initial testing.

Another feature of the first generation of Bowtie probes was that the pads were written with the device level to speed up development time. Connection to the probes are made using silver paste by the Lancaster group, and clips are used at both Glasgow and at Motorola (see Chapter 7), and so a separate layer for gold pads was deemed unnecessary. The device metal was increased from 50 nm to 100 nm to help prevent the clip scratching through the pads to the substrate below, and to reduce EBL job time further a series of gaps were made in the pads. The lithography was excellent and up to this stage almost 100% of the devices were electrically continuous. The increase of thickness and coverage of Pd on the cantilever however was found to be an error, since after release almost every cantilever curled up $\approx 75^\circ$. The result of the pattern change therefore was that a time saving

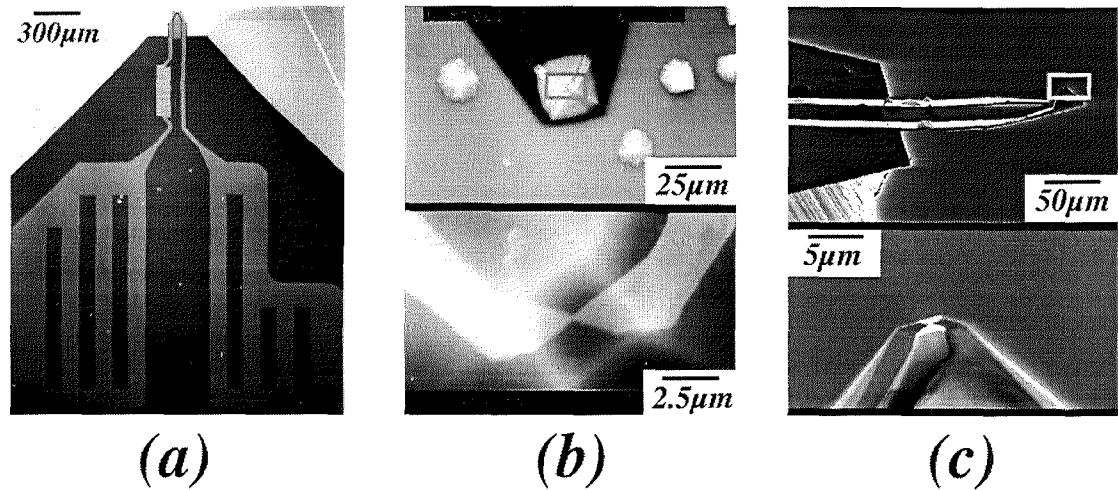


Figure 6-8 (a) & (b) SEM micrographs of a pre-release all palladium Bowtie probe. (c) A side profile of a released conventional style Bowtie probe. Note the bending in the cantilever ($\approx 6^\circ$)

ploy had produced exactly the opposite effect. The bending was attributed to stress built into the metal layer during deposition. Electron images of the single layer Bowtie probes before release are shown in Figure 6-8 (a) and (b).

Two more quarter wafers of Bowtie probes were fabricated, but this time the original scheme with separate Au pads and mirror was used. This allowed the resistor metal thickness to be reduced back to a non-catastrophic 50 nm. Two different Bowtie widths were written (100 and 250 nm) and the protecting series resistor was omitted this time after information from Lancaster showing that relaxed ESD precautions gave no increase in failed probes. Another difference with these particular substrates was that the flat tops of the pyramidal tips measured $4.5 \mu\text{m}^2$. The reason for these large tops was simply that these substrates (which had been originally intended for side probes) were all that happened to be available at the time. Specimen access in the final probes would be poor, but the thermal image was still expected to provide resolution of the order of the Bowtie taper for flat specimens.

The critical lithography was again excellent for this pair of substrates, with over 90% electrical continuity of resistors. After release this figure dropped marginally due to the occasional mechanical failure. The released probes (shown in Figure 6-8(c)) were tested using a Hewlett Packard parameter analyser (Model No. 8514A). Probe resistances of approximately 700Ω at room temperature were measured. Normally a compliance of $100 \mu\text{A}$ was imposed so as not to over stress the resistors however, in order to observe the non-linearity of the resistance as a function of electrical heating, larger voltage sweeps were used without current limitation. Figure 6-9(a) shows a plot of voltage across the

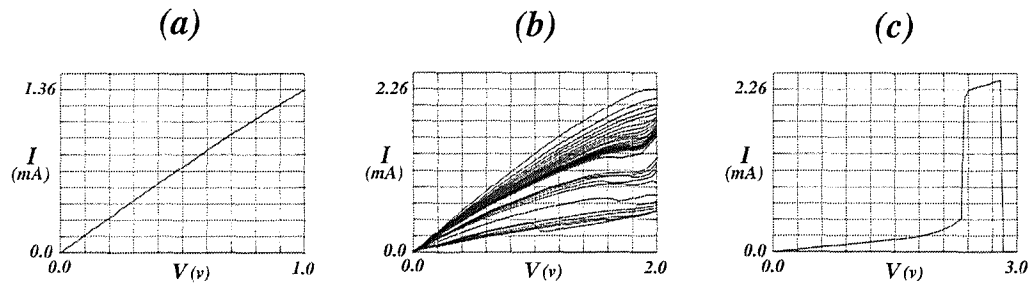


Figure 6-9 (a) Current versus voltage (IV) plot for conventional Bowtie probe. (b) Series of IV plots showing the degradation of the Bowtie probe during electrical overstress. (c) Final IV plot showing the probe becoming open circuit.

resistor versus current. The resistance is measured to vary from 715Ω at negligible current to 830Ω at around 1.3 mA . This is a 17% change in resistance due to electrical heating, and gives a measure for the probe sensitivity. The voltage was increased to discover the maximum current allowable. Figure 6-9(b) shows a series of plots over a driving voltage range of $0\text{-}2 \text{ V}$. The voltage sweeps were performed approximately every 10 seconds and overlaid onto a single graph. The first plot is uppermost on the graph. When approximately 2.2 mA is reached on the first sweep, the resistance of the probe increases dramatically. The second sweep (second from top) shows the resistance of the probe to have increased by a few Ohms at low current, with a marked increase in resistance observed at approximately 2 mA . This trend continues with the resistance of the probe increasing to approximately $3 \text{ k}\Omega$ after around 25 sweeps. The probe appeared to stabilise at this point. Figure 6-9(c) shows a final voltage sweep from $0\text{-}3 \text{ V}$, after which the probe became and remained open circuit. The failure mechanism here was presumed to be electrical over stress resulting in electromigration which thinned and eventually cut the wire at the tip apex. After final inspection, cleaving and packaging, some similar (but unstressed) probes were shipped down to Lancaster for scanning.

Several tests were carried out using the Bowtie probes at Lancaster by Dr Azzedine Hammiche. As always these were carried out in the modified Topometrix Explorer AFM. These tests included:

- Topographic scanning using force feedback of standard test structures.
- Thermal scanning of polymer interfaces.
- Comparison of thermal sensitivity and spatial resolution with Wollaston wire probe.
- Thermomechanical measurement of the polymer polycaprolactone (PCL).

Topographic scanning was achieved by deflecting the height sensing laser off the Au mirror on the cantilever. One problem however was that the probes were bent away from the normal by about 10° due to stress caused by the Pd wires on the cantilevers. Most of the probes were difficult to align because of the limited optical path from the probe to the detecting photodiode in the Explorer microscope. It was observed that the laser signal increased significantly when the probe was brought into contact with the specimen surface. This was due to the contact forces bending the cantilever back into alignment range. Once this had occurred force feedback was easily maintained, albeit with excessive contact forces.

One result of particular interest was a thermal scan of a microtomed PET/Resin interface, shown in Figure 6-10. Here a comparison of thermal spatial resolution was made with the Wollaston wire probe (provided as the standard probe for the Explorer thermal microscope). The Wollaston probe is made from a silver clad platinum wire which has been manually fashioned into a cantilever shape with protruding tip. A piece of metal foil is glued onto the back of the cantilever to facilitate force detection. The silver cladding ($75\ \mu\text{m}$ diameter) is chemically etched away at the tip to expose the platinum core ($5\ \mu\text{m}$

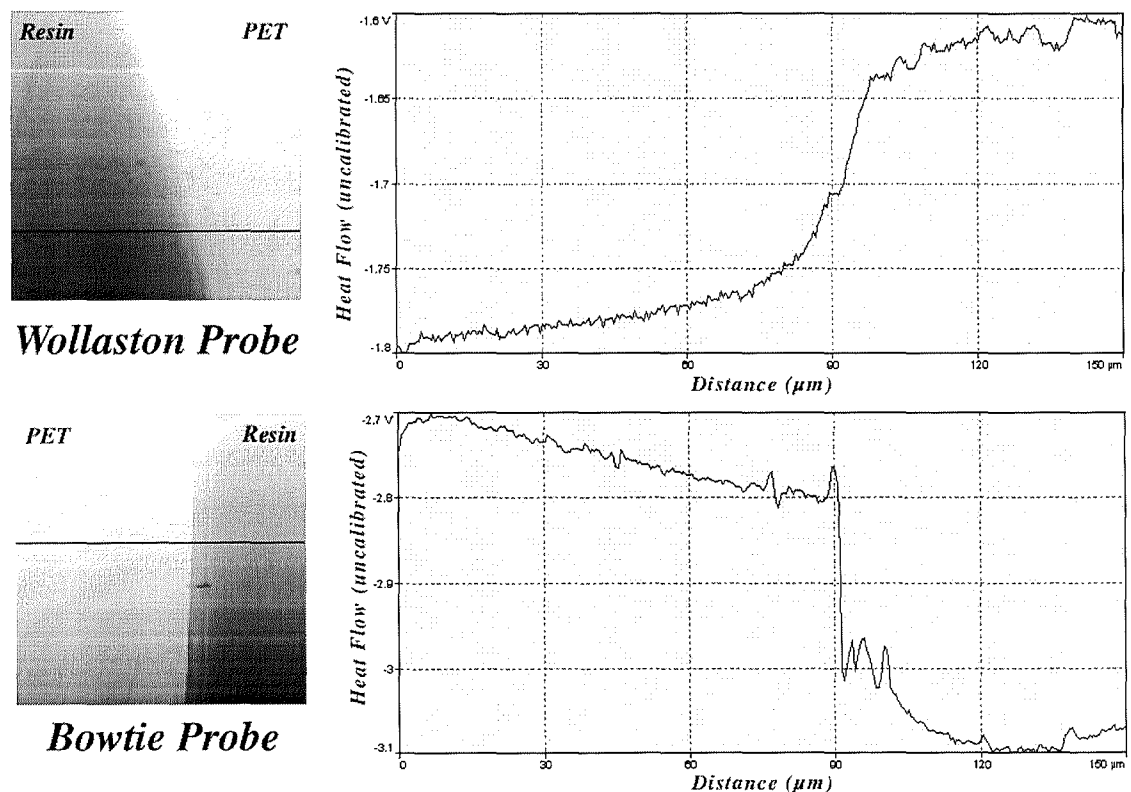


Figure 6-10 Heat flow images of a microtomed PET/Resin interface using both the Wollaston and Bowtie probes. Positions of the line plots are indicated on the corresponding images (courtesy of Dr A. Hammiche).

diameter). The tip radii are nominally $7\mu\text{m}$ however it is believed that smaller actual tips are formed from random asperities. The scans show that the Bowtie probe is capable of significantly higher thermal spatial resolution than the Wollaston wire probe. The contrast is caused by the difference in thermal conductivities of the different materials. Measurements made by Dr Hammiche of the rise lengths at the thermal interface gave values of $30\mu\text{m}$ for the Wollaston wire probe and $1.5\mu\text{m}$ for the Bowtie probe. These scans were not taken at exactly the same location on the interface and so it is possible that topography differences contributed to differences in the riselengths. Subsequent scans, where care was taken to scan the same location, still showed the micromachined probes to be superior to the Wollaston wire probes, but by factors of two to five. It is possible however that the dominant factor here is the variability of the tip shapes of the Wollaston wire probes.

Attempts were made to acquire thermomechanical measurements of a PCL specimen. These are fixed point measurements and involve increasing the current in the integrated resistor in order to heat the specimen. Changes such as expansion and melting of the polymer cause deflections of the cantilever which are measured using the force sensing laser. Unfortunately results were not reproducible due to the difficulty in getting the force sensing laser to deflect from the cantilever (bent by 10°), however the probe did appear to respond to events such as melting in some cases.

6.4 Enhanced Sensitivity Probes

A significant change to the Bowtie probe design was made in order to improve performance. The reasons for this were twofold 1) to increase the sensitivity ($\Omega/\Omega^\circ\text{C}$) of the resistance measurement, and 2) to reduce the undesired bending of the cantilever due to stress in the Pd wires. The idea was to replace a portion of the 50 nm thick Pd metal on the probe with the pad and mirror metal (100 nm Au). The only remaining Pd would be in the

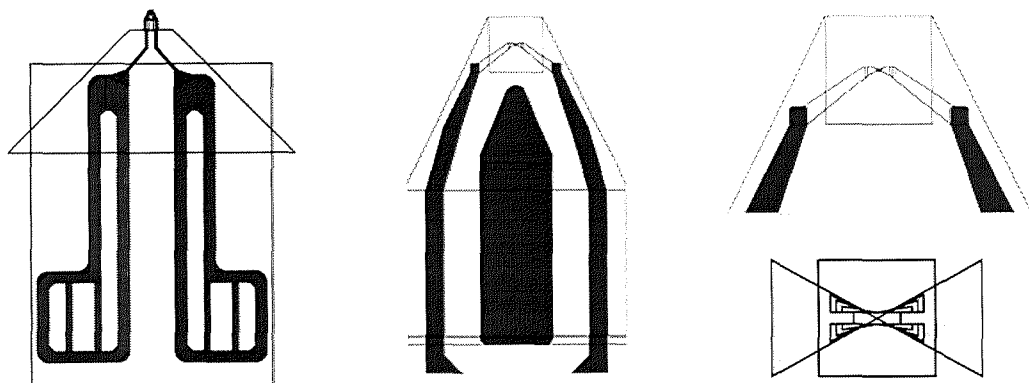


Figure 6-11 CAD drawing for the enhanced sensitivity Bowtie probe.

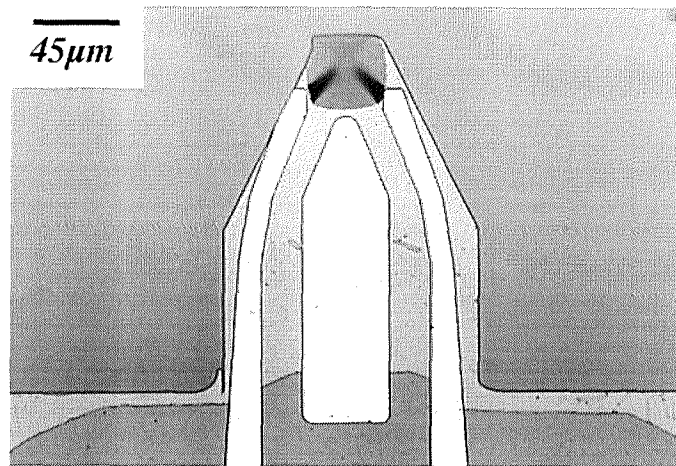


Figure 6-12 Optical micrograph of released enhanced sensitivity Bowtie probe.

form of a strap extending over the pyramid, but not beyond the pyramid base. Figure 6-11 shows CAD drawing of the enhanced sensitivity design. Assuming satisfactory contact between the metal levels at the pyramid base, there would be lower overall resistance and in turn an increase in the ratio of active resistance at the tip to total resistance. In addition, the removal of a large fraction of the stressed Pd layer from the cantilever was expected to result in less bending of the cantilever after release. The resistor leads on the cantilever were halved in width to further enhance this effect.

A wafer containing both the new enhanced sensitivity probes, and some of the earlier conventional design probes, was processed by Lesley Donaldson (a technician in the department) under instruction of the author. The fabrication of the probes was successful, however approximately one third of the probes died due to open circuits caused by under exposure/development at sites where float coat wrinkles were to be found. This problem was traced to a gradual loss of calibration of the beam current measurement system on the beam-writer, and is now fixed. A recurrence of the spurious contamination during release also rendered another third of the devices useless, however as mentioned in Section 6.2 this problem was fixed at a later date. Figure 6-12 shows an example of the enhanced sensitivity probes after final release. Taper width at the apex of the pyramid was 125 nm for both conventional and enhanced sensitivity probes.

Initial optical examination showed that the conventional probes (i.e. those with half width Pd leads on the cantilever) were angled away from the substrate approximately 3° compared to approximately 6° for those with normal width leads. In contrast, the enhanced sensitivity probes (i.e. those with half width Au leads on the cantilever) were essentially flat having a bend angle of only about 0.5° . These values were wholly attributable to the volume and extent of the Pd on the cantilevers. Electrical test of the probes showed that

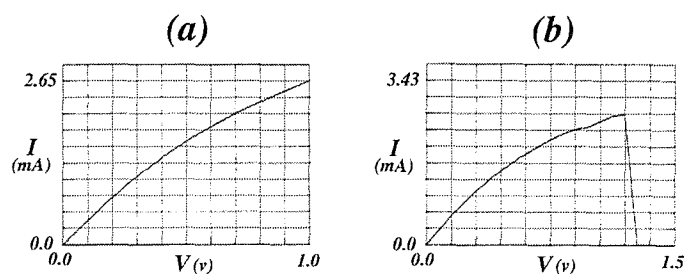


Figure 6-13 (a) IV plot for the enhanced sensitivity Bowtie probe (same voltage range as Figure 6-9(a)). (b) The enhanced sensitivity Bowtie probe becomes open circuit at approximately 2.5 mA which is comparable to the conventional probe.

total resistance of the enhanced sensitivity probes was 250Ω at room temperature compared to 700Ω for the conventional design. Figure 6-13(a) shows an IV plot of the resistance of the enhanced sensitivity probe with identical voltage scale to Figure 6-9(a). As expected, the variation of resistance due to electrical heating at the taper is more pronounced than with the conventional probe. The resistance change for a current of 1.35 mA (comparable to full scale on Figure 6-9(a)) was 120Ω . This is the same as the figure for the conventional probe at this current, but represents a 48 % change due to lower overall resistance. This makes the relative change in the enhanced sensitivity probe almost three times larger than that of the conventional probe. This suggests that the temperature induced resistance change is indeed governed by the tapered portion of the Pd resistor at the tip apex, which was common to both probes. Further change in the extent and geometry of the Au leads and Pd resistor should result in further enhancement of device sensitivity.

Figure 13(b) shows the maximum allowable current for the enhanced sensitivity probes to be around 2.5 mA. This is comparable to the earlier design of Bowtie probe.

Testing of the enhanced sensitivity probes continues at Lancaster University, however it has already been shown that it is much easier to align the force sensing laser with these probes which makes high resolution imaging routine and local thermal analysis much more reliable. Examples of scans using the enhanced sensitivity probes are shown in Figure 6-14. Figure 6-14(a) and (b) show topographic and heat flow images of a cleaved resin/metal interface. Some topography is evident at the boundary in the form of a trench running down the centre of the image. In the heat flow image strong contrast is produced due to the lower thermal conductivity of the resin compared to the metal. Further, it is shown that the trench is in the resin not the metal. Figure 6-14(c) shows thermomechanical plots of PCL. Thermal expansion of the material is observed before a sharp melt, which is known to be at 60°C . The results were relatively reproducible, however some problems

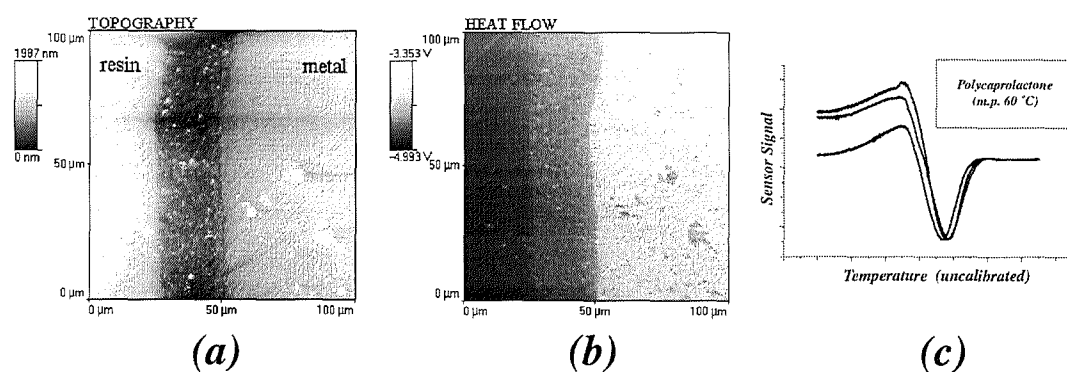


Figure 6-14 (a) Topographic scan of a cleaved resin/metal interface using an enhanced sensitivity probe. (b) Corresponding heat flow image. (c) Thermomechanical plot for PCL using an enhanced sensitivity probe (scans courtesy of Dr M. Conroy).

were experienced with the probe sinking into the molten polymer and breaking on retraction. Possible solutions to this involve using lower contact forces, engaging force feedback, and heating the probe to its maximum as it is retracted. Further characterisation of the probe will involve determination of the thermal time constant of the probe, investigations into the anisotropy of the sensor in imaging mode, and calorimetric measurements of polymers. It is expected that the micromachined probes will also contribute to new imaging techniques being developed at Lancaster, including scanning thermal expansion microscopy (SThEM) and photothermal FTIR spectroscopy [10].

6.5 Self Aligned Resistance Probes

It was realised from an early stage that the strategy for improving the access of the thermocouple probes (see Chapter 5) would also be applicable to the resistance thermometer probes. Especially interesting was the “Swiss cheese” design where a portion of the cantilever was removed to further localise the sensor to the tip. In the case of the thermocouple, the dimensions of the sensor were still subject to variation due to EBL misalignment, however if the sensor were a single wire (as with resistance thermometer probes) then the cantilever shape could entirely define the critical device dimensions. This would mean that only the cantilever definition level would require high resolution lithography, and the sensor shape and location would be entirely self aligned in all directions.

The first step was to design a “Swiss cheese” side resistance thermometer cantilever shape. Figure 6-15(a) and (b) show SEM micrographs of the dry etch mask for the silicon nitride cantilever and the post etch deposition of the 50 nm thick Pd resistor layer

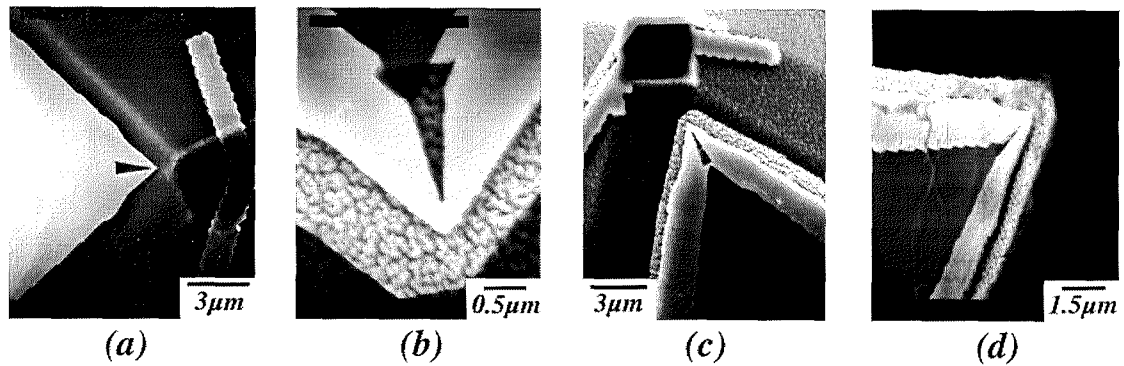


Figure 6-15 (a) Dry etch mask for an early side resistance thermometer cantilever. The hole in the tip has not lifted off satisfactorily. (b) & (c) Side probe after the resistor metal level has been lifted off. Note that in (b) the device is not affected by misalignment whereas in (c) a short circuit has occurred. (d) A shroud of metal and silicon nitride remains after release - removed in later wafers by increasing the cantilever dry etch depth.

respectively. The shape of the hole in the cantilever has been changed from the thermocouple design to preserve the taper in the wire at the tip apex (not needed with the thermocouple probes). The lift off in Figure 6-15(a) was poor, although a portion of the hole did lift off. The intended shape of the hole is shown in Figure 6-15(b) which lifted off satisfactorily. The cause of the poor lift off was attributed to under development of the sharp corners of the structure. Figure 6-15(b) also shows the deposition of the oversized resistive metal wire which entirely overlaps the cantilever edges and the hole. The metal layer in this particular case is misaligned, however since the shape of the cantilever dictates the resistor shape and alignment, the sensor is unaffected. The hole limits the width of the wire at the tip apex to 150 nm. Figure 6-15(c) shows a case where a poorly lifted off hole causes a short circuit in the resistor away from the tip. Some good probes were fabricated despite the lift off difficulties and were released after the usual Au pad level. An example of these probes is shown in Figure 6-15(d).

An unintended feature of the probe, which was common to all the probes in this batch, was that a strange shroud surrounded the tip apex. It appears that the silicon nitride cantilever had not been dry etched satisfactorily, causing unwanted parts of the metal resistor to fail to detach during release. It can be deduced from the fact that the whole pyramid is not intact that the dry etch was very close to completion, and that the metal deposition somehow acted as an adhesive for the shroud. A mistake had been made in assuming that the vertical thickness of the silicon nitride was the same on the pyramid wall as on the flat. If the thickness of the nitride is 500 nm and uniform over the wafer, then the depth which must be etch is in fact 785 nm (see Figure 6-16). Further examination showed that the shroud was not electrically contacted to the cantilever and so, on the assumption that some

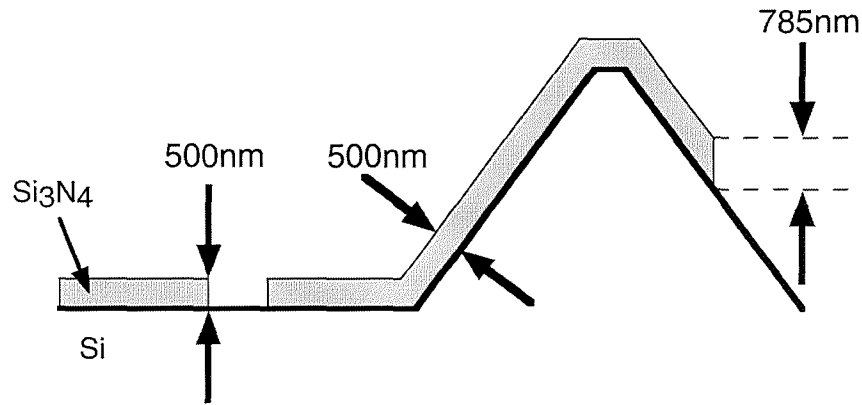


Figure 6-16 If there is a uniform coating of 500 nm thick silicon nitride on a generic substrate, then an etch depth of 785 nm is required on the pyramid sidewall if the film is to be completely removed.

sort of thermal sensor remained, some of these imperfect probes were taken to be scanned tested in a commercial microscope (see Chapter 7).

Figure 6-17 shows the CAD pattern for a new design of cantilever for "Swiss cheese" resistance thermometer probes. To remedy the problem of poor development of the hole in the cantilever, an attempt was made to round the sharp edges of the feature. The resulting lift off was much better with approximately 80% satisfactory structures. The dry etch time was also increased from 20 mins to 30 mins (600 to 900 nm depth). Figure 6-18(a) and (b) show the new cantilever shape after dry etch. The NiCr mask tip radii were improved to below 50 nm as shown in Figure 6-18(c), however this degraded after RIE to

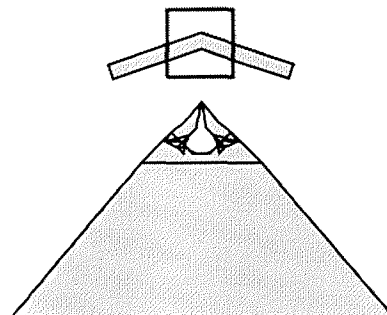


Figure 6-17 CAD drawing of the "Swiss cheese" resistor probe. The hole is now rounded to aid lift off.

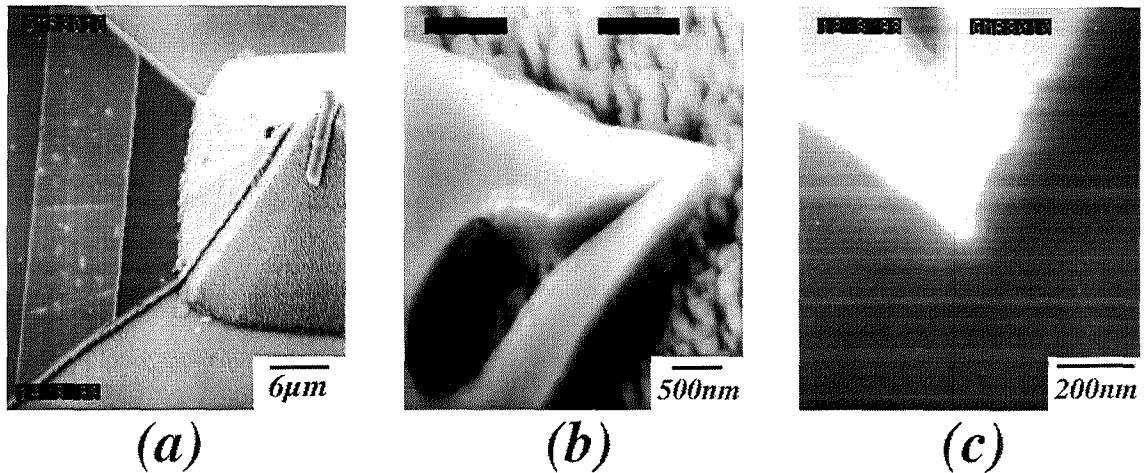


Figure 6-18 (a) & (b) SEM micrographs of “Swiss cheese” cantilevers after the increased dry etch. (c) SEM micrograph of the Nichrome dry etch mask before etching which will form the sharp tip.

approximately 100 nm due to mask erosion. The metal wire was patterned as before, but with a greater success rate due to the improved cantilever definition. The pad level caused unexpected problems in that in a large fraction of the pyramids were capped with thick gold. This was attributed to the effect of the extended dry etch on flat areas of the specimen. Figure 6-18 (b) shows the etched surface where the silicon nitride has been partly removed. The remaining silicon appears to have been roughened by the etch. This is often called “grass”, and is the result of the extended dry etch damaging the silicon surface. The adhesion of the pad layer was later fixed by increasing the resist thickness for the pad layer.

Figure 6-19 shows several SEM micrographs of released “Swiss cheese” resistance thermometer probes which avoided capping of the pad layer. All the sacrificial metal

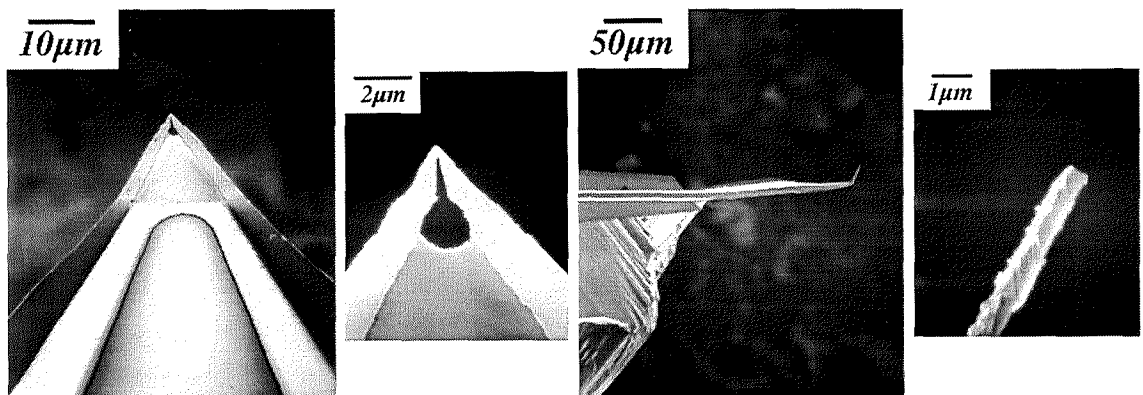


Figure 6-19 SEM micrographs of released “Swiss cheese” resistor probes with magnified images of the tip.

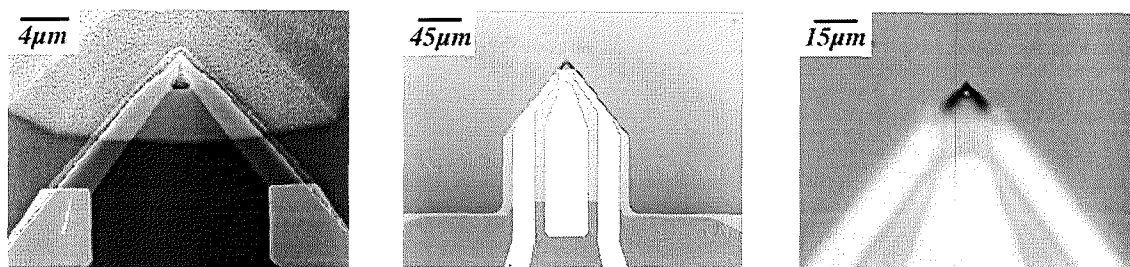


Figure 6-20 SEM (pre-release) and optical micrographs of enhanced sensitivity side resistor probe.

surrounding the probe tips has detached during release this time. It can be seen from the side profiles that the cantilevers were bowed slightly due to the stressed Pd wires. This was reduced when an enhanced sensitivity version of the side resistor probe was produced (Figure 6-20). Electrical probing confirmed that the probes were continuous and similar to the Bowtie probes in resistance. Testing of the enhanced sensitivity probes goes on.

- [1] A. Hammiche, D. J. Hourston, H. M. Pollock, M. Reading, and M. Song, "Scanning thermal microscopy - subsurface imaging, thermal mapping of polymer blends, and localized calorimetry," *Journal Of Vacuum Science & Technology B*, vol. 14, pp. 1486-1491, 1996.
- [2] A. Hammiche, M. Song, H. M. Pollock, and D. J. Hourston, "Phase-separation of miscible blends - study by sthm and m-t dsc," *Abstracts Of Papers Of the American Chemical Society*, vol. 212, pp. 186-PMSE, 1996.
- [3] A. Hammiche, M. Reading, H. M. Pollock, M. Song, and D. J. Hourston, "Localized thermal analysis using a miniaturized resistive probe," *Review Of Scientific Instruments*, vol. 67, pp. 4268-4274, 1996.
- [4] A. Hammiche, H. M. Pollock, M. Song, and D. J. Hourston, "Subsurface imaging by scanning thermal microscopy," *Measurement Science & Technology*, vol. 7, pp. 142-150, 1996.
- [5] *Solid State Physics*: Cambridge University Press, 1974.
- [6] *The Solid State*: Oxford Science Publications, 1978.
- [7] J. W. Gardner, "Microsensors," *Wiley Press*, 1994.
- [8] H. E. Sostmann, "Fundamentals of thermometry Part 3 - The standard platinum resistance thermometer," www.its_90.com.
- [9] H. E. Sostmann, "Fundamentals of Thermometry Part 1," www.its_90.com.
- [10] A. Hammiche, H. M. Pollock, M. Reading, M. Claybourn, P. H. Turner, and K. Jewkes, "Photothermal FT-IR spectroscopy: A step towards FT-IR microscopy at a resolution better than the diffraction limit," *Applied Spectroscopy*, vol. 53, pp. 810-815, 1999.

7 Studies at CASE Collaborator

7.1 Introduction

As part of the EPSRC CASE collaboration, it was necessary for the author to spend a period of three months in the employ of the project sponsors, Motorola. It was decided that this should take place in Mesa, Arizona at the Materials Characterisation Laboratory (MCL) which was then part of the Materials Research and Strategic Technologies (MRST) division. A programme of work was devised which included use of a commercial AFM by *Digital Instruments*²⁴ (DI), which had been modified for SThM. The remit of the project was to investigate the application of SThM with specimens relevant to the industrial activities at Motorola, and where possible to make a comparison of the commercial SThM probes with Glasgow thermal probes.

7.2 Thermal Probes

The probes used in this investigation came from two sources, DI and Glasgow University, and were made using Focused Ion Beam (FIB) and Electron Beam Lithography (EBL) respectively. All probes were resistance thermometer probes.

The DI probes, fabricated by Mark Wendman of DI, are conventional silicon nitride AFM probes²⁵ which have been modified to incorporate a resistor in the form of a metal strap over the tip apex. The probes consist of two pads for electrical connection made by first coating the front face of the probe with Al, then using an FIB to mill a 1 μm gap all the way up the substrate, onto the cantilever and over the tip. In a second step, again using the FIB, a platinum strap is deposited across the two pads over the tip apex. The resistances are trimmed if necessary by adding more metal in a second deposition stage to achieve a probe resistance of 1-2 k Ω . Due to the significant thickness deposited (200-400 nm), the initial tip radius of around 100 nm changes to a roughly circular flat apex which is approximately 750 nm in diameter. Figure 7-1 shows a set of SEM micrographs of the probes.

Two types of Glasgow University probe were used, the “Bowtie” (see Section 6.3) and improved access (“side”) resistance probes (see Section 6.5). Unfortunately, both kinds of probe were in a relatively immature state of development, and as such most examples were sub-optimal at this time. As described in Chapter 6, an unwanted shroud of partly

²⁴ Digital Instruments 112 Robin Hill Rd, Santa Barbara, CA, USA.

²⁵ Nanosensors GmbH IMO-Building, Im Amtmann 6, Wetzlar-Blankenfeld, Germany.

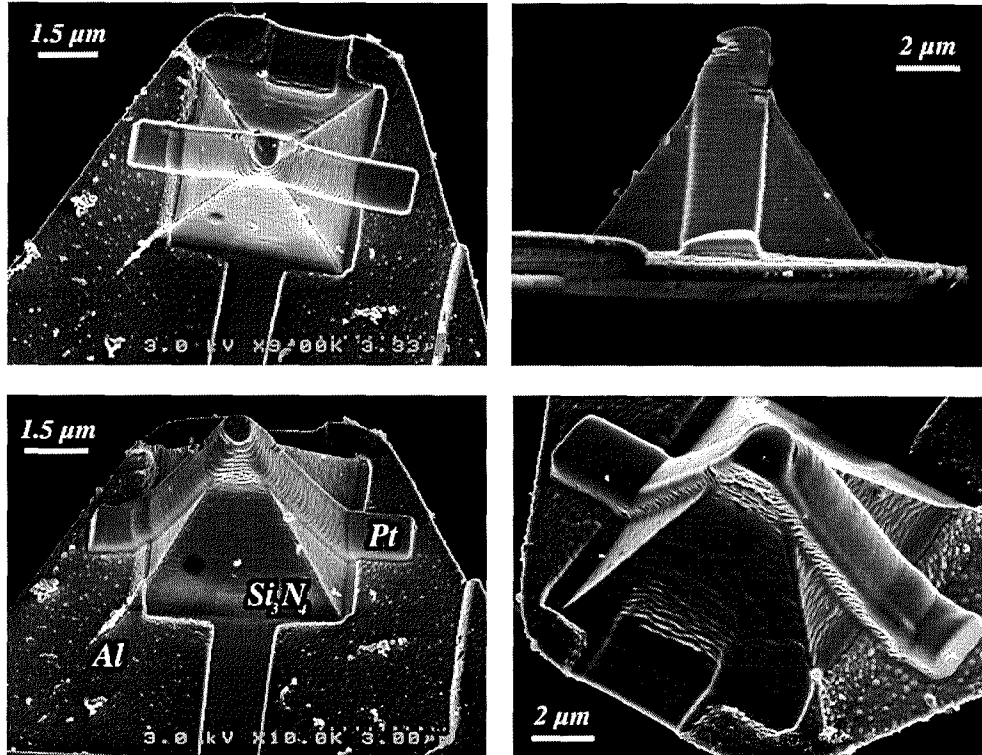


Figure 7-1 Scanning electron micrographs of the Digital Instruments thermal resistance probe.

etched nitride and metal surrounded early examples of the side tips. This problem was subsequently remedied, but unfortunately not in time to impact experiments at Motorola. Cantilever bending due to excessive Pd thickness and coverage also affected all but two of the Bowtie probes available for transportation to Motorola. The poor quality of the Glasgow probes at this time, limited investigations but provided some basis for comparison with the commercial technology.

Resistance thermometer probes are vulnerable to electrostatic discharge (ESD) [1]. Precautions when using the commercial probes involved wearing a grounding strap at all times, using a low current multimeter to measure probe resistance (i.e. not an autoranging meter), and using a special grounded tip holder. These precautions seemed excessive since the Glasgow probes are three orders of magnitude smaller than the DI probes in terms of sensor volume. Experiences of the author, and co-workers at Lancaster, using the Bowtie probes suggest that these probes are not routinely affected by ESD unless the critical dimensions of the sensor are below approximately 100 nm.

7.3 Experimental Setup

Facilities at Motorola MRST in Phoenix, Arizona were substantial and included a Digital Instruments Dimension 3000 AFM, a Micrion Focussed Ion Beam (FIB) machine, a Physical Electronics Scanning Auger Spectrometer, Hitachi SEMs and Zeiss optical microscope.

The Dimension 3000 AFM includes an eight inch motorised stage, piezo tube scanner [2] with 90 μm of travel in x and y, top view CCD camera, beam deflection force detection [3] (see Figure 1-2) and automatic tip approach. In this particular AFM, the specimen is fixed during scanning and the tip moved in x, y, and z. The thermal option for the machine was also fitted which changes the AFM so that it can be used with the DI thermal tips. Modifications include the incorporation of a Wheatstone bridge and operational amplifier in the scanning head with external gain and balancing resistor controls. The thermal probe holder differs from the conventional DI holder (Figure 7-2) in that it does not have a dithering Z piezo but instead has a two pronged metal clip for making electrical connection to the probe. The prongs are electrically insulated from each other during scanning, however a rotating bar at the base of the clip allows the prongs to be either lifted for mounting the probe or shorted together for protection from ESD and transient effects during connection to the microscope. Fortunately, no further modification of the tip holder or electronics was needed to use the Glasgow probes in the DI machine. The twin Au pads on the Glasgow probes were ideally placed for good electrical connection and the resistance of the probe was sufficiently similar to that of the DI probes to be able to be balanced by the variable balancing resistor already present in the modified electronics.

Due to resistance differences between the DI thermal probes, a procedure for normalising the sensitivity of the probes was performed before scanning. The beam deflection laser,

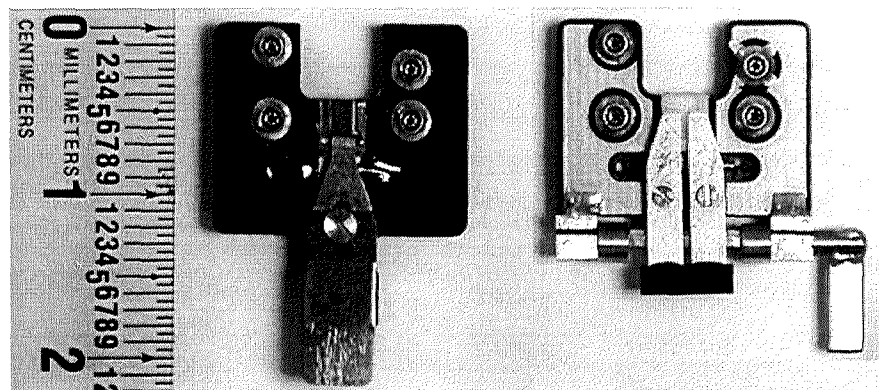


Figure 7-2 (a) Standard tip holder with single metal clip. (b) Thermal holder with twin clips and rotating bar.

which is aligned to the cantilever for force detection, is used to heat the probe. The voltage across the probe is then adjusted to be approximately 6 V by trimming the amplifier gain and variable resistors (2 k Ω and 200 Ω) on the balancing arm of the amplifier. Current in the DI probes is typically 400 μ A during normal operation, depending on the resistance of the probe. The DI microscope does not allow for the current in the probe to vary (other than due to external effects) so modulating the probe current and detecting with a lock in amplifier was not possible, i.e. only dc heating and detection was available.

7.4 Probe Characteristics

Both the DI and Glasgow probes are bimaterial strips since they have metal coatings on the front face of a silicon nitride cantilever. Bimaterial strips bend when heated, and this was also found to be the case with the SThM cantilevers. Sources of cantilever heating include

- Electrical heating from biasing of the integrated resistor.
- Optical heating from the force sensing laser.
- Conduction of heat to and from a specimen through tip contact.
- Convection from to and from a specimen across an air gap.
- Radiative exchanges of heat from specimen to cantilever.

As the cantilever is heated or cooled and bending occurs, care must be taken to anticipate and compensate for the resulting changes in force of contact with the specimen. Issues like tip wear and specimen deformation can be greater if excessive force is used, and the tip may intermittently lose contact with the specimen if too small a contact force is used. In order to measure the heating of the cantilever, temperature-distance curves for each of the probes was acquired. These graphs are plots of temperature (measured using the integrated resistor) versus distance from a specimen. It is useful to compare the temperature-distance curves with simultaneously measured force-distance curves, which are plots of cantilever deflection (measured using the force sensing laser) versus distance from specimen. The coincidence of physical events such as contact with the specimen and thermal events such as a step change in probe temperature may be observed using this technique.

The force-distance and temperature-distance curves for the three different probes are shown in Figure 7-3. The side and bowtie probes were contacted to gold surfaces for these curves, whereas the DI probe was contacted to a silicon surface. The curves show that in the case of the DI tip, the temperature of the probe drops as it nears the surface presumably due to radiative and convective heat transfer into the approaching surface. The cantilever responds by deflecting towards the specimen surface. At the point of contact

with the surface the temperature of the probe drops abruptly, due to heat conduction at the tip, and the cantilever attempts to bend further towards the specimen. This is prevented however by the presence of the surface and so results in the application of a significant force to the surface. The cantilever deflects away from the specimen as the force is increased and the probe resumes its gradual decrease in temperature because of decreasing air gap between the cantilever and the surface. Figure 7-4 shows a graphical representation of the cantilever descent and the associated heat transfer and cantilever deflection.

The hysteresis in the temperature-distance curves is caused when the probe is retracted and allowed to bend towards the specimen surface (while maintaining contact). This appears similar to the pullout force experienced by conventional tips due to the ubiquitous water layer found on surfaces in air at room temperature. An increase in these capillary forces is inevitable because of the greater tip radius of the DI thermal probe, but it is the view of the

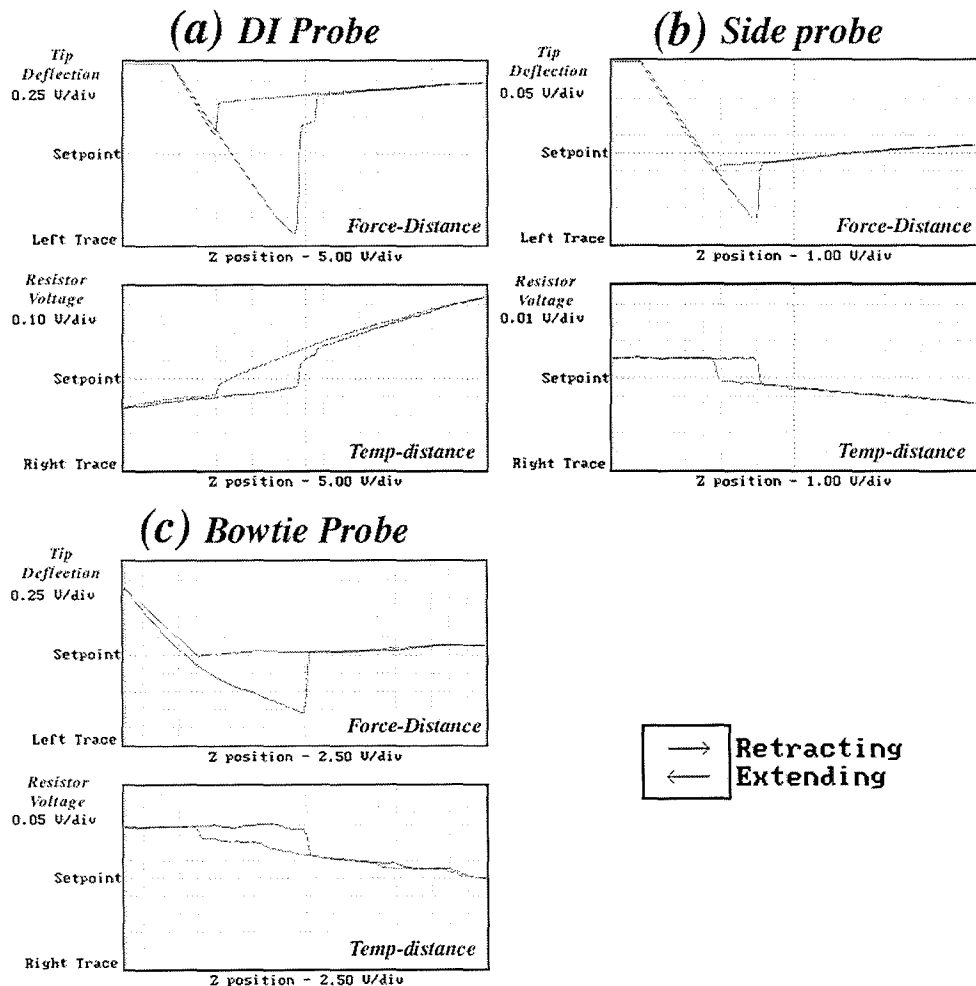


Figure 7-3 Force/Distance (top) and Temperature/Distance (bottom) curves for (a) the DI thermal probe, (b) the Glasgow improved access resistance thermometer probe, and (c) the Glasgow Bowtie probe.

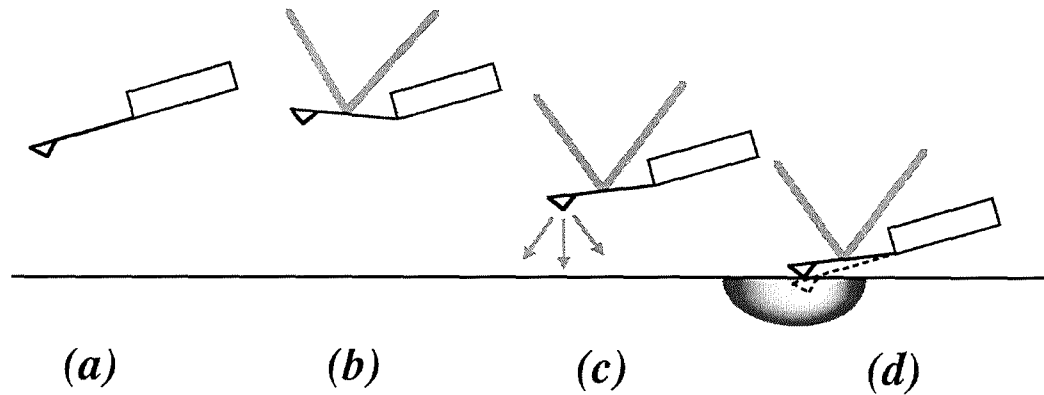


Figure 7-4 (a) Unheated probe. (b) When heated with the laser, the probe bends away from the surface. (c) As the probe descends it loses some of its heat to the surface begins to bend back towards the surface. (d) When the probe makes contact, the probe experiences a step decrease in temperature and would like to assume its unheated position (dashed lines). This is not possible due to the presence of the surface and so a force is exerted on the surface.

author that the hysteresis is dominated by thermally induced bending of the cantilever. As the tip is retracted and loses contact with the specimen, it suddenly loses all conductive heat-sinking. The tip rapidly heats up to its pre-contact temperature after losing contact, and deflects abruptly away from the surface to its original position. Performing this experiment in vacuum, where most of the surface water layer is removed, would give a better understanding of the contribution of the capillary effect to this observation. It is important to note that if minimum force scanning is desired, then the position just before the tip loses contact on retraction is the point of zero force between tip and specimen, not at the point of contact during approach.

The improved access and Bowtie probes showed similar effects to those seen with the DI tip but with two important differences. Firstly the polarity of the resistance change was opposite to that with the DI tip, and secondly the magnitude of the temperature induced deflections was significantly less than that for the DI tip. The polarity difference was attributed to the different material composition of the resistors. In the case of the Glasgow probes, the resistors were deposited using electron beam evaporation of a pure electronic grade palladium source. The DI resistor was deposited by using an FIB to decompose an organometallic and, although nominally platinum, such deposits are known to contain large amounts of carbon and oxygen (plus other stray contaminants from the chamber) [4]. With enough carbon contaminant, a material may change its properties from those of a metal (where resistance increases with heat due to increased scattering) to those of a

semiconductor (where resistance can decrease due to increased carrier concentration). Auger electron spectroscopy (AES) [5] was carried out on the resistive element on the DI thermal tip (Figure 7-5) by Bridget Rogers of Motorola [6]. A 10 kV, 20 nA primary beam was used for the analysis after 1 kV Argon ions had been used to remove surface carbon. Measurements revealed the resistor composition to be 60% C, 35% Pt and 5% O. The excessive carbon content of the resistive element explains why the DI probe acts as a negative temperature coefficient resistor, and is probably also responsible for the high sensitivity of the probe. A draw back however to this method of resistor fabrication, where contamination determines the probe characteristics, is that contamination by its nature is unpredictable. Although not explored further, it is likely that reproducibility of calibration would be poor with DI probes.

The other difference between the DI and Glasgow probes was the magnitude of the temperature induced deflections of the probes. Comparison of the probes in the force-distance curves showed that the Glasgow probes were less prone to the large cantilever deflections observed with the DI probes. The DI probe suffered approximately 700 nm of bending when contact was lost on retraction, compared to approximately 35 nm for the side probe and 200 nm for the Bowtie probe. The reason for this would appear to be the difference in shape, composition and thickness of the metal coatings on the front faces of

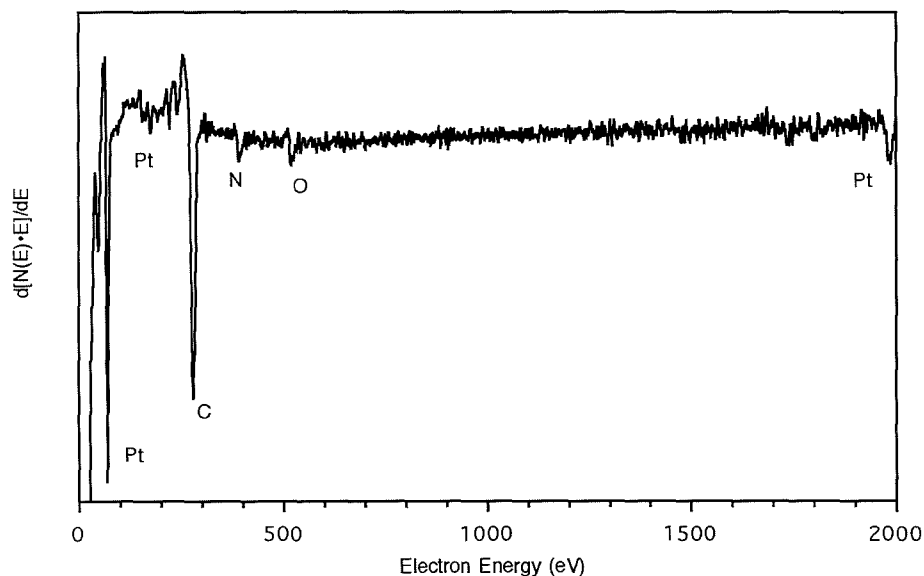


Figure 7-5 Scanning Auger spectrum of the material that formed the resistive element on the DI thermal tip. The composition was calculated to be 60% C, 35% Pt and 5% O (analysis performed by Bridget Rogers of Motorola).

the Glasgow probes, which reduces the heat absorbed by the laser and the bimaterial effect with the Si_3N_4 cantilever. Another factor that would reduced these effects is the tip radius of the different probes (which determines contact area). For example, the side probe has a nominal tip radius of 100 nm compared to approximately 500 nm for the DI tip. The Bowtie has a sensor dimension of approximately 150 nm but a tip radius of approximately 1.5 μm . Capillary forces may be significant with the Bowtie probe since it has a large flat contact area. The coverage and nature of the metal on the cantilever, which affects the heat absorbed by the probe from the laser, would appear to be a stronger influence however since the thermal deflections of the Bowtie are more than three times less than that of the DI probe. Yet another factor to be considered is the relative tip height of the probes. This determines the distance of the cantilever to the specimen at the point of contact, and is approximately 20 μm for the Glasgow probes compared to just under 4 μm for the DI tip. It has been shown that heat may be transferred to and from a cantilever through an air gap [7, 8]. Maximising this air gap reduces this effect and so a taller pyramid is preferable if cantilever-specimen interactions are to be minimised.

An advantage of the DI probe was that in comparison to the side and Bowtie probes, the signal levels were typically an order of magnitude greater. This was attributed to the larger series resistance and smaller contact area inherent in the Glasgow probe design (later improved using the enhanced sensitivity design - see Section 6.4). This was compensated for by increasing the gain of the thermal signal amplifier in the DI microscope electronics. The greater sensitivity of the DI probe is attributed to the material difference between the probes.

	DI Probe	Glasgow Side Resistor
Fabrication Method	FIB	EBL
Batch Size	1	60 or 240
Tip Radius	500 nm	100 nm
Tip Height	4 μm	20 μm
Sensor Material	Pt/C	Pd
Resistor Thickness	200-300 nm	50 nm
Resistor Size	1 μm x 5 μm	100 nm x 200 nm
Resistance	1-2 k Ω	1-2 k Ω

Figure 7-6 Table comparing the DI and Glasgow probes

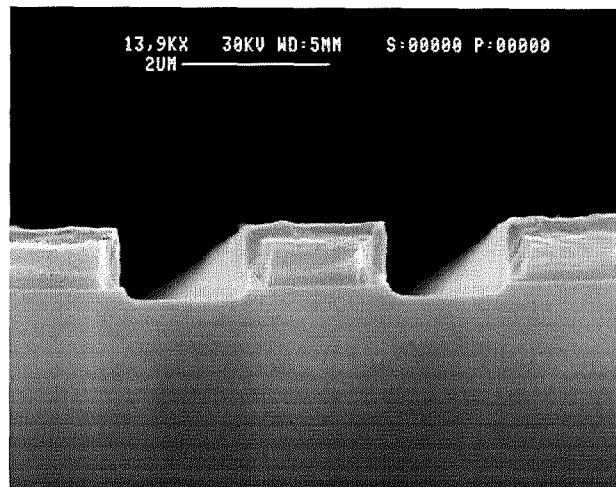


Figure 7-7 SEM cross section of passivated AlCu wires.

A summary of the differences between the side and DI probe is shown in Figure 7-6. The DI probe was used for most of the following experiments, however the side probe was also used at times to verify results and look for probe-specific artefacts.

7.5 Passivated Wires

Initial investigations with the DI thermal probe involved scanning some AlCu wires under 250 nm of passivation. Figure 7-7 shows a SEM cross section of the structure. The unheated wires were scanned normal to the direction of the wires. For analysis with the thermal tips, scan rates were low (0.2 Hz or below) in order to avoid tip damage and allow the feedback loop time to track the surface. Figure 7-8 shows four images scanned in different modes. Topographic analysis was performed using tapping and contact mode scanning with conventional probes (silicon and silicon nitride respectively). Thermal scanning, which yields a topographic image and a simultaneous thermal image, was performed using the DI thermal probe. Contact and tapping mode were used to verify the topography of the specimen, since it was shown earlier that temperature changes cause deflections in the thermal probe.

In both the tapping and contact mode images (Figure 7-8(a) and (b)), the surface roughness of the passivation covering the wires appears to be randomly oriented, however in the topography image with the thermal probe a large granularity is seen. This granularity is approximately 500 nm in size, which roughly matches the tip dimensions and so could be a repeated image of the tip shape. In the contact mode image and topography images using the thermal probe, the wires appear broadened compared to the tapping mode image. This is due to a larger tip opening angle which was measured by

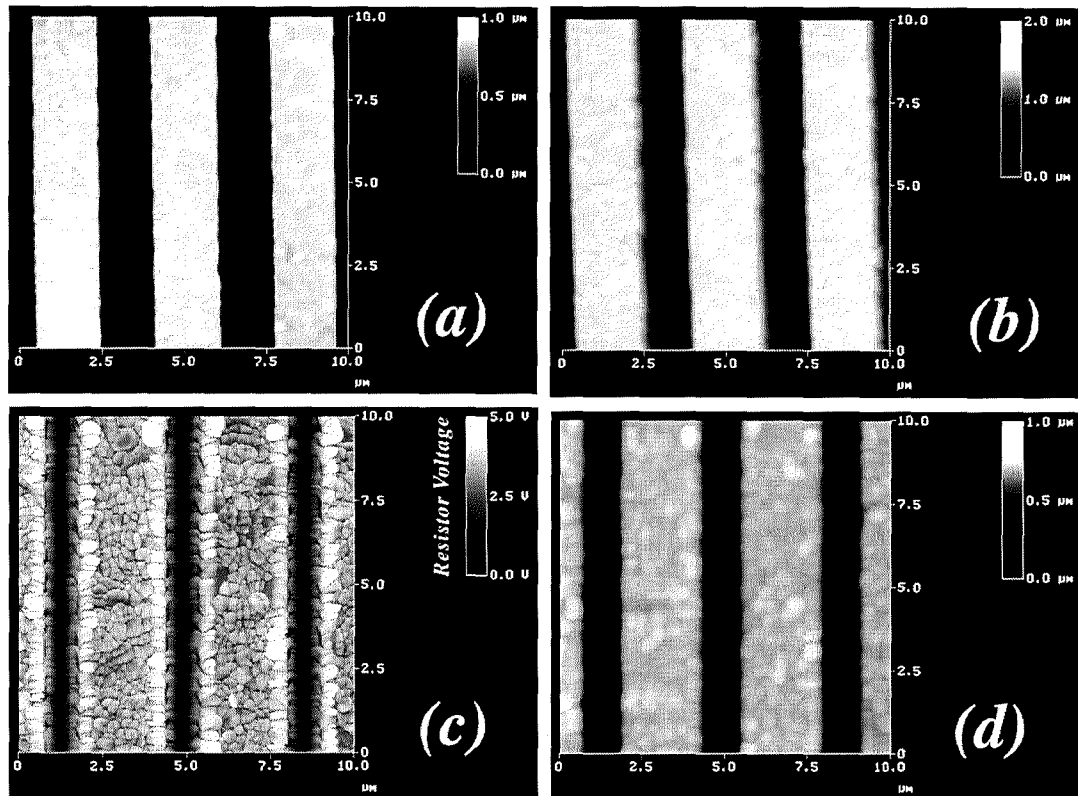


Figure 7-8 Passivated AlCu Wires (see Figure 7-7). (a) Tapping mode image using conventional silicon probe. (b) Contact mode image using conventional silicon nitride probe. (c) Heat flow image using DI thermal probe. (d) Topography image using DI thermal probe acquired simultaneously with (c).

looking at cross sections of the scans to be approximately 70 degrees for contact and 35 degrees for the tapping mode, which agrees with the manufacturer's specification for each probe.

The thermal image in Figure 7-8(c) is strikingly different from all the other images. Firstly, the edges of the wires appear brighter than the centre. This is explained by the tip-specimen contact area decreasing as the probe travels over an edge, producing an increase in probe temperature (see Figure 7-9). Secondly, there is a very high resolution granular structure in the body of the wires which is mirrored in part by the topography image using the thermal probe (Figure 7-8(d)). The origin of this contrast is thought to be due to surface roughness and differences in tip contact causing changes in heat transfer from tip to specimen. No such shapes are observed with the conventional tips however. Another hypothesis to explain this decoration of the passivated wires is that somehow the grain structure of the underlying metal is affecting the thermal tip. Perhaps differences in the thermal conductivity of different crystal orientations or even the roughness of the metal is being detected by the thermal probe.

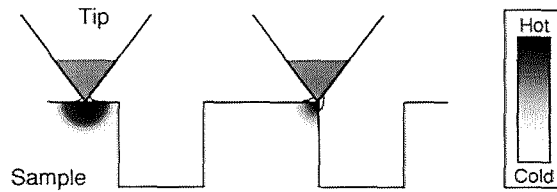


Figure 7-9 Tip losing heat over an edge. Note the representation of the water layer which is present on all surfaces at ambient.

To see if there was a correspondence between the grain size of the underlying AlCu and the features in the thermal image, a different part of the specimen containing a depassivated area of the same metal layer was scanned using tapping mode AFM (Figure 7-10 (a)). The granular thermal features in Figure 7-8(c) are approximately $0.5 \mu\text{m}$ in diameter. The roughness of this depassivated surface consists of larger features, also about $0.5 \mu\text{m}$ in size, which contain finer structure on the 100 nm scale. Whether this image clearly represents the Al grain size is unclear since post deposition processing can artificially roughen the surface. In order to observe the metal grains based on their crystal orientation therefore, a portion of the passivation on the original wires was removed using FIB milling. The FIB delineates the grains by etching different crystal orientations at different rates (due to channelling). Figure 7-10(b) shows an ion induced electron image from the FIB in which shows the grains after FIB milling. It is obvious from this image that the grain size is appreciably larger than the shapes seen in the thermal image. This image does not show all the grains since the angle of incidence of the milling beam was fixed, however

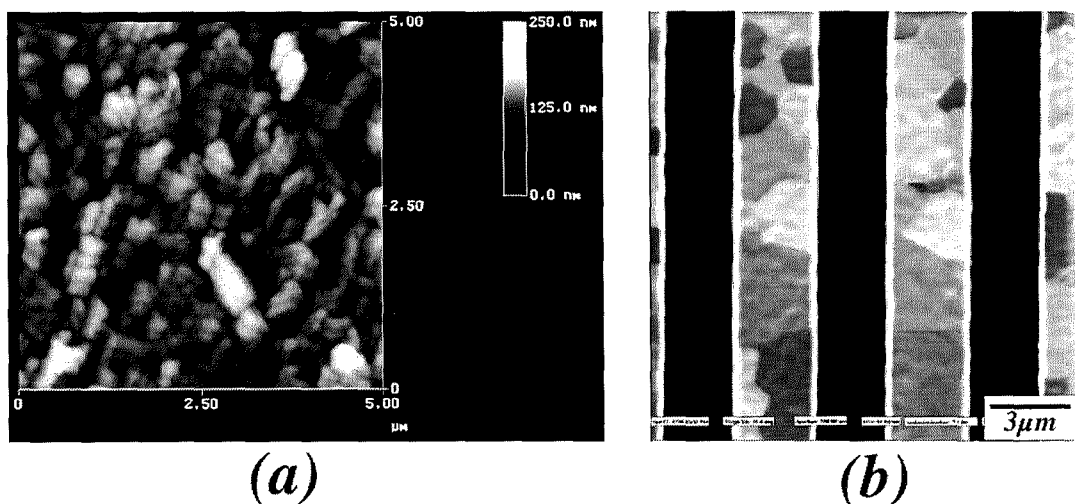


Figure 7-10 (a) Tapping mode image of unpassivated AlCu metal film. (b) FIB image of depassivated AlCu wires.

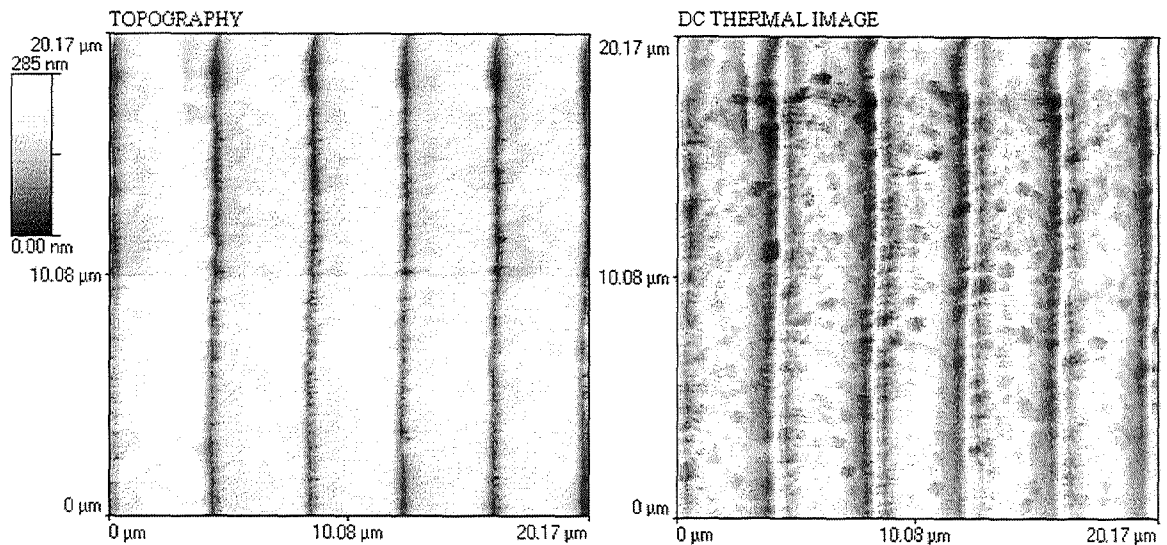


Figure 7-11 Topographic and thermal images of passivated AlCu wires using Wollaston wire probe (courtesy of Dr A. Hammiche).

even the smallest grains shown here are larger than the largest granular features in Figure 7-8(c).

Evidence to support the theory that the granular thermal features were caused by tip contact variations was provided when an identical specimen was analysed by H. M. Pollock and A. Hammiche at the University of Lancaster, England. The instrument used in this case was the SThM by *Topometrix*²⁶ which uses a Wollaston wire probe [9]. This design of probe differs from the DI probes in that it is made from a piece of 5 μm diameter platinum wire and as such has a large tip radius. The Topometrix thermal microscope provides the ability to modulate the electrical current, and therefore the heat produced in the probe. This can be used to limit the depth of the penetration heat [10] however for comparison with the DI probe only the dc component of the thermal image and the simultaneous topography are shown here (Figure 7-11). Images were taken of the passivated wire specimen using the Wollaston wire probe operated at 40 °C above room temperature. The wires appear broadened in the topographic image compared to Figure 7-8(d). This is attributed to the poorer specimen access afforded by the Wollaston wire. Some features approximately 1-2 μm in size can be seen in the body of the wires, presumably due to specimen roughness. The thermal image contains similar but sharper features although not at all like those seen with the DI thermal probe.

²⁶ Topometrix Corporation, 5403 Betsy Ross Drive, Santa Clara, CA 95054, USA.

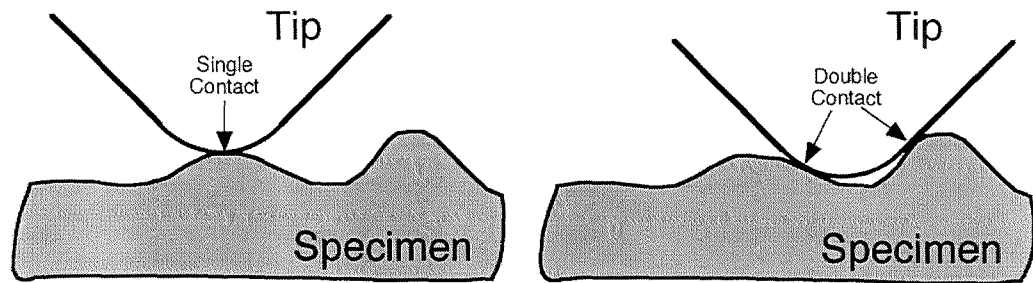


Figure 7-12 Representation of the way in which tip contact can change as topographic features are encountered.

The differences in the images taken with the DI thermal probe and the Wollaston wire probe suggest that tip contact changes are responsible for the thermal contrast in the Al wires. The DI probe with a tip diameter of $0.75\ \mu\text{m}$ gives thermal features of a similar size. This is also true of the Wollaston wire probe which gives thermal features of approximately $1\text{-}2\ \mu\text{m}$ with a tip radius of $3\text{-}5\ \mu\text{m}$. If the specimen roughness is assumed to be irregular based on the evidence of Figure 7-8(a), then the regularity observed in the images taken with the thermal probes is most likely caused by undesired interactions of the specimen with the large tip radii. A simple schematic of the way in which tip shape and surface roughness affect tip contact is shown in Figure 7-12. Single or double (or more) points of contact with the surface are possible which change the rate of heat transfer between tip and specimen. Topographic features may be traced by the tip creating lines of equal tip contact. The relatively blunt tip is thus imaged by asperities on the specimen, rather than the desired situation where a sharp probe faithfully records the specimen topology. The stronger contrast and higher resolution observed using the DI thermal probe compared to the Wollaston wire probe, is attributed to greater sensitivity and smaller tip radius.

7.6 FIB Trenches

Previous experience of co-workers at Motorola had shown the thermal probe to distinguish between height differences in a homogeneous specimen [11]. Ideally the probe would be sensitive to the thermal properties of the specimen only. To investigate this further, a sample was devised which consisted of variable depth trenches in $\langle 100 \rangle$ single crystal silicon.

The specimen was prepared by cleaving a piece of the polished silicon, and milling portions of it using an FIB. In an attempt to reduce any differences in the thermal

properties of the material due to ion implantation, an area ($100 \times 100 \mu\text{m}$) of the specimen surface was milled to implant gallium ions at a dose of approximately $5 \text{ nC}/\mu\text{m}^2$ over the whole of the working area. Three $5 \times 5 \mu\text{m}$ trenches were then milled at depths of 80 nm, 160 nm and 320 nm. Figure 7-13(a) is a topographic scan of the specimen using a conventional silicon tapping mode probe, and clearly shows the differences in trench depth. Figure 7-13(b) shows a thermal scan of the same area using a DI thermal probe. It can be seen that the probe temperature decreases with increasing trench depth. Similar enhancement of surface roughness to that in Figure 7-8(c) can be seen in this thermal image at the bottom of the trenches. This roughness is caused by the FIB milling which may mask surface contaminants or magnify imperfections in the original surface. Using conventional tapping mode AFM, the roughness at the bottom of the deepest trench was measured to be 7 nm (rms), compared to 0.15 nm (rms) for the unetched surface. In addition to the familiar enhancement of topographic features however it is clear that there is a trench depth dependence to the temperature signal. This was attributed to the proximity of the cantilever to the top surface since this would appear to be the only parameter that is changed between trenches. The temperature-distance curves for the DI probe confirm that the temperature of the probe drops as the cantilever approaches the specimen out of contact. A separate measurement [12] showed this transfer of heat from tip to specimen to occur over a range of $20 \mu\text{m}$ from the surface.

Figure 7-13(c) is a thermal image of the same specimen using a Glasgow side probe. It appears that this probe does not distinguish between the different trench depths to the same extent as the DI probe. The side probe does show a decrease in temperature with increasing trench depth like the DI probe, but the magnitude of this decrease is small in comparison. An indication of why this is the case may be seen in the force-distance curves in Figure 7-3. Some bending occurs in each of the cantilevers before contact with the specimen is made and corresponds to a drop in probe temperature. The heat loss and heat

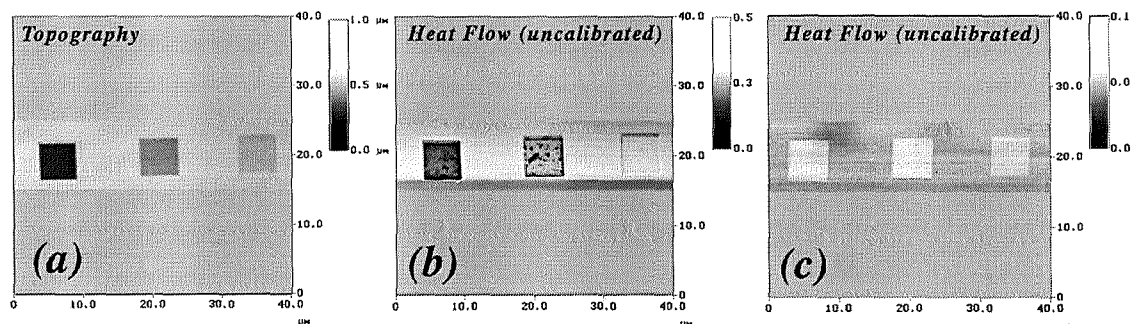


Figure 7-13 FIB Trenches in Silicon (a) Topographic image scanned in tapping mode using a conventional silicon probe. (b) Heat flow image using a DI thermal probe. (c) Heat flow image using a Glasgow side resistor probe.

induced bending is due to the presence of the specimen surface (gold for the Glasgow probes and silicon for the DI probe) and is presumably due to radiative or convective heat transfer from probe to specimen. Calculated values for the three graphs show that each probe deflects approximately 0.1 nm for a 1 nm decrease in tip-specimen spacing. It is clear however that the DI probe loses more heat, and deflects more than the Glasgow probes when near a surface since the silicon specimen used with the DI probe conducts heat less well than the gold used with the Glasgow probes. Other issues that affect this transfer of heat when the probe is out of contact are

- Magnitude of electrical heat produced at the tip.
- Absorption of the force sensing laser by the cantilever (optical heating).
- Distance of the cantilever from the specimen.
- Height and shape of the tip.
- The geometry of the resistive heater.
- Coverage and shape of metal layers on the cantilever.

Insufficient data was collected to determine which (if any) of these variables dominates, however one important characteristic is the tip height. The tip height effectively determines the distance of the cantilever from the specimen when in contact. The Glasgow probes have a tip height of 18-20 μm whereas the DI probe has a tip height of 4 μm . Therefore if the probe tip is a given distance from the specimen, the cantilever of the DI probe is always 14-16 μm closer to the specimen than that of the Glasgow probe.

7.7 Angle Cut Specimen

In order to chemically and electrically protect integrated circuits they are often coated with a thick dielectric layer. To investigate the sub-surface imaging capabilities of the microfabricated thermal probes through such passivating material (silicon oxide in this case), structures such as those shown in Figure 7-14 were imaged. The structures were designed to test electromigration effects in aluminium based wires, but also served as samples with thermal features passivated in such a way as to present a flat surface to the thermal probes. The wires were sandwiched between layers of silicon oxide, and the passivation was approximately 1.8 μm thick above the wires. In Figure 7-14(a) voids between the wires are seen. This is due to overhang of material during deposition which closes up the gap between the wires without filling it.

Although the structures were capable of electrical connection (the centre wire of the structure shown in Figure 7-14(a) was terminated in 100x100 μm pads), these experiments were conducted with the specimen unconnected.

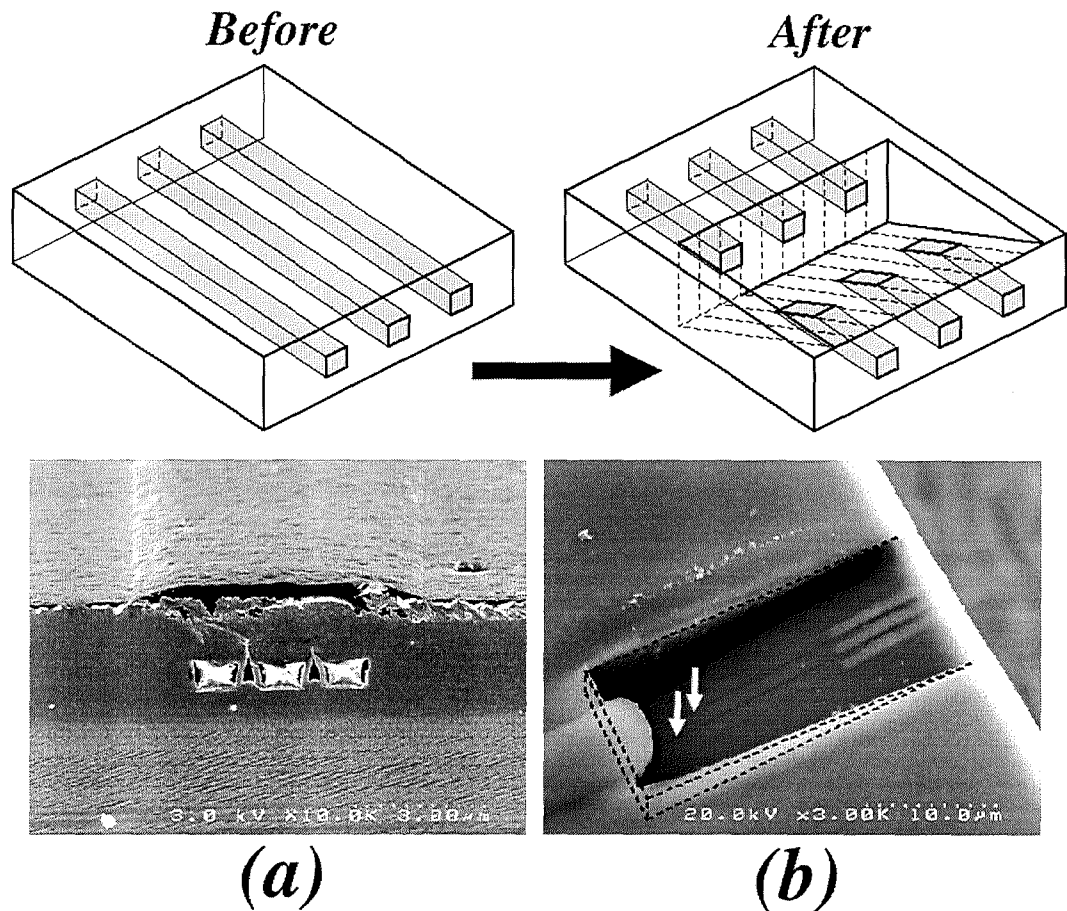


Figure 7-14 Electromigration Structures. (a) Schematic and SEM of three AlCuW wires buried under silicon oxide. (b) Schematic and SEM of the same specimen after an angular FIB cut made at 15° wrt to the surface plane.

Scans using the DI thermal tip on an unmodified specimen showed no evidence of the sub-surface features. The same high resolution tip effects observed in previous experiments were apparent, but no contrast relating to the three buried wires was seen. To thin the passivation, the specimen was placed in the FIB and trenches similar to those made in the silicon wafer were milled. The milling was timed to give a variety of depths, and although the mill rate was poorly controlled due to the heterogeneous nature of the passivation, a range of depths from $0.3 \mu\text{m}$ to $2 \mu\text{m}$ was achieved. Doses varied from 5 to $10 \text{ nC}/\mu\text{m}^2$. For passivation thicknesses above $0.1 \mu\text{m}$ no evidence of the sub-surface voids was seen. The images shown in Figure 7-15(a) and (b) were acquired at 100 nm . The topographic image shows the large ridge covering the wires and a large dimple, which is due to contamination or a defect accelerating the mill, but no other features. The thermal image on the other hand clearly shows the voids between the wires which appear as bright tramlines in the centre of the image (arrowed). The contrast is correct in that the tip

appears to be losing less heat over the voids, which are assumed to be air filled. This may be considered to be a sub-surface thermal image since features can be seen that correspond to known structures buried in the specimen. Furthermore there is no topographic evidence of these features.

It was difficult to time the milling to give a range of depths near to the $0.1\ \mu\text{m}$ thickness which would help pinpoint a maximum passivation thickness for detection of the sub-surface features therefore an alternative approach was used. An angular cut was made with the FIB down into the wires and through to the substrate below. Figure 7-14(b) shows an SEM micrograph and schematic drawing of the angle cut structure. By cutting at an angle, the scan surface was defined by the FIB side wall. The cut started at the top of the passivation and was angled down into the specimen. Had the cut been made the other way (starting at the wires and milling up at an angle) the voids and the metal wires would have caused non-uniform milling and a rough side wall. The side walls of an FIB cut are much less rough than at the bottom of a trench in general because the beam is tangential to the surface and gives a polishing effect. With trench cutting any surface debris or pits on the

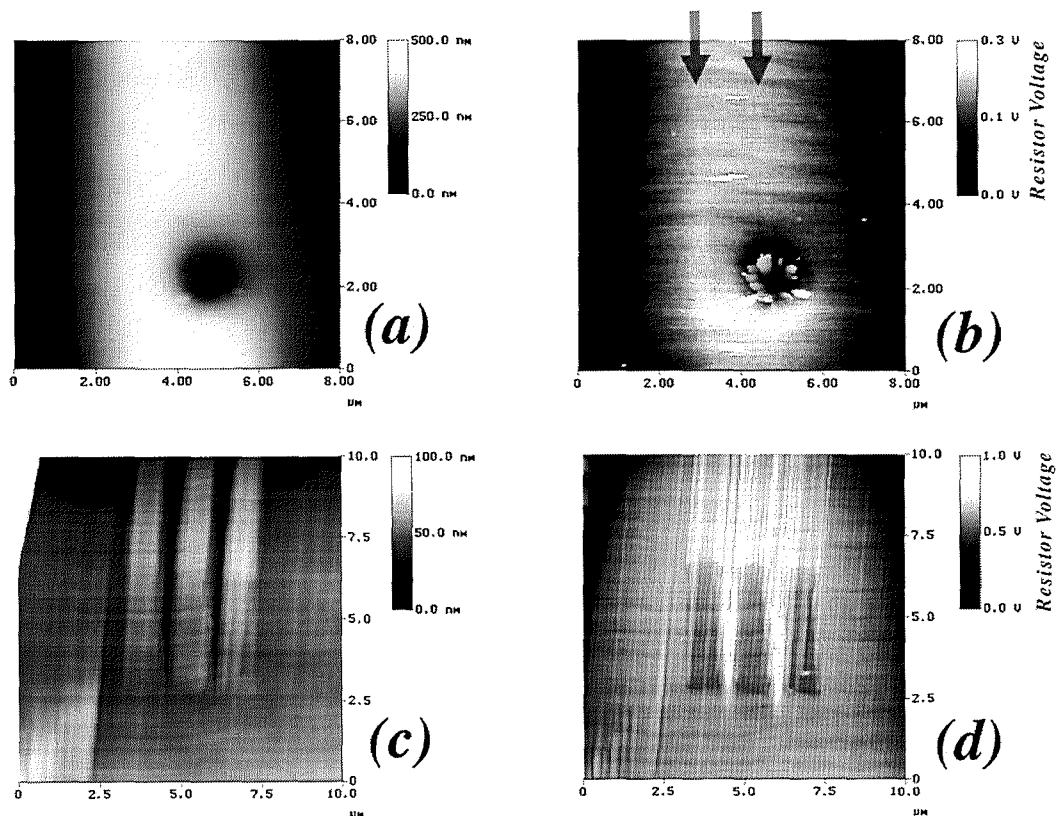


Figure 7-15 Sub-surface images using the DI probe. (a) Topography image of buried wire ($0.7\ \mu\text{m}$ passivation thickness). (b) Corresponding heat flow image. Voids between wires are arrowed. (c) Topographic image of angle cut passivated wires. (d) Corresponding heat flow image.

original surface are amplified down onto the final surface. An FIB sidewall may be incrementally polished by repeated milling with finer spots, but this was not possible here due to time constraints.

The finished specimen presented a continuum of passivation thickness from 1.8 μm down to the bare metal wires, followed by a section down through the wires and beyond. Scans of this surface using a DI thermal tip are shown in Figure 7-15(c) and (d). The passivation thickness is greatest at the bottom of the images. The topographic image shows two large trenches which were caused when the voids were breached and are arrowed in Figure 7-14(b). The thermal image clearly shows the thermal conductivity difference between the aluminium wires (the three dark stripes) and the passivation. The corrugation which can be seen in both topographic and thermal images is caused by the FIB raster scan (spot size was 0.1 μm) and was measured to be 1 nm p-p using tapping mode AFM with conventional silicon probes.

Areas of interest in the thermal image were the two white tails protruding from the three stripes (which represent the metal wires). These are caused by the voids between the wires which alter the effective thermal conductivity of the specimen. If the voltage across the probe in air (far away from the specimen) is offset to be zero, the relative voltages when contacted to the passivated voids, SiO_2 and metal wires were measured to be 25 mV, 100 mV and 135 mV respectively. Roughly twice the contrast is thus produced by the sub-surface feature compared with the Al relative to the SiO_2 . This explains why the voids can be seen in Figure 7-15(b) at a depth of 100 nm without evidence of the metal lines. From the known angle of the cut (15°) and the measured lateral extent of the thermal features corresponding to the voids (light streaks), the maximum depth for resolution of the voids was calculated to be 225 nm (± 25 nm), at which point the contrast due to the sub-surface

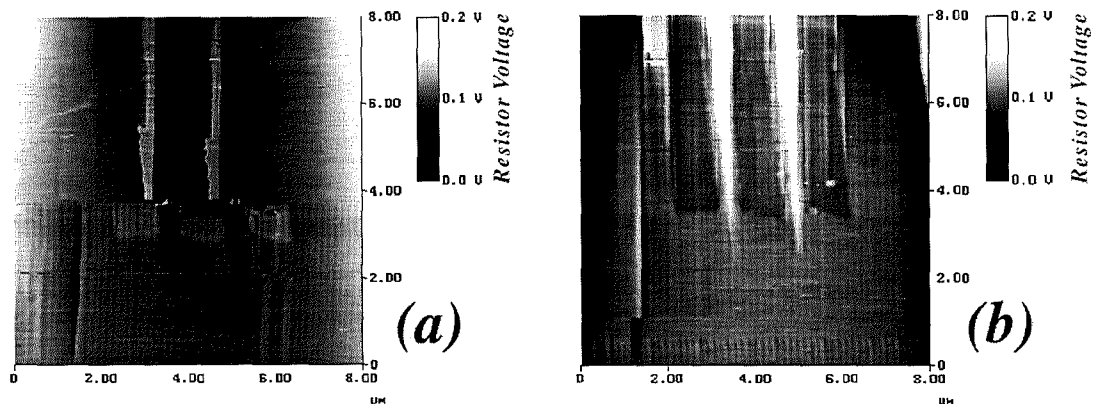


Figure 7-16 Side resistor images of angle cut passivated wires. (a) Heat flow image with shroud collapse mid scan. (b) Complete heat flow image post collapse (contrast reversed).

voids was equal to that due to the residual topographic corrugation.

A side resistor probe was used to scan the same specimen. Unfortunately the only side probes available during this experiment were those which had been poorly etched and featured a silicon nitride and metal shroud round the tip apex (see Section 6.5). Initial thermal images were of variable quality which was attributed to the shroud causing poor thermal contact with the specimen. Figure 7-16(a) shows what is thought to be the fragile shroud collapsing part way through a scan due to tip wear, thus allowing the real tip and sensor to image the specimen. The image switches suddenly to give a clearer image of the wires and voids that corresponds well to the image taken with the DI tip. Figure 7-16(b) shows a complete scan after the shroud has disappeared. The contrast in this image has been artificially reversed for comparison with the image using the DI tip (Figure 7-15(d)). Note that despite the normalisation of the different probe sensitivities using heat from the force sensing laser, the full scale voltage in the DI probe image is five times greater than that of the side probe. This is attributed to the material difference between resistors and the inherently poorer thermal contact afforded by the sharper side probe. Despite this, the signal to noise was measured from the images to be 18.5 dB for the DI probe and 27 dB for the side probe. The lower noise in the side probe is attributed to the purity of the Pd resistor relative to the carbon contaminated DI resistor.

- [1] A. P. Whitehead, P. K. Footner, and B. P. Richards, "ESD-Induced Electromigration; A new VLSI failure mechanism.," *Proc. ISTFA*, pp. 214-220, 1984.
- [2] G. Binnig and D. P. E. Smith, "Single-tube 3-dimensional scanner for scanning tunneling microscopy," *Review Of Scientific Instruments*, vol. 57, pp. 1688-1689, 1986.
- [3] *Scanning probe microscopy and spectroscopy*: Cambridge University Press, 1994.
- [4] L. Johnson, *Motorola MRST*, Private communication 1998, rpo6760@email.sps.mot.com.
- [5] S. M. Sze, *VLSI Technology*: McGraw Hill, 1988.
- [6] G. Mills, J. M. R. Weaver, G. Harris, W. Chen, J. Carrejo, B. Johnson, and B. Rogers, "Detection of sub-surface voids using scanning thermal microscopy," *Ultramicroscopy*, vol. 80, pp. 7-11, 1999.
- [7] O. Nakabeppu, M. Chandrachood, Y. Wu, J. Lai, and A. Majumdar, "Scanning thermal imaging microscopy using composite cantilever probes," *Applied Physics Letters*, vol. 66, pp. 694-696, 1995.
- [8] H. Pollock, *University of Lancaster*, Private communication 1998, h.pollock@lancaster.ac.uk.
- [9] A. Hammiche, M. Reading, H. M. Pollock, M. Song, and D. J. Hourston, "Localized thermal analysis using a miniaturized resistive probe," *Review Of Scientific Instruments*, vol. 67, pp. 4268-4274, 1996.

- [10] A. Hammiche, D. J. Hourston, H. M. Pollock, M. Reading, and M. Song, "Scanning thermal microscopy - subsurface imaging, thermal mapping of polymer blends, and localized calorimetry," *Journal Of Vacuum Science & Technology B*, vol. 14, pp. 1486-1491, 1996.
- [11] W. Chen, *Motorola SPS*, Private communication 1997, rp2312@email.sps.mot.com.
- [12] K. Kjoller, *Digital Instruments Corp*, Private Communication 1997, kevin@di.com.

8 Conclusions

8.1 Probe Fabrication

It has been shown that a variety of novel probes for scanning thermal microscopy may be batch fabricated using nanolithography and micromachining [1-3]. Figure 8-1 shows a table of the probes that have fabricated by the author. The probes may be split into two distinct types: Au/Pd thermocouples and Pd resistance thermometer/heaters. Both have been demonstrated with truncated pyramid and sharp triangular tips. Figure 8-2 shows a schematic of the different tip shapes which have complimentary advantages. The truncated pyramid offers good thermal contact of the sensor to relatively flat specimens. For specimens with significant relief however, the large tip size means that the sensor may


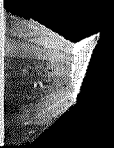




Probe Type	Picture of Probe	Description of Probe	Sensor Size	Good Access	Good Thermalisation	Quantitative Thermometry	Heat Specimen
Cross Thermocouple		Bisecting Au/Pd thermocouple on flat apexed tip.	100nm ² (typ) 35nm ² (min)		✓	✓	
Side Thermocouple		Diamond shaped thermocouple on a sharp triangular cantilever.	250nm ² (typ) 100nm ² (min)	✓		✓	
Triple Thermocouple		Three Pd wires bisecting a long common Au wire on flat apexed tip.	120nm ² (typ) 70nm ² (min)		✓	✓	
Swiss Cheese Thermocouple		Side thermocouple with the shape of the thermocouple constrained in 2D.	200nm ² (typ) 70nm ² (min)	✓		✓	
Bowtie Resistor		Single two terminal Pd wire forming a taper on a flat apexed tip.	150nm ² (typ) 70nm ² (min)		✓		✓
Side Resistor		Self aligned resistor on a sharp triangular tip.	150nm ² (typ) 100nm ² (min)	✓			✓

Figure 8-1 Table of thermal probes fabricated using the generic Glasgow substrate.

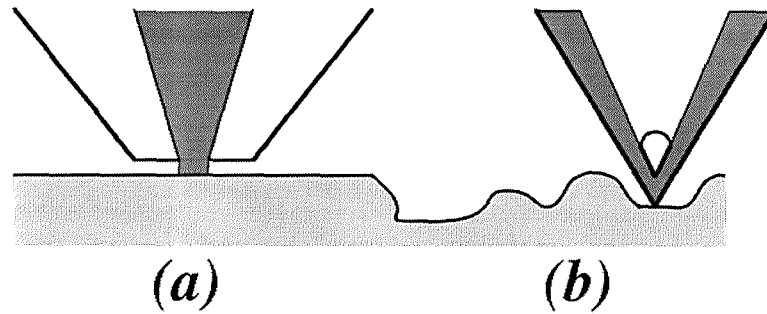


Figure 8-2 Different specimen access and sensor contact area with (a) the truncated pyramid and (b) sharp triangular tip.

intermittently lose contact resulting in errors in the thermal data. In contrast, the sharp triangular tip gives better specimen access, but only a small portion of the sensor at the tip apex is in contact with the specimen. Although not yet properly characterised, this is expected to degrade the thermal signal to noise ratio and thermalisation time constant.

The thermocouple and resistance thermometer/heater probes differ significantly. Thermocouples are capable of quantitative thermometry, and this is a desirable function for a microscope probe to have. It has been shown that the Seebeck coefficient for the thin film Au/Pd thermocouples used here are the same as bulk Au/Pd thermocouples to within a factor two and matched to 3% on a probe. The thermocouple probes have also been shown to produce temperature maps of a photothermal test specimen when scanned in a conventional AFM.

The resistance thermometer/heater probes may be used in many different modes, some of which have been presented here. Thermal conductivity imaging and thermomechanical thermal analysis of polymers has been demonstrated in collaboration with Lancaster University. Subsurface imaging has been also been performed using the side resistor probe in a commercial microscope and a specimen with buried thermal features.

Some novel designs and processes for making AFM cantilevers and sensors have been developed including selective removal of parts of the cantilever to provide self alignment of the thermal sensor to the tip. Multiple sensors have also been fabricated on a single tip, which demonstrates that complex patterns may be patterned on three dimensional substrates. The multiple sensor tips may have utility in their own right for measuring tip contact effects or high speed scanning. The limits of electron beam lithography and metal lift off on the generic pyramidal AFM tips has also been explored. Wires 35 nm wide have been patterned at the apices of the 20 μm high tips. The limiting factor would appear to be the resist coating on the tip which must be thick enough to cover sharp edges yet thin

enough to allow small features to be patterned. The extent and shape of the metal features at the tip that form the thermal sensors have been varied, and were found to affect the bending of the AFM cantilevers and sensitivity of the thermometers. In addition to this, advances in transferring metal patterns onto three dimensional substrates have been made. The employment of “lift-off aids”, where redundant space is patterned in such a way as to free excess metal from critical features, has been shown to be invaluable in producing sensors with high yield.

8.2 Measurements

It is fair to say that the work presented here has not only advanced the field of scanning thermal microscopy in terms of probe development, but also in the measurement of thermal phenomena. Some of the highest resolution thermal images ever obtained have been produced using the improved access thermocouple probes. The contrast was due to changes in heat transfer between tip and a photothermal test specimen, and a resolution of 40 nm was observed. In addition to this, the temperature dependence of 70 nm thermocouples on the triple thermocouple probes has been measured, although not calibrated.

Much pioneering work has also been done in collaboration with Lancaster University. High resolution thermal conductivity and thermal expansion images of polymer specimens have been demonstrated using the Bowtie probes. Thermomechanical point measurements have been made and phase changes in selected polymers observed. Resolutions of 100-200 nm have been achieved, and glass transitions and melting events have been identified. Calorimetric measurements, where the heating of the probe is modulated, have just recently been acquired [4]. Work continues at Lancaster to discover more about the contrast mechanisms involved, and to apply the probe techniques to new fields of measurement.

In conjunction with testing of the new micromachined probes at Glasgow and Lancaster, a body of work has been accumulated using both Glasgow and commercial probes in a commercial microscope. This work was carried out at Motorola - the CASE collaborator for this project. The dependence of cantilever bending on specimen temperature while in close proximity to the specimen, and at the point of contact, were studied. Tip contact area variations and parasitic heat transfer to the specimen through the cantilever were identified as significant contributors of artificial contrast. Due to the Glasgow probes having smaller tip radii, taller tips, and less metal on the cantilever, the magnitudes of these deleterious effects were shown to be significantly smaller than with the commercial probes. Sub-surface detection of voids in multiple layer electromigration test structures was also achieved using thermal conductivity imaging. Angled sectioning of the structures was then

used to determine that the maximum depth of penetration was over 200 nm under normal operating conditions.

8.3 Artefacts

There would appear to be three main causes of artefactual contrast in scanning thermal microscopy.

- Tip-specimen contact area effects.
- Short range temperature induced bending of the cantilever due to contact with specimen.
- Long range bending of the cantilever and distortion of thermal information due to radiative and convective heat transfer from the cantilever its environment.

The most common and misleading artefact is caused by variations in tip to specimen contact area. Strong thermal contrast corresponding solely to topographic changes in the specimen has been observed in almost all of the thermal images produced during this project, often obscuring temperature or thermal conductivity contrast. The effect is dependent on sensor size, tip radius, and specimen roughness, and was seen using DI, Glasgow and Wollaston wire probes to varying degrees. Ideally, specimens analysed by SThM would be perfectly flat in order to eliminate the tip effects, however in practice no specimens have yet met this criterion. Specimen preparation (FIB milling, chemical etching, mechanical cleaving and polishing) can help to planarise surfaces of interest, however this can be time consuming and in most cases the original thermal properties of the specimen are expected to be drastically altered.

What is important is that the tip radius and sensor dimensions be shrunk to approximately an order of magnitude less than the specimen micro-roughness. Undulations on the

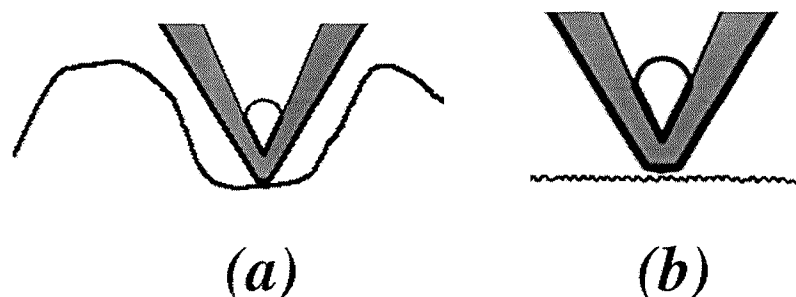


Figure 8-3 (a) The specimen may be faithfully traced by the tip if the roughness is (a) larger than the tip radius and tip opening angle or (b) much less than the tip radius.

surface should then be well resolved by the AFM, and contact with the specimen maintained at the end of the tip. Alternatively, destructive artefacts from roughness may be avoided if the tip is approximately an order of magnitude larger than the specimen micro-roughness. The specimen roughness may then cause high frequency spatial noise in the thermal image, but thermal features of similar size to the tip will be resolved. In both cases, shown diagrammatically in Figure 8-3, the tip must have an appropriate opening angle to preserve tip contact during larger scale topographic variations. This allows the specimen to be faithfully traced by the tip and artefacts caused by bridging of valleys to be significantly reduced.

The specimens used during this investigation can be split into two broad categories: semiconductor structures and polymers. In order to determine whether SThM will become an important analysis tool in these areas, it is useful to look at typical specimens and the type of measurements that are most desirable. In the case of the semiconductor industry, a key application area is measurement of the power dissipation of the millions of transistors found on modern microprocessors. Finished die usually have large topographic variations due the thick contact layers and many microns of passivation deposited over the whole die. It is important that these structures are altered as little as possible if heat dissipation in active devices is to be investigated. Stripping away any of the layers to provide better access for the probe will drastically alter the heat flow away from the active region. Without the removal of passivation however, high resolution imaging is not possible since any heat produced spreads out laterally through the dielectric. Cross sectioning devices and at the same time preserving electrical operation is extremely difficult, and again does not provide a good representation of normal operating conditions. Perhaps SThM has a role in semiconductor material science, but in the opinion of the author it will not become widespread for routine measurements or failure analysis.

Polymer specimens on the other hand often present a more amenable surface for SThM. Bulk material is often analysed and so polishing or microtoming does not necessarily change the specimen properties. Polymer specimens also seldom feature active components (although new conducting polymers are becoming more widespread [5]), and so coating with dielectrics is not necessary. Multi-phase polymers may be spun onto flat substrates and SThM used to visualise the domain structure. In this case the specimen is almost flat and so the resolution limits of SThM may be explored with minimal topographic artefacts. Local thermal analysis adds an extra dimension to SThM in that it allows identification of the materials in an image (providing the glass transition or melting point of the material are within the temperature range of the probe). Most traditional calorimetric techniques are available using SThM but on the micron scale. The new probes described here are expected to push the resolution limits and analysis volumes of these

techniques towards 100 nm. This increase in resolution and decrease in analysis volume is of interest to industry because polymer structure is often not adequately resolved using existing probes.

8.4 Future Work

Much remains to be done in the field of scanning thermal microscopy and thermal probe development and characterisation. The construction of several different probe types has been demonstrated, however due to time constraints they have not been exhaustively characterised. In particular, there remains much to be done with the thermocouple probes. It is desirable to be able to perform properly calibrated thermal measurements as opposed to qualitative thermal imaging. Determination of actual temperatures on the micro and nano-scale using nano-thermocouples provides the opportunity to study discrete constituents of structures and materials using traditional thermometry. It is important therefore that future work includes accurate measurement of the thermoelectric properties of such thin film thermocouples.

Further characterisation of the resistor probes is also important. Of particular interest are high speed versions of existing techniques, accurate measurement of local thermal conductivity [6, 7], and advanced local thermal analysis of polymers [8]. This work is currently being pursued in collaboration with Lancaster and Sheffield Universities, and the National Physical Laboratory.

With a more thorough understanding of the thermal probes described in this text comes the ability to apply thermal microscopy to new fields of exploration. Potential measurements for the near future include analysis of thermally induced defects in laser diode facets, high resolution photothermal FTIR [9], nanotribology, determination of the thermal conductivity of thin or doped layers of semiconducting material and nanolithography using chemically amplified resists.

Further still in the future is the fabrication of entirely new probe types. A toolbox of techniques for patterning thermal sensors and related structures has been provided here, and may now be used to make more complex cantilever and sensor arrangements. Multiple identical sensors on one tip have been demonstrated, however new probes could incorporate different sensors on a single tip. An obvious extension would also be the combination of a resistive heater and a thermocouple, finding application in the simultaneous stimulation and measurement of a specimen. Figure 8-4(a) shows a possible arrangement for such a probe. Alternatively the thermal sensors may be combined with magnetic or near-field optical sensors with possible applications in storage or

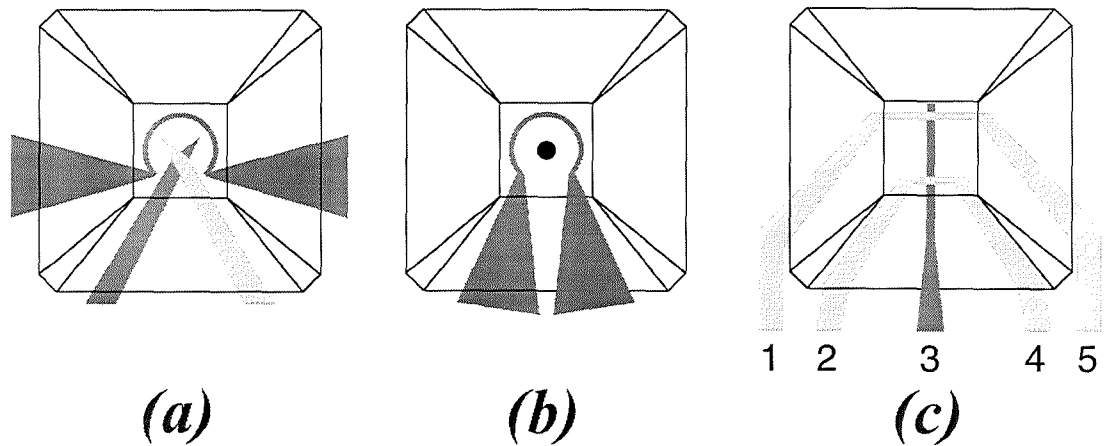


Figure 8-4 New complex sensor designs: (a) Thermocouple with integrated ring heater. (b) Coil for thermal or magnetic perturbations with integrated near-field optical sensor. (c) Self calibrating probe for absolute temperature measurements. Terminal 1&2 and 4&5 are gold. Terminal 3 is nichrome.

nanolithography. Figure 8-4(b) shows a two terminal metal structure combined with a near field aperture. In this case, the SNOM cladding would have to be isolated from the metal ring so as not to cause a short circuit. Some form of dielectric spacer layer may have to be introduced. Figure 8-4(c) shows a probe design for a self calibrating dual thermocouple probe which could be used for absolute temperature measurements. This arrangement consists of two Au/NiCr thermocouples at the flat apex of a pyramidal tip. The thermocouples may be calibrated by first performing a four terminal resistance measurement of the portion of the NiCr between the two Au wires (terminals 1&2 drive current, terminals 4&5 measure voltage). The Johnson noise, e_n , is then measured between terminals 1&2 or 4&5 using two independent low current noise operational amplifiers and a correlator used to extract the common mode noise due to the resistor from the amplifier noise. Johnson noise is defined as

$$e_n = \sqrt{4k_B TBR}$$

Since e_n and the resistance R of the NiCr resistor are known, absolute temperature T may be calculated by inserting Boltzmann's constant k_B and the bandwidth B over which the Johnson noise measurement was performed. Once T at the tip apex is known the thermocouples can be properly calibrated.

Other possibilities include the advancement of the improved access probe technology in which parts of the cantilever are removed to create novel tip shapes or self alignment of the sensor layers. The pyramidal tip is essentially a blank canvas out of which shapes may be

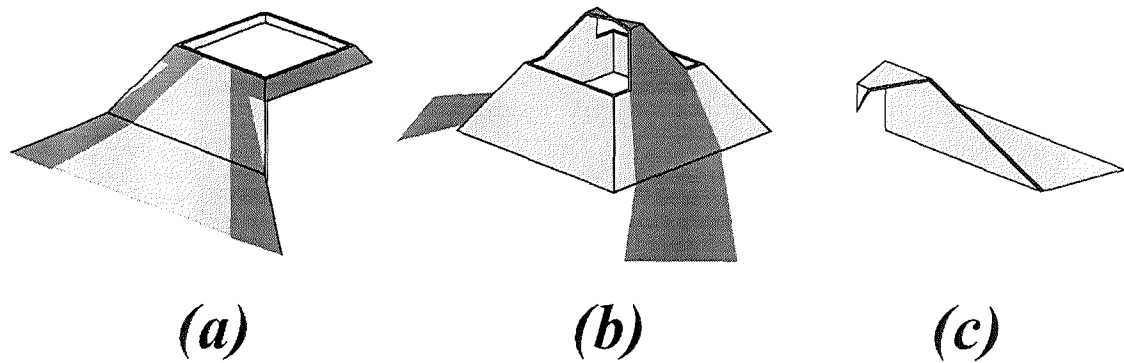


Figure 8-5 Possible future probe designs involving cutting shapes out of the cantilever. (a) A self aligned coil. (b) A self aligned Bowtie probe. (c) Hook probe.

cut (assuming they can be patterned using EBL and lift off). Self aligned rings for bulk magnetic or thermal manipulation of specimens could be manufactured (see Figure 8-5(a)). Figure 8-5(b) shows a self aligned Bowtie probe which would provide better specimen access in one dimension and a reduction in the thermal path from heater to cantilever. Figure 8-5(c) shows a hooked probe which has possible utility in manipulating specimens mechanically. Perhaps AFM of the underside of overhanging structures (resist profiles for example) would be possible with such a probe.

Summarising, future work using the micromachined thermal probes may be split into three broad categories: further characterisation of existing probes, application of the probes to new areas of microscopy and measurement, and fabrication of complex new probes which may be tailored to suit wide variety of applications and experiments.

- [1] H. Zhou, A. Midha, G. Mills, S. Thoms, S. K. Murad, and J. M. R. Weaver, "Generic scanned-probe microscope sensors by combined micromachining and electron-beam lithography," *Journal Of Vacuum Science & Technology B*, vol. 16, pp. 54-58, 1998.
- [2] G. Mills, H. Zhou, L. Donaldson, and J. M. R. Weaver, "Scanning thermal microscopy using batch fabricated thermocouple probes," *Applied Physics Letters*, vol. 72, pp. 2900-2902, 1998.
- [3] H. Zhou, G. Mills, B. K. Chong, A. Midha, L. Donaldson, and J. M. R. Weaver, "Recent progress in the functionalization of atomic force microscope probes using electron-beam nanolithography," *Journal of Vacuum Science & Technology a-Vacuum Surfaces and Films*, vol. 17, pp. 2233-2239, 1999.
- [4] A. Hammiche, *University of Lancaster*, Private communication 1999, a.hammiche@lancaster.ac.uk.
- [5] D. R. Baigent, R. N. Marks, N. C. Greenham, R. H. Friend, S. C. Moratti, and A. B. Holmes, "Conjugated polymer light emitting diodes on silicon substrates," *Applied Physics Letters*, vol. 65, pp. 2636-2638, 1994.

- [6] F. Ruiz, W. D. Sun, F. H. Pollak, and C. Venkatraman, "Determination of the thermal conductivity of diamond-like nanocomposite films using a scanning thermal microscope," *Applied Physics Letters*, vol. 73, pp. 1802-1804, 1998.
- [7] V. M. Asnin, F. H. Pollak, J. Ramer, M. Schurman, and I. Ferguson, "High spatial resolution thermal conductivity of lateral epitaxial overgrown GaN/sapphire (0001) using a scanning thermal microscope.," *Applied Physics Letters*, vol. 75, pp. 1240-1242, 1999.
- [8] M. Reading, D. J. Hourston, M. Song, H. M. Pollock, and A. Hammiche, "Thermal analysis for the 21st century," *American Laboratory*, vol. 30, pp. 13, 1998.
- [9] A. Hammiche, H. M. Pollock, M. Reading, M. Claybourn, P. H. Turner, and K. Jewkes, "Photothermal FT-IR spectroscopy: A step towards FT-IR microscopy at a resolution better than the diffraction limit," *Applied Spectroscopy*, vol. 53, pp. 810-815, 1999.

9 Publications

(Prints of the two first author papers follow on next page)

(A) **G. Mills**, H. Zhou, L. Donaldson, and J. M. R. Weaver, "Scanning thermal microscopy using batch fabricated thermocouple probes," *Applied Physics Letters*, vol. 72, pp. 2900-2902, 1998.

(B) **G. Mills**, J. M. R. Weaver, G. Harris, W. Chen, J. Carrejo, B. Johnson, and B. Rogers, "Detection of sub-surface voids using scanning thermal microscopy," *Ultramicroscopy*, vol. 80, pp. 7-11, 1999.

H. Zhou, A. Midha, **G. Mills**, S. Thoms, S. K. Murad, and J. M. R. Weaver, "Generic scanned-probe microscope sensors by combined micromachining and electron-beam lithography," *Journal Of Vacuum Science & Technology B*, vol. 16, pp. 54-58, 1998.

H. Zhou, **G. Mills**, B. K. Chong, A. Midha, L. Donaldson, and J. M. R. Weaver, "Recent progress in the functionalization of atomic force microscope probes using electron-beam nanolithography," *Journal of Vacuum Science & Technology a-Vacuum Surfaces and Films*, vol. 17, pp. 2233-2239, 1999.

H. Zhou, A. Midha, L. Bruchhaus, **G. Mills**, L. Donaldson, and J. M. R. Weaver, "Novel SNOM/AFM probes by combined micromachining and electron beam nanolithography," *Journal of Vacuum Science and Technology B*, 1999 (accepted).

H. Zhou, A. Midha, **G. Mills**, L. Donaldson, and J. M. R. Weaver, "Scanning near field optical spectroscopy and imaging using nanofabricated probes," *Applied Physics Letters*, 1999 (accepted).

(A)

APPLIED PHYSICS LETTERS

VOLUME 72, NUMBER 22

1 JUNE 1998

Scanning thermal microscopy using batch fabricated thermocouple probes

G. Mills, H. Zhou, A. Midha, L. Donaldson, and J. M. R. Weaver^{a)}*Department of Electronics and Electrical Engineering, University of Glasgow, Glasgow G12 8LT, Scotland, United Kingdom*

(Received 20 January 1998; accepted for publication 26 March 1998)

We have developed scanning thermal microscopy probes for high resolution analysis of thermal properties in an atomic force microscope (AFM). Electron beam lithography and silicon micromachining have been used to batch fabricate Au/Pd thermocouples situated at the end of Si_3N_4 cantilevers. The cantilevers are patterned on the side of traditional style pyramidal AFM tips, giving a new shape of probe which is favorable for access to specimens containing significant topographic variation. Tip radius is approximately 50 nm and the probe has a macroscopic opening angle of 70° . The probes were scanned in the repulsive mode using a conventional AFM. Force feedback was optically employed to give topographic and thermal maps simultaneously by maintaining a constant force of approximately 5 nN. During initial scans using a photothermal test specimen, 80 nm period metal gratings were thermally resolved. © 1998 American Institute of Physics. [S0003-6951(98)01322-9]

Scanning thermal microscopy (SThM) is related to atomic force microscopy (AFM)¹ in which a sharp tip mounted on a cantilever is held in contact with a specimen and mechanically scanned over the surface. Cantilever deflections are optically detected and used to regulate the force of contact, and to provide topographic information about the specimen. If a thermal sensor is placed at the end of the tip, a simultaneous local temperature map can then be acquired. Early instruments for SThM used thermal conduction to profile specimens in much the same way as scanning tunneling microscopy (STM) uses tunneling current.² Combined STM/SThM instruments have also been used for temperature mapping^{3,4} where a thermal sensor is used as both a tunneling source and a temperature detector, however such instruments are limited to conducting specimens only. Using the AFM for SThM allows a greater number of practical specimens to be imaged however because the specimens need not be conductors.

Probe designs for SThM have matured steadily over the last five years but have mostly involved individually crafted cantilevers and sensors. Techniques have included the use of resistance thermometers,⁵ twisted and chemically etched wire thermocouples,⁶ diamond shards,⁷ and bimetallic cantilevers.⁸ Since the probes are made one at a time, however, any two sensors will necessarily be different, leading to the need for individual characterization of each probe before use. In addition to this, fabrication of the probes is time consuming and dependant on chance and human dexterity. In general, there is a need for well characterized probes that are batch fabricated. Such probes would provide a user with continuity between experiments and certainty about the dimensional and electrical properties of the sensors.

In this letter we present results achieved using batch fabricated Au/Pd thermocouple⁹ probes. The probes are novel in that they are produced using micromachining of bulk silicon

and multiple levels of direct write electron beam lithography (EBL).

The substrate for the probes was formed by micromachining a Si wafer using Si_3N_4 as a mask for wet etching with an anisotropic etchant (KOH and KOH+Isopropyl Alcohol). Probe bases and etched through markers were formed on one side of the wafer using contact photolithography, liftoff,¹⁰ and reactive ion etching (RIE) for pattern transfer, and KOH etching, leaving a 60 μm thick silicon membrane below the position of the silicon nitride AFM cantilever. The reverse side of the wafer was then patterned with EBL (using the etched through markers for automatic alignment) and etched to form pyramidal tips, each with local alignment marks. A detailed account of these processes is published elsewhere.^{11,12}

The substrate was then coated with 500 nm of low pressure chemical vapor deposited (LPCVD) Si_3N_4 and, after another level of EBL was transferred into a Cr mask, reactive ion etched with C_2F_6 to form the cantilever. The cantilever shape is triangular and impinges upon the protruding pyramidal tip to form an asperity angled away from the substrate plane at 56° . The vertical dry etching profiles produce a

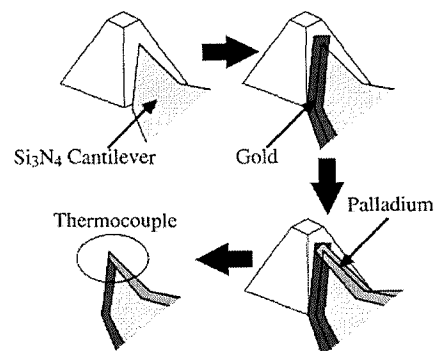


FIG. 1. Fabrication stages of the thermocouple probe process.

^{a)}To whom all correspondence should be sent. Electronic mail: j.weaver@elec.gla.ac.uk

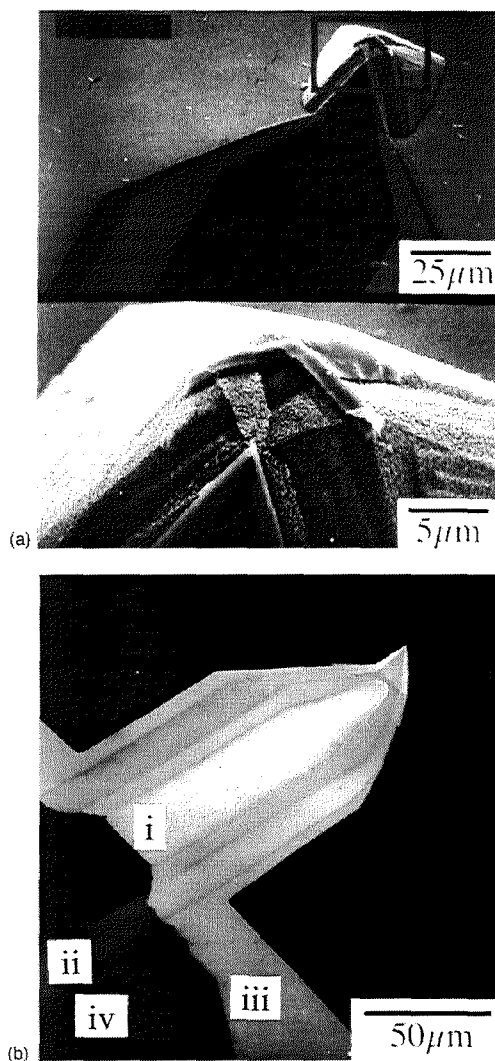


FIG. 2. (a) Unreleased thermocouple probe. (b) Released thermocouple probe (i) Mirror for force detection optics, (ii) thermocouple wire, (iii) 500 nm thick Si_3N_4 membrane, (iv) Si probe base.

sharp tip at the end of the cantilever. The sharpness of the tip is determined by the lithographic resolution of the Cr mask and the nature of the etch used. Tip radii to 30 nm have been produced although this is not felt to represent a limit, especially if the etch is allowed to undercut the mask. Two wires, one Au (25 nm thick), one Pd (50 nm thick), were then patterned in separate levels of EBL and transferred using liftoff. The wires overlap the edge of the cantilever, thus using the Si_3N_4 to define one of the edges of the wire. The thermocouple junction is therefore self-aligned to the end of the cantilever (Fig. 1). An unreleased device is shown in Fig. 2(i). Finally, a 250 μm thick Au layer is used to pattern bonding pads and a mirror for the force detection optics. The cantilever is then released by etching in KOH solution. [Fig. 2(ii)]. This dissolves away the remaining silicon membrane and completes the definition of the probe bases but does not

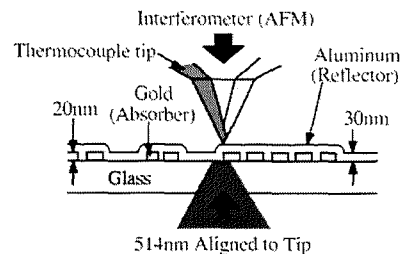


FIG. 3. Experimental setup.

attack the thermocouple which consists of noble metals and a NiCr adhesion layer or the cantilever.

The thermocouple size is dependent on the alignment accuracy of the EBL machine (Leica EBPG5HR 100 kV) between the thermocouple wire layers (specification 50 nm), however, this in turn depends on the quality of the etched markers on individual wafers. Presently 250 nm junctions have been produced with dimensional variability consistent with the above specification.

Images were acquired by fixing the tip to one side of a piezoelectric flexure stage, and raster scanning the specimen. Figure 3 shows a schematic of the experimental setup. The specimen consisted of large features for gross alignment and a number of high resolution test structures written by EBL on a glass substrate, and lifted off in 20 nm of Au. The small structures on the specimen were a series of gratings ranging from 200 nm down to 50 nm period (mark+space). The whole specimen was then evaporation coated with 30 nm of Al. To produce thermal features, the specimen was heated with a laser (Ar+, 514 nm, 10 mW). Au absorbs approximately five times more light than Al at 514 nm, and so a temperature gradient between the two metals was maintained. The laser pump beam was chopped at 1.025 kHz and a lock-in amplifier used to demodulate the resultant signal from the thermocouple. Noise levels were approximately 1 mK in unit bandwidth, limited by the preamplifier used and laser noise. Direct heating of the tip by transmitted light was not found to give a particularly large contribution to the measured signal: The total signal level was comparable to that obtained by direct illumination of the tip by the pump beam and the optical transmission of the specimen was measured to be approximately 10^{-3} .

Images were acquired with and without force feedback. For the former, a laser interferometer produced a signal proportional to the cantilever deflection, which was then regulated using a feedback loop to give constant force between tip and specimen. Simultaneous topographic and thermal information is gathered in this mode of operation. Figures 4(i) and 4(ii) show topographic and thermal images taken with force feedback. Figure 5 shows an image without force feedback, with a scan of the 200 nm grating inset. Scanning without force feedback was possible because of the flexibility of the Si_3N_4 cantilever. During use, no probe wear was observed in either mode of operation. The electrical properties of the thermocouple also appeared to be completely stable during normal use. Probe failure generally occurred due to gross mechanical stress or electrostatic discharge.

In the analysis of these results, it is important to note that

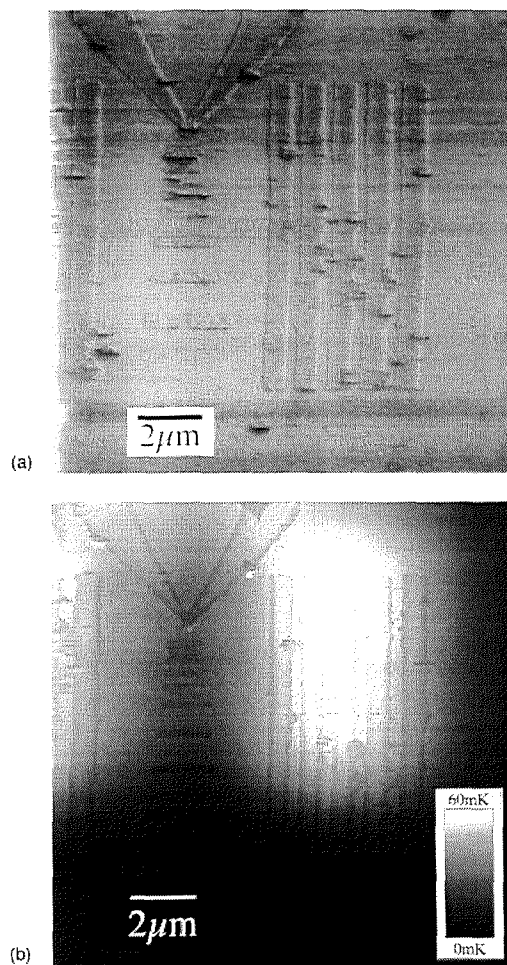


FIG. 4. (a) Topographic image, (b) Corresponding thermal image.

all the contrast in the thermal images is due to temperature changes at the thermocouple. The observed contrast is attributed to two mechanisms (1) surface temperature, and (2) thermal conduction between tip and specimen. Contrast due to surface temperature is the larger of the two and responsible for most of the contrast, however, spatial resolution appears to be limited by the pump laser spot size (approximately $2\ \mu\text{m}$). Note for low resolution features the gold regions are hotter than the aluminum regions, as expected. Thermal conduction is the mechanism by which the small

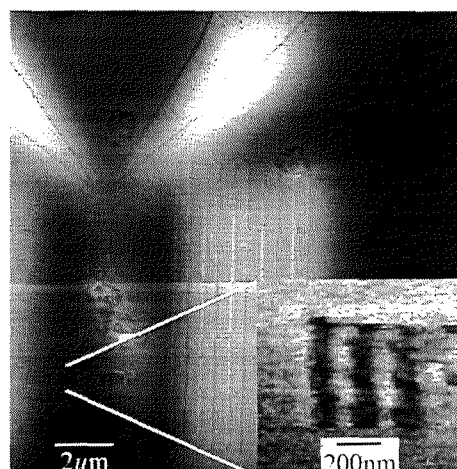


FIG. 5. Thermal image with 200 nm grating image inset.

features are resolved. Sharp topographic changes in the specimen can cause a reduction or increase in the area of thermocouple in contact with the specimen depending on the tip shape and edge shape. The rise time of the edges of the 200 nm grating were measured to be 40 nm. The period of the smallest resolvable grating was 80 nm which corresponds well to the edge resolution and proves a thermal spatial resolution of at least 40 nm for the instrument.

The authors would like to acknowledge the collaborative support of Motorola MRST.

- ¹G. Binnig, C. F. Quate, and C. Gerber, *Phys. Rev. Lett.* **56**, 930 (1986).
- ²C. C. Williams and H. K. Wickramasinghe, *Appl. Phys. Lett.* **49**, 1587 (1986).
- ³J. M. R. Weaver, L. M. Walpita, and H. K. Wickramasinghe, *Appl. Phys. Lett.* **49**, 1587 (1989).
- ⁴M. Stopka, L. Hadjiiski, E. Oesterschulze, and R. Kassing, *J. Vac. Sci. Technol. B* **13**, 2153 (1995).
- ⁵A. Hammiche, H. M. Pollock, M. Song, and D. J. Hourston, *Meas. Sci. Technol.* **7**, 142 (1996).
- ⁶A. Majumdar, J. P. Carrejo, and J. Lai, *Appl. Phys. Lett.* **62**, 2501 (1993).
- ⁷J. Lai, M. Chandrachod, A. Majumdar, and J. P. Carrejo, *IEEE Electron Device Lett.* **16**, 312 (1995).
- ⁸O. Nakabeppu, M. Chandrachod, Y. Wu, J. Lai, and A. Majumdar, *Appl. Phys. Lett.* **66**, 694 (1995).
- ⁹Y. G. Kim, K. S. Gam, and C. Rhee, *Metrologia* **33**, 337 (1996).
- ¹⁰D. R. S. Cumming, S. Thoms, J. M. R. Weaver, and S. P. Beaumont, *Microelectron. Eng.* **30**, 423 (1996).
- ¹¹H. Zhou, A. Midha, G. Mills, S. Thoms, S. K. Murad, and J. M. R. Weaver, *J. Vac. Sci. Techn. B* (Feb 1998).
- ¹²A. Midha, L. Donaldson, G. Mills, J. M. R. Weaver, and H. Zhou (unpublished).

(B)



ELSEVIER

Ultramicroscopy 80 (1999) 7-11

ultramicroscopy

www.elsevier.nl/locate/ultramic

Ultramicroscopy Letter

Detection of subsurface voids using scanning thermal microscopy

G. Mills^a, J.M.R. Weaver^{a,*}, G. Harris^b, W. Chen^b, J. Carrejo^b,
L. Johnson^b, B. Rogers^b

^aDepartment of Electronics & Electrical Engineering, University of Glasgow, Rankine Building, Oakfield Avenue, Glasgow G12 8LT, UK

^bMotorola SPS, 2200 West Broadway Road, Mesa, Arizona 85202, USA

Received 14 September 1998; received in revised form 22 March 1999

Abstract

A commercially available thermal scanned probe microscope has been used to look at voids which are buried under a SiO₂ passivation layer. The microscope detects heat flow from the probe into the specimen. Results show that it is possible to detect thermal conductivity changes caused by subsurface voids at a depth of over 200 nm. © 1999 Elsevier Science B.V. All rights reserved.

1. Introduction

In recent years a number of scanned probe microscopes have been developed in which a sensor is located at the tip of an AFM probe. Force feedback allows the sensor to be accurately positioned relative to a specimen surface. One of these innovations has been the scanning thermal microscope (SThM) [1]. Commercial SThMs use a miniature thermal resistor [2] positioned at the end of a sharp tip, which is in turn situated at the end of a cantilever. If a small current is passed through the resistor, and the resistance is measured as the tip is scanned over the surface, a local temperature map of the specimen is produced. If, on the other hand, a large current is passed and the resistor

temperature rises significantly above that of the specimen, the probe detects local changes in the local thermal conductivity of the sample [3]. In the latter mode of operation the thermal conductivity of the specimen, as presented at the surface, is an aggregate of any thermal conductivity variations down into the specimen. Changes in composition below the specimen surface will therefore produce a feature in the thermal map [4].

In the past SThM has been used to investigate Joule heating [5], phase changes in polymer blends [6], material variations in semiconductor devices [7], subsurface metal particles [4] and photothermal heating [8]. The ability to image subsurface features is desirable in many fields of microscopy, but is particularly important in the semiconductor industry where multi-level structures are commonplace. Passivating layers of silicon oxide and silicon nitride usually cover active regions, and serve to protect fine structures from mechanical and chemical damage.

* Corresponding author.

E-mail address: j.weaver@elec.gla.ac.uk (J.M.R. Weaver)

2. Experiments

In this letter we present results obtained using a commercial scanning thermal microscope (Dimension 3000 by Digital Instruments). The instrument uses modified silicon nitride probes which incorporate thermal resistors at the apex of a pyramidal tip. The resistor is an FIB-deposited Pt strap that bridges two Al contact pads directly at the tip. The resistive strap is approximately 1 μm wide, 6 μm long, and 0.25 μm thick and has a resistance of 1-2 k Ω . Fig. 1 shows an electron micrograph of the probe tip. Note that the significant resistor thickness produces a flat round top at the tip approximately 750 nm in diameter. It was observed that the resistor acts as a negative temperature coefficient thermistor. Scanning Auger analysis of the resistor material was performed using a Physical Electronics 670 field emission system. A 10 kV, 20 nA primary beam was used for the analysis after 1 kV Argon ions had been used to remove surface carbon (Fig. 2). Measurements revealed the resistor composition to be 60% C, 35% Pt and 5% O. Thermal scanning using this probe was performed in air at room temperature using a DC current in the region of 400 μA to resistively heat the probe.

A standard electromigration specimen (Fig. 3) consisting of three 1 μm wide metal wires passivated top and bottom with silicon oxide ($\approx 2 \mu\text{m}$

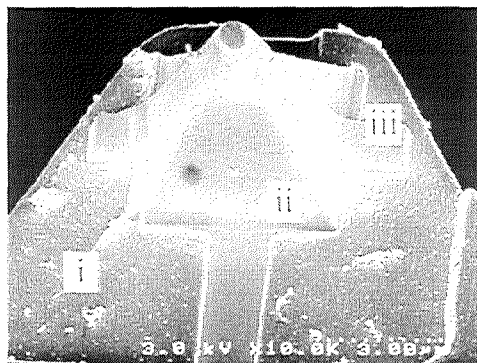


Fig. 1. SEM micrograph of a digital instruments thermal probe. (i) aluminum contacts, (ii) silicon nitride pyramid, (iii) resistive strap.

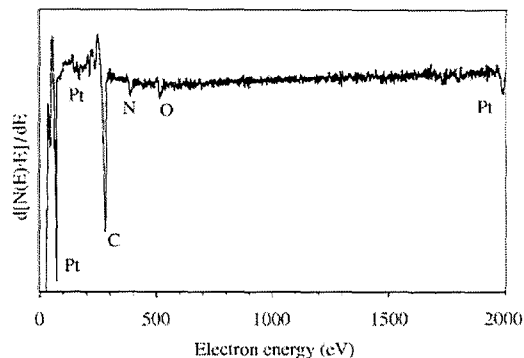


Fig. 2. Scanning Auger spectrum of the resistive strap on the digital instruments thermal probe.

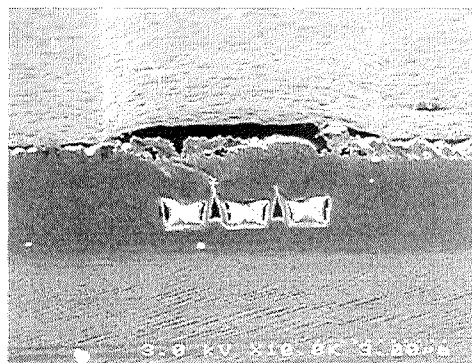


Fig. 3. SEM micrograph of a thermal specimen in cross section. Three aluminum wires passivated with 2 μm of silicon oxide.

thick) was selected for analysis. Tapping mode AFM and scanning electron microscopy of the passivated surface showed a flat topped plateau structure over the buried wires. No topographic evidence of the individual wires underneath was apparent. Growth of the oxide passivation layer was observed to have created voids between the wires due to overgrowth and pinch off. The planar nature of the passivation above the wires is useful since thermal features are often obscured by thermally detected topographic features [8,9]. The voids between the wires were expected to locally reduce the thermal conductivity from probe to specimen.

3. Results

An initial scan of the surface with the thermal probe showed no sign of the subsurface voids which are $0.25\ \mu\text{m}$ wide and $1.8\ \mu\text{m}$ deep. Previous studies had shown that Cu particles under a polymer layer had been detected at a depth of $1\ \mu\text{m}$ with lateral resolution of $1.5\ \mu\text{m}$ [4], and so efforts to thin the passivating layer were made. An FIB (Micrion 9000) was used to mill vertical trenches into the specimen above the wires. The trenches were $20 \times 20\ \mu\text{m}$ wide and varied in depth from $0.5\ \mu\text{m}$ to $2\ \mu\text{m}$. Spurious particles and defects in the specimen surface caused some areas within the trenches to mill at different rates. This resulted in the bottom of the trenches being very rough, and made for poor subsequent STHM measurements. One facet however, which had remained relatively flat, yielded an interesting image when scanned with the tip. Fig. 4a shows the topographic map of the bottom of the trench with Fig. 4b showing the simultaneous thermal map. The depth of this trench was approximately $1.7\ \mu\text{m}$. The trench appears relatively flat apart from a large pit at the bottom right of the image. The thermal image however shows a pair of fine lines (arrowed) running parallel to the subsurface wires which were not evident in the topographic image. The position of the pair of lines corresponds to that of the voids between the wires, and the contrast is created by the difference in thermal conductivity between the metal and the voids. Higher signal corresponds to less heat loss from the tip. The image suggests lateral thermal resolution of the order $100\ \text{nm}$ based on the observed thermal features. It is proposed that this is possible from a tip with diameter of $750\ \text{nm}$ because tip access is not restricted with this specimen, and (depending on tip angle and orientation) the tip asperity is in fact smaller than the tip diameter.

In order to explore the nature of this effect, especially the maximum depth at which the voids were detectable, a second specimen was prepared. The FIB was utilised once again, but this time to drill an angled trench down into the passivation over the wires. This particular geometry provides a gradation (wedge) of passivation thicknesses, and an angled section through the Al wires and substrate. Fig. 5 shows an SEM micrograph of the speci-

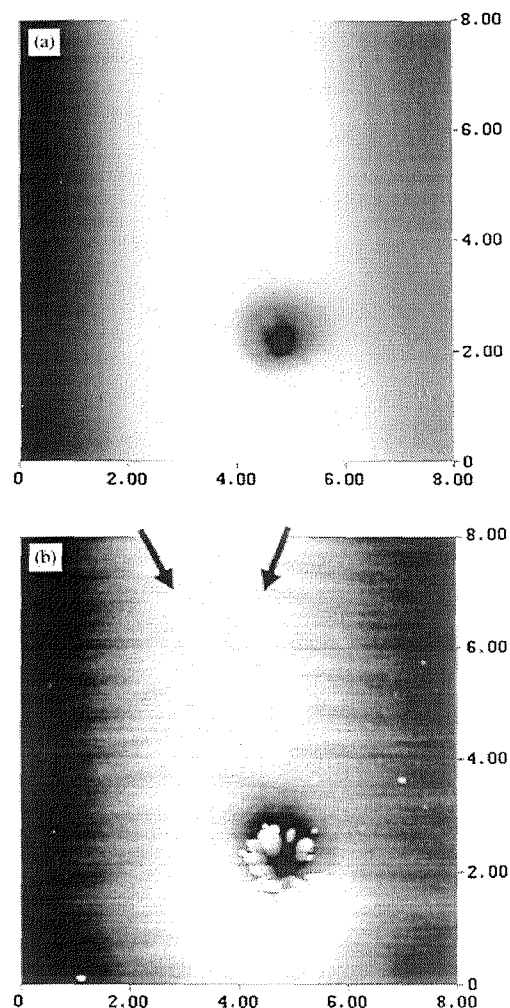


Fig. 4. (a) Topographic image of the bottom of an FIB-milled trench over the three passivated wires. Scan size is $8 \times 8\ \mu\text{m}$ and full scale contrast is $500\ \text{nm}$; (b) subsurface voids between the wires are visible. Scan size is $8 \times 8\ \mu\text{m}$ and full scale contrast is $0.3\ \text{V}$.

men. It can be seen that the scan surface is actually the side wall of the FIB cut. The sidewall is smoother than the base of the vertical cut, in that the only significant topographic variation is a corrugation ($1\ \text{nm p-p}$) due to the raster scan of the FIB spot and two trenches (arrowed) formed after

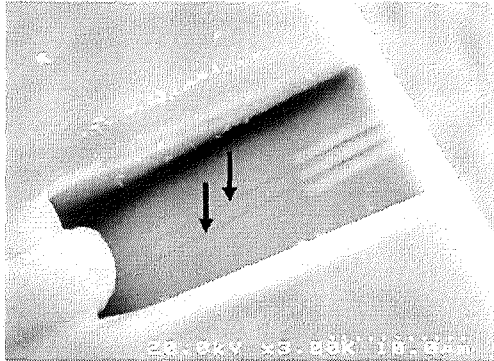


Fig. 5. SEM micrograph of the three passivated wires specimen cut at an angle using FIB. The three stripes to the right of the specimen are the aluminum wires. Passivation thickness over the wires varies from $2\ \mu\text{m}$ to $0\ \mu\text{m}$.

the voids are breached. The corrugation is small enough not to obscure the thermal data, and the trenches occur away from the passivation.

Topographic and thermal images of the angle cut specimen are shown in Fig. 6a and Fig. 6b, respectively. The area with decreasing passivation thickness is at the bottom of each image, with the bare metal lines in the middle and the substrate at the top. The thermal image clearly shows where the three metal wires appear, then disappear, at the specimen surface (three dark stripes). The voids are located directly below these three stripes in the thermal image, where the wires are still passivated. Two low thermal conducting features (light streaks) can be seen at this point. The dark regions on each side of the image are due to the sides of the wedge cut which are just out of frame. The tip loses more heat radiatively at these regions due to the proximity of these walls to the side of the tip [1]. The lighter regions to the top of the image is due to excessive roughening of the angle cut facet after the metal wires have been breached. The probe is making worse contact to the specimen in these regions and so loses less heat to the specimen. The voltage across the probe was measured at various points in the thermal image to determine the magnitude of the contrast. If the voltage across the probe in air is offset to be zero, the corresponding values while contacted to the passivated voids, metal wires and

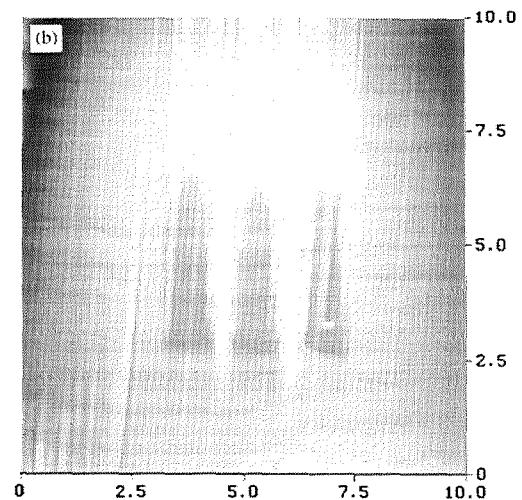
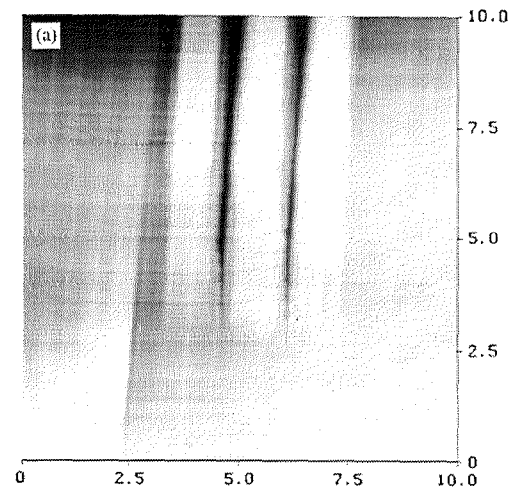


Fig. 6. (a) Topographic image of the angle cut specimen. Scan size is $10 \times 10\ \mu\text{m}$ and full scale contrast is $100\ \text{nm}$; (b) The passivated wires are to the bottom of the image. The three dark stripes are the metal wires themselves. The light streaks below the metal wires represent subsurface detection of the voids between the wires. Scan size is $10 \times 10\ \mu\text{m}$ and full scale contrast is $1\ \text{V}$.

SiO_2 were measured to be 25, 100 and 135 mV, respectively. Roughly twice the contrast is thus produced by the subsurface feature compared to that produced by the thermal conductivity differ-

ence between Al and SiO₂. This agrees with the observation that the voids can be seen in Fig. 4b at a depth of 100 nm without the evidence of the metal lines. From the known angle of the cut (15°) and the measured lateral extent of the low-thermal conducting features (light streaks), the maximum depth for resolution of the voids was calculated to be 225 nm (± 25 nm), limited by the residual topographic corrugation of the surface. The signal-to-noise ratio of the probe was measured from the image to be 18.5 dB. This figure includes the electrical noise of the probe, quantisation noise and topographic noise due to specimen roughness.

4. Conclusion

In conclusion, we have shown that sub-surface thermal imaging of VLSI devices using SThM is a practical technique. Contrast caused by structural defects created during passivation growth has been

observed, and is apparent at depths greater than 200 nm.

References

- [1] C.C. Williams, H.K. Wickramasinghe, *Appl. Phys. Lett.* 49 (1986) 1587.
- [2] R.B. Dinwiddie, R.J. Pyllki, P.E. West, *Therm. Conductivity* 22 (1994).
- [3] M. Nonnenmacher, H.K. Wickramasinghe, *Appl. Phys. Lett.* 61 (1992) 168.
- [4] A. Hammiche, H.M. Pollock, M. Song, D.J. Hourston, *Meas. Sci. Technol.* 7 (1996) 142.
- [5] K. Luo, Z. Shi, J. Lai, A. Majumdar, *Appl. Phys. Lett.* 68 (1996) 325.
- [6] A. Hammiche, M. Song, H.M. Pollock, M. Reading, D.J. Hourston, *Abstracts of Papers of the American Chemical Society*, 212, 278-POLY, 1996.
- [7] J. Lai, M. Chandrachood, A. Majumdar, J.P. Carrejo, *IEEE Electron Dev. Lett.* 16 (1995) 312.
- [8] G. Mills, H. Zhou, L. Donaldson, J.M.R. Weaver, *Appl. Phys. Lett.* 72 (1998) 2900.
- [9] K. Luo, Z. Shi, J. Varesi, A. Majumdar, *J. Vac. Sci. Technol. B* 15 (1997) 349.